

# HIGH PRECISION ABSOLUTE GRAVITY GRADIOMETRY WITH ATOM INTERFEROMETRY

A DISSERTATION  
SUBMITTED TO THE DEPARTMENT OF PHYSICS  
AND THE COMMITTEE ON GRADUATE STUDIES  
OF STANFORD UNIVERSITY  
IN PARTIAL FULFILLMENT OF THE REQUIREMENTS  
FOR THE DEGREE OF  
DOCTOR OF PHILOSOPHY

By  
Jeffrey Michael McGuirk  
September 2001

© Copyright 2001 by Jeffrey Michael McGuirk  
All Rights Reserved

I certify that I have read this dissertation and that in my opinion it is fully adequate, in scope and quality, as a dissertation for the degree of Doctor of Philosophy.

---

Mark Kasevich  
(Principal Adviser)

I certify that I have read this dissertation and that in my opinion it is fully adequate, in scope and quality, as a dissertation for the degree of Doctor of Philosophy.

---

Steven Chu  
(Department of Physics and Applied Physics)

I certify that I have read this dissertation and that in my opinion it is fully adequate, in scope and quality, as a dissertation for the degree of Doctor of Philosophy.

---

John Turneure  
(Department of Physics)

Approved for the University Committee on Graduate Studies:



# Abstract

An absolute gravity gradiometer was demonstrated using atom interference techniques. This is the first realization of an gradiometer which uses an absolute standard for its calibration. A gravity gradiometer measures spatial changes in the gravitational field over a fixed baseline by making simultaneous acceleration measurements with two spatially separate accelerometers. The gradiometer has a differential sensitivity of  $4 \times 10^{-9} \text{ g}$  in 1 s and a differential accuracy of  $10^{-9} \text{ g}$ . This is the best gradiometer accuracy reported to date and the sensitivity competes favorably with existing state-of-the-art instruments. A proof-of-principle measurement of the gravity gradient of a small test mass was made leading towards a precision measurement of the gravitational constant. The performance was characterized on a vibrationally noisy reference platform, testing the ability of the gradiometer to reject common-mode accelerations. Techniques for extracting gradient information were explored. Applications of sensitive and accurate gravity gradiometers include tests of general relativity, studies of the gravitational constant, navigation, and geophysical studies.

The principle behind the measurement is as follows: proof masses for the two accelerometers consist of two ensembles of laser-cooled cesium atoms whose acceleration is measured by an interferometer sequence. The interferometer is comprised of light pulses in a  $\pi/2 - \pi - \pi/2$  pulse sequence which acts to divide, deflect, and recombine each atomic wavepacket. The final state of the atom depends on the inertial forces experienced by the atom during its trajectory through the interferometer. The two simultaneous acceleration measurements are subtracted to produce a gravity gradient. This technique is advantageous because it offers intrinsic absolute calibration, robust operation, and uniformity of proof masses.

# Acknowledgements

I am deeply grateful to my advisor Mark Kasevich. In addition to being a gifted physicist who taught me an amazing amount of physics, Mark has both the vision to pursue interesting ideas and the experimental ability to carry them out. On top of physics, it has just been fun to work with Mark. I cannot forget the opportunity he allowed me to live on both coasts. Along the way, I have been fortunate to work with a number of talented people. Dean Haritos and Philippe Bouyer helped build the experiment at Stanford. During his post-doc, Mike Snadden assisted with the proof-of-principle work at Stanford, helped during the move to Yale in 1997, and was instrumental in the steps leading to the current device performance. Also, in his spare time, Mike wrote 25,000 lines of computer code to control the timing and data acquisition. Greg Foster and Jeff Fixler helped develop the data extraction routines and demonstrate the performance of the gradiometer, and they have smoothly assumed the running of the experiment for the measurement of  $G$ . Post-doc Kai Bongs and students Romain Launay and Neelima Sehgal developed the details of the interferometer theory and enlightened me with many discussions. I am also thankful for the general laboratory expertise of my colleagues Brian Anderson and Todd Gustavson, and for many useful discussions with Kurt Gibble. The work in this dissertation was funded by ONR, NASA, and NRO. My time in Stanford and New Haven was made more enjoyable and my sanity was maintained with the help of Dean, Mike, Todd, Brian, Jamie Kerman, and the Saeco Magic de Luxe. Finally I wish to thank my family for their support.

# Contents

<b>Abstract</b>	<b>v</b>
<b>Acknowledgements</b>	<b>vi</b>
<b>1 Introduction</b>	<b>1</b>
1.1 Introduction . . . . .	1
1.2 Gradiometry and the equivalence principle . . . . .	2
1.3 Laser manipulation of atoms . . . . .	3
1.4 Atom interferometry . . . . .	4
1.5 Overview . . . . .	5
<b>2 Gravity Gradiometry</b>	<b>6</b>
2.1 Gradient tensor . . . . .	6
2.2 Gradient units . . . . .	7
2.3 Gradiometer applications . . . . .	8
2.3.1 Inertial navigation . . . . .	8
2.3.2 Subsurface mass anomalies . . . . .	9
2.3.3 Gravitational constant . . . . .	11
2.3.4 Tests of General Relativity . . . . .	14
2.3.5 Fifth force experiments . . . . .	14
2.4 Alternate gradiometer technologies . . . . .	15
2.4.1 Mass-spring gradiometers . . . . .	15
2.4.2 Superconducting instruments . . . . .	16
2.4.3 Falling cornercube gradiometer . . . . .	16

2.4.4	Absolute gradiometry . . . . .	17
<b>3</b>	<b>Laser Cooling and Trapping</b>	<b>18</b>
3.1	Atomic structure . . . . .	18
3.2	Two-level atoms . . . . .	19
3.3	Optical forces . . . . .	21
3.3.1	Scattering force . . . . .	21
3.3.2	Dipole force . . . . .	23
3.4	Magnetic forces . . . . .	23
3.5	Laser cooling . . . . .	24
3.5.1	Doppler cooling . . . . .	24
3.5.2	Polarization gradient cooling . . . . .	26
3.6	Magneto-optical trapping . . . . .	27
3.6.1	Trap loading . . . . .	29
3.6.2	Atomic fountains . . . . .	30
3.7	Two-photon stimulated Raman transitions . . . . .	31
3.8	Atom detection . . . . .	36
3.9	Experiment synopsis . . . . .	37
<b>4</b>	<b>Atom Interferometry</b>	<b>39</b>
4.1	Intuitive analogy . . . . .	40
4.2	Interferometer description . . . . .	41
4.3	Wavepacket overlap phase . . . . .	43
4.4	Laser phase . . . . .	44
4.4.1	Frequency term . . . . .	45
4.4.2	Initial phase . . . . .	46
4.5	Free propagation phase . . . . .	47
4.5.1	Path integral formalism . . . . .	47
4.5.2	Perturbative approach . . . . .	49
4.6	Nonuniform acceleration fields . . . . .	50
4.6.1	Exact solution . . . . .	50
4.6.2	Gravity gradients . . . . .	51



4.6.3	Rotations . . . . .	52
4.7	Limitations to the theory . . . . .	53
4.8	Application to gradiometry . . . . .	55
<b>5</b>	<b>Experimental Apparatus</b>	<b>57</b>
5.1	Apparatus overview . . . . .	57
5.2	Vacuum system . . . . .	57
5.2.1	Motivation for vacuum . . . . .	57
5.2.2	Vacuum chamber design and preparation . . . . .	59
5.2.3	Chamber evacuation . . . . .	62
5.3	Laser system . . . . .	63
5.3.1	Master laser . . . . .	63
5.3.2	Laser amplifiers . . . . .	65
5.3.3	Optical fiber system . . . . .	68
5.4	Laser cooled atomic sources . . . . .	69
5.5	State preparation . . . . .	71
5.5.1	Optical pumping . . . . .	72
5.5.2	Composite pulse techniques . . . . .	74
5.6	Atom interferometer . . . . .	76
5.6.1	Raman lasers . . . . .	76
5.6.2	Beam delivery . . . . .	79
5.6.3	Propagation reversal . . . . .	82
5.6.4	Raman beam parameters . . . . .	83
5.6.5	Interferometer operation . . . . .	85
5.7	Detection system . . . . .	85
5.7.1	Background . . . . .	85
5.7.2	Detection apparatus . . . . .	87
5.7.3	Detection system performance . . . . .	91
5.7.4	Noise analysis . . . . .	93
5.8	Vibration isolation subsystem . . . . .	94
5.8.1	Mechanical design . . . . .	95

5.8.2	DSP servo system . . . . .	96
5.9	Microwave generation . . . . .	96
<b>6</b>	<b>Results</b>	<b>99</b>
6.1	Proof-of-principle results . . . . .	99
6.2	Signal extraction . . . . .	101
6.2.1	Normalization . . . . .	101
6.2.2	Interference fringe fitting . . . . .	102
6.2.3	Magnetic phase shifting . . . . .	104
6.2.4	Gaussian elimination reduction . . . . .	106
6.2.5	Circle fitting . . . . .	108
6.2.6	Ellipse fitting . . . . .	111
6.2.7	Summary of data extraction methods . . . . .	115
6.3	Sensitivity characterization . . . . .	116
6.3.1	Noise . . . . .	117
6.3.2	Proof-of-principle mass detection . . . . .	118
6.4	Accuracy estimation . . . . .	118
6.4.1	Tidal measurement . . . . .	118
6.4.2	Allan variance . . . . .	120
6.4.3	Gravitational constant measurement . . . . .	122
6.5	Immunity to environmental noise . . . . .	124
6.5.1	Linear acceleration . . . . .	124
6.5.2	Rotation . . . . .	127
<b>7</b>	<b>Discussion</b>	<b>130</b>
7.1	Performance Limits . . . . .	130
7.1.1	SNR limits . . . . .	130
7.1.2	Rotations . . . . .	131
7.2	Related methods . . . . .	133
7.2.1	Large area interferometers . . . . .	133
7.2.2	Interferometer comparisons . . . . .	139
7.2.3	Multi-loop interferometers . . . . .	142

7.2.4	Curvature measurements . . . . .	145
7.2.5	Multi-axis gradiometers . . . . .	146
<b>8</b>	<b>Conclusion</b>	<b>149</b>
8.1	Future enhancements . . . . .	149
8.2	Future measurements . . . . .	151
<b>A</b>	<b>Physical parameters of Cs</b>	<b>154</b>
<b>B</b>	<b>Digital control loops</b>	<b>156</b>
	<b>Bibliography</b>	<b>159</b>

# List of Tables

A.1	Properties of Cs . . . . .	154
B.1	Vibration isolation system filter bandwidths and gains. . . . .	158

# List of Figures

1.1	Conceptual representation of a gradiometer . . . . .	1
2.1	Gravity gradient of an underground structure . . . . .	10
2.2	Recent measurements of the gravitational constant . . . . .	13
3.1	Schematic representation of the scattering force . . . . .	22
3.2	Illustration of Doppler cooling . . . . .	25
3.3	Illustration of an atom in a 1D MOT . . . . .	28
3.4	Schematic depictions of 3D MOT configurations . . . . .	32
3.5	Energy level diagram for Raman transitions . . . . .	34
4.1	Conceptual picture of a gravity measurement . . . . .	40
4.2	Recoil diagram of the interferometer sequence . . . . .	42
4.3	Interferometer path overlap in the presence of gradients . . . . .	44
5.1	Picture of the gravity gradiometer apparatus . . . . .	58
5.2	Vacuum chambers . . . . .	60
5.3	Spectral purity of tapered amplifiers . . . . .	66
5.4	Block diagram of trapping laser system . . . . .	68
5.5	Launching of cold atoms . . . . .	71
5.6	Sequence of state preparation and interferometer pulses . . . . .	73
5.7	Transfer efficiency of composite pulses . . . . .	75
5.8	Raman beam geometry . . . . .	78
5.9	Block diagram of the Raman laser system . . . . .	79
5.10	Rejection of magnetic phase shifts with Raman propagation reversal .	83

5.11	Interferometer contrast simulation . . . . .	84
5.12	Schematic representation of the detection apparatus . . . . .	88
5.13	Study of optimal detection parameters . . . . .	89
5.14	Shot noise limited detection . . . . .	92
5.15	Schematic view of the vibration isolation system . . . . .	95
5.16	Performance of the vibration isolation system . . . . .	97
6.1	Proof-of-principle Earth gradient measurement . . . . .	100
6.2	Sinusoidal least squares fits to interference fringes . . . . .	103
6.3	Decrease of SNR with phase mismatch . . . . .	105
6.4	Data reduction using Gaussian elimination method . . . . .	108
6.5	Data analysis using deviations from a circle . . . . .	110
6.6	Ellipse fitting of data . . . . .	113
6.7	Calibration of ellipse fitting routine . . . . .	114
6.8	Comparison of interference fringes with vibration isolation . . . . .	117
6.9	Measurement of the gradient of a small test mass . . . . .	119
6.10	Gravitational tidal signals . . . . .	120
6.11	Allan variance of gradiometer data . . . . .	121
6.12	Precision lead test masses . . . . .	122
6.13	Linear acceleration test . . . . .	125
6.14	Interferometer transfer function for vibrational phase noise . . . . .	126
6.15	Platform tilt test . . . . .	128
6.16	Effect of rotations on interferometer contrast . . . . .	129
7.1	$6\hbar k$ interferometer recoil diagram . . . . .	133
7.2	Schematic representation of multiple pulse interferometers . . . . .	134
7.3	Comparison of phase shift for $2\hbar k$ and $6\hbar k$ interferometers . . . . .	137
7.4	Interference fringes using a $6\hbar k$ interferometer . . . . .	138
7.5	Recoil diagrams for multiple loop interferometers . . . . .	144
7.6	Triple-loop interference fringes . . . . .	146
7.7	Full gradient tensor measurement configuration . . . . .	147

A.1	Energy level diagram for $^{133}\text{Cs}$ . . . . .	155
B.1	Transfer function of the SHP-voice coil system . . . . .	157
B.2	Comparison of digital filters . . . . .	158

# Chapter 1

## Introduction

### 1.1 Introduction

Gravity gradiometry is the study of spatial changes in the gravitational field over a known distance. A gravity gradiometer measures the spatial rate of change of the gravity field, *i.e.* its first moment or first derivative. In its most conceptually simple form, a gravity gradiometer measures the gravitational acceleration of two objects, subtracts them, and divides by the distance between them to obtain a gradient. This is depicted in Fig. 1.1. Precise and accurate measurements of gravity gradients have importance in a wide array of applications, from technological applications such as navigation, oil and mineral exploration, and geodesy, to scientifically interesting

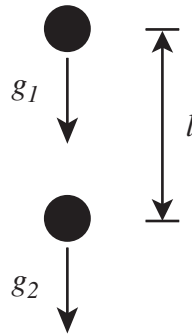


Figure 1.1: A conceptual representation of a gradiometer using two freely falling bodies. The gravity gradient is given by  $(g_1 - g_2)/l$ .



applications including a precision measurement of the gravitational constant, tests of general relativity, and searches for new physics in the form of a fifth force. The gravity gradiometer described in this dissertation has the potential to meet many of these applications, based on its demonstrated differential sensitivity of  $4 \times 10^{-9}g$  in 1 s and differential accuracy of less than  $10^{-9}g$ .

## 1.2 Gradiometry and the equivalence principle

At first glance, it might seem that a gravity gradient is an odd quantity to measure. After all, the quantity of interest in most of the applications listed is gravity itself. The reason why gravity gradients are important lies in the equivalence principle. Einstein, in his 1911 formulation of equivalence [1], states that

*“This assumption of exact physical equivalence makes it impossible for us to speak of the absolute acceleration of the system of reference, just as the usually theory of relativity forbids us to talk of the absolute velocity of a system; and it makes the equal falling of all bodies in a gravitational field seem a matter of course.”*

In other words, when making a gravity measurement, it is impossible to differentiate the gravitational acceleration experienced by the proof mass from the acceleration of the reference frame of the measurement. The reference frame of the measurement is defined by the platform on which the acceleration read-out devices<sup>1</sup> are placed. If this reference frame is accelerating, due to vibrations or motion of the vehicle transporting the device, then the measured acceleration will include these offsets and noise from the accelerating reference platform. For this reason, gravimetry is fundamentally challenged by its sensitivity to platform vibrations. A sensitive gravimeter requires a quiet reference platform, otherwise the noise from platform vibrations limits the sensitivity.

It was realized that a gravity gradiometer can circumvent the problem of platform vibrations. By making simultaneous acceleration measurements at two spatially

---

<sup>1</sup>The acceleration sensitive components can be capacitors, superconducting coils, photodetectors, mirrors, *etc.* depending on the measurement method.

separated locations a differential measurement of the gravity field can be made. If both these measurements are made with respect to the same reference frame, and if the two accelerometers experience common vibrations, then all accelerations of the reference platform can be removed as a common-mode. Measuring gravity gradients then can be an effective tool to circumvent the noise limits of a vibrationally noisy platform<sup>2</sup>. The key to successful gravity gradiometry lies in ensuring that the two accelerometers are tightly coupled so as to only have common-mode vibrations. Traditionally, there has been a compromise between intrinsic gradiometer sensitivity and noise suppression in gravity gradiometers. This tradeoff is because expanding the baseline distance between the two accelerometers linearly increases the sensitivity to gradients, but all previously demonstrated devices require rigid mechanical coupling between accelerometers for good common-mode vibration suppression, which becomes difficult to do over large baselines. The device presented in this dissertation is fundamentally different. It uses light pulses effectively to couple the two accelerometers together and requires no rigid coupling between accelerometers to maintain common-mode performance<sup>3</sup>. By removing this constraint, the baseline can be made arbitrarily large, and the sensitivity scales accordingly.

### 1.3 Laser manipulation of atoms

The key enabling technologies for this gravity gradiometer are the techniques of manipulating atoms using lasers that were pioneered over the last 20 years. In the mid to late 1970s, several proposals for slowing atoms with optical forces were made [2, 3], but it was not until 1982 that it was first observed that the motion of atoms could be damped by transferring momentum to them from optical fields [4]. In 1986, this advance was taken one step further with the invention of “optical molasses” [5]. An optical molasses is a configuration of laser beams that acts to damp the motion of atoms in all directions by transferring kinetic energy to the optical field. Based

---

<sup>2</sup>The definition of “noisy” depends on the scale of the measurement, and for some purposes, platforms with accelerations as small as  $10^{-9}g$  are considered noisy.

<sup>3</sup>The light pulses couple vibrations to the two accelerometers identically, and these common-mode spurious accelerations are removed during the data reduction.

on this technique, atoms could be cooled to temperature of several  $\mu\text{K}$ , where their velocities are slow enough to perform experiments requiring long interrogation times. Furthermore a way of producing a dense cloud with large numbers of laser-cooled atoms was pioneered by adding a magnetic field to the molasses to produce a localizing restoring force [6]. Such a configuration is called a magneto-optical trap (MOT), and can be used to produce as many as  $10^{10}$  ultra cold atoms in a region with a size of  $\sim 1$  mm or less. The MOT has become the workhorse of modern atomic physics, as it has proven to be an extremely robust source of dense, cold atoms that is straightforward to produce. In recognition of these achievements, the Nobel Prize in Physics was awarded in 1997 to three of the pioneers of laser cooling and trapping: Chu, Cohen-Tannoudji, and Phillips [7].

## 1.4 Atom interferometry

Ramsey developed an interferometer for atoms based on microwave fields (the “separated oscillatory field” method) in the 1950s [8]. Building on early work in neutron interferometry [9, 10], there were several proposals to use neutral atoms as inertial force sensors in atom interferometers [11, 12]. Analogous to neutron scattering from silicon crystals, atom interference was shown using narrow mechanical gratings to diffract the atom into two separate wavepackets and then to diffract them back to overlap and interfere [13]. More interestingly, soon thereafter, atom interference was demonstrated using not mechanical gratings to diffract the atoms, but *optical fields* in the form of two-photon stimulated Raman transitions [14, 15]. Optical fields were used to divide the atom into two wavepackets, direct the wavepackets back towards each other after a drift period, and finally to recombine the wavepackets at a location where their interference could be observed. These optical elements are analogous to the beamsplitters and the mirrors used in a standard Michelson interferometer. Soon after, a light-pulse-based interferometer sensitive to gravitational acceleration on the freely falling atoms was demonstrated in 1992 [16]. In the following years a similar-in-concept atom interferometer gyroscope was demonstrated [17], sensitive enhancements to the original gravimeter idea were made [18], and the gravity gradient

sensitive interferometer presented herein was demonstrated [19].

## 1.5 Overview

The format of this dissertation is as follows. Chapter 2 contains an introduction to the study of gravity gradients, including interesting applications of gradiometry as well as brief descriptions of existing gradiometers. A review of the fundamental concepts of the behavior of atoms in optical fields, particularly related to laser cooling and trapping and two-photon Raman transitions, is the subject of Chapter 3. Chapter 4 provides a detailed discussion on the nature of the atom interferometers and the effects of inertial forces on the atomic phases in interferometers. The experimental apparatus is described in Chapter 5. Chapter 6 presents the results of the experiments and includes a detailed discussion on the extraction of phase information from the data. Chapter 7 provides a discussion of the limits of the gravity gradiometer, proposes several related interferometer schemes, and compares this work with related methods. Finally, Chapter 8 concludes with possible future experimental enhancements as well as brief descriptions of potential future measurements.

# Chapter 2

## Gravity Gradiometry

The purpose of this section is to discuss several aspects of gravity gradiometry. Existing gravity gradiometers will be described. The need for sensitive and accurate gradiometer is elucidated. The applications described in section 2.3 are by no means an exhaustive listing of the technical and scientific applications of a precise absolute gravity gradiometer. They are merely meant as descriptions of several of the more important applications and some of the new physics that might come out of such studies of gravity requiring unprecedented levels of accuracy and precision.

### 2.1 Gradient tensor

The gravity gradient is a tensor quantity. The gradient tensor is a three-by-three matrix whose components are the derivative of the three components of the gravity vector ( $x$ ,  $y$ , and  $z$ ) with respect to each spatial direction:

$$T = \nabla \mathbf{g} = \begin{pmatrix} \frac{\partial g_x}{\partial x} & \frac{\partial g_x}{\partial y} & \frac{\partial g_x}{\partial z} \\ \frac{\partial g_y}{\partial x} & \frac{\partial g_y}{\partial y} & \frac{\partial g_y}{\partial z} \\ \frac{\partial g_z}{\partial x} & \frac{\partial g_z}{\partial y} & \frac{\partial g_z}{\partial z} \end{pmatrix}. \quad (2.1)$$

The notation  $g_{xx}$  is often used to denote  $\frac{\partial g_x}{\partial x}$ , and so forth. There are nine components to the gradient tensor, however only five of them are independent components. The

tensor is a symmetric tensor, *i.e.*  $T_{ij} = T_{ji}$ . Additionally, the trace is equal to zero so knowledge of two diagonal components determines the third. In order to characterize completely the gravitational field, five components of the tensor must be measured, two diagonal components and three off-diagonal components. In practice however, enough information is often carried primarily in one component, and then a one-axis device is usually sufficient. The device presented herein is a one-axis gradiometer, however in section 7.2.5 various schemes for constructing multi-axis devices are discussed.

## 2.2 Gradient units

The fundamental unit of gravity gradiometry is the Eötvös, named after the Hungarian physicist credited with making the first gravity gradient measurements [20],  $1 \text{ E} = 10^{-9} \text{ s}^{-2}$ , or  $1 \text{ E} \simeq 10^{-10} \text{ g/m}$ , where  $g$  is the gravitational acceleration near the Earth's surface and is  $\simeq 9.8 \text{ m/s}^2$ . The Eötvös is an exceedingly small unit, and measurements with accuracies of 1 E or less have not been achieved prior to this work. As a point of reference, the Earth's gravity gradient with increasing altitude near the surface is  $\sim 3000 \text{ E}^1$ . It is a somewhat nonintuitive unit, and often it is preferable to think of gravity gradiometers in terms of differential acceleration measurements, which are typically referred to as a differential acceleration divided by a baseline, *i.e.* as  $\text{g/m}$ . In these units, the Earth's gradient is  $\sim 3 \times 10^{-7} \text{ g/m}$ . To further complicate the picture, the CGS unit of acceleration is the gal,  $1 \text{ gal} = 1 \text{ cm/s}^2 \simeq 10^{-3} \text{ g}$ . Sensitive acceleration measurements are discussed in terms of  $\mu\text{gal}$ , and  $1 \text{ E} = 0.1 \mu\text{gal/m}$ . This unit is the unit of choice in the navigation and geophysics communities, but will not be used here.

The sensitivity of the gradiometer is typically quoted in units of  $\text{E}/\sqrt{\text{Hz}}$  or  $\text{g}/\sqrt{\text{Hz}}$ . These units are meant to be the sensitivities for a white noise limited process where the precision scales inversely as the square root of the measurement time [21]. For example, this means that a  $1 \text{ E}/\sqrt{\text{Hz}}$  device has a raw noise of 1 E in a 1 Hz bandwidth, giving a precision of about 1 E in 1 s, and a precision of about 0.1 E in 100 s if it has

---

<sup>1</sup>The Earth's gradient is obtained from the derivative of the inverse square law of gravity.

white noise properties. It is the case that the gradiometer presented herein has white noise scaling over a range of time greater than  $10^3$  s before the sensitivity begins to roll off. This is discussed in section 6.4.

## 2.3 Gradiometer applications

There is a host of applications for gravity gradiometry. Typically, knowledge of gravity is required for a number of field applications. These applications almost always include operation on a noisy platform, which severely hampers gravitational acceleration measurements. For this reason, gravity gradiometry is useful. Additionally for precision scientific measurements, gravity gradiometry lessens the constraints on the level of the exact knowledge of the local gravitational field and its variations from tides, ocean loading, post-glacial rebound, near-field masses, *etc.* [22]. This section describes some of the major applications for gravity gradiometry and related measurements that could be made with the atom interferometer presented in this dissertation. First technological applications are described, and then precision measurements of scientific interest are described.

### 2.3.1 Inertial navigation

A long-standing goal of the navigation community has been the development of a quiet, self-contained inertial navigation system. Inertial navigation consists of measuring the inertial forces experienced by an object, specifically rotations and accelerations, and using these forces to determine completely the trajectory and location of the object from a known initial position [23]. The Global Positioning System (GPS) is an excellent navigation tool, as are active methods such as radar and sonar, however there are a number of environments where GPS is unavailable and active methods are unavailable or undesirable. In these instances, inertial navigation is key. In navigation grade inertial navigation systems<sup>2</sup> the position estimate obtained from

---

<sup>2</sup>Navigation grade systems require higher performance than tactical grade systems due to longer timescales involved.

the on-board accelerometers and gyroscopes is typically limited by knowledge of local gravity  $\mathbf{g}$ , particularly near large gravitational anomalies such as mountains and valleys, as these anomalies can perturb the perceived platform vertical as determined by the gyroscopes. In these instances, an onboard gravity gradiometer could correct the inertial navigation system's position estimate. The positioning obtained from GPS is limited by the knowledge of the position of the satellites themselves. Exact knowledge of the Earth's gravitational field dynamically measured onboard each GPS satellite operating at a differential sensitivity  $\sim 10^{-9} \text{ g}/\sqrt{\text{Hz}}$  would allow for correction of orbital perturbations from the Earth's non-uniform gravity field, *i.e.* periodic orbital corrections from ground-based measurements of the satellite orbits would not be required.

### 2.3.2 Subsurface mass anomalies

Another application well-suited to gravity gradiometers is the detection of subsurface mass anomalies. Nonuniform densities below the surface of the Earth cause gravitational anomalies through changes in both the local gravity  $g$  and the gravity gradient  $\nabla g$ . Examples of nonuniformities include oil and mineral deposits, water reservoir levels, and underground tunnels and bunkers. Recently, a measurement of two large, hollowed out underground chambers was made by using the mechanical gradiometer described in section 2.4.1. As a gradiometer is moved across a subsurface anomaly, a characteristic signal is seen (see Fig. 2.1). The altitude at which the gradiometer makes measurements (*i.e.* land-based, airborne, or satellite) as well as the depth of the anomaly determine the spatial resolution at which the anomaly may be detected. The spatial resolution of the gravity gradient measurements can be understood by expressing the gravity field of the Earth as an expansion of spherical harmonics at the altitude of the measurement. For optimal detection of features, the wavelengths of the primary components in the spherical harmonic expansion of the features must be nearly matched to the baseline of the gravity gradiometer as well as to the distance from the gradiometer to the anomaly. This is particularly important for gradiometric scans taken from high flying airplanes and satellite. Finally, the speed at which



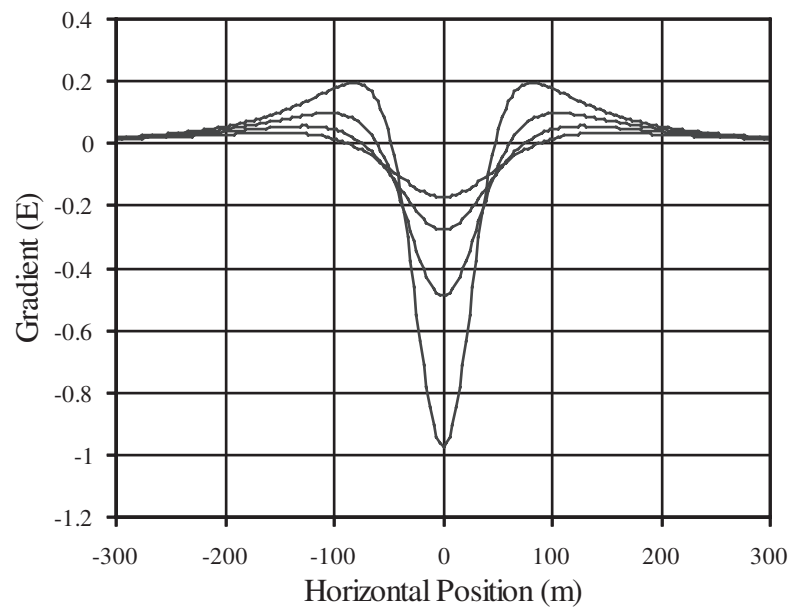


Figure 2.1: Simulation of a typical gradient of an underground structure such as a tunnel as a gravity gradiometer is scanned across the anomaly from the surface. The tunnel is assumed to be  $2\text{ m} \times 2\text{ m}$ , and the four lines are for depths of 110 m, 90 m, 70 m, and 50 m, from top to bottom.

a gradiometer is moved across an anomaly and the size of the gradient produced by the anomaly determine the sensitivity necessary to detect the subsurface mass distribution.

### 2.3.3 Gravitational constant

One of the least well known fundamental constants is the gravitational constant<sup>3</sup>  $G$  [25]. The primary reason for this is that gravity is the weakest known force, *e.g.* weaker than the electromagnetic interaction between two baryons by  $\sim 10^{40}$ . Additionally gravity is a force that cannot be screened, making a precise measurement difficult to decouple from the environment. All measurements of  $G$  essentially use the attraction from a well-characterized test mass on a well-characterized proof mass. The proof mass is the mass that is internal to the gradiometer and is the mass on which the acceleration measurement is performed. All such measurements require complete characterization of the test mass to the level of accuracy desired for the experiment. This reliance on the accuracy of the test mass distribution is a fundamental limit to all measurements of  $G$ , although some test mass geometries lessen the constraints on the exact knowledge of the test mass distribution.

A more accurate value for the gravitational constant is beneficial for a number of reasons. Several geophysical parameters are limited by the knowledge of  $G$ , including the mass of the Earth, its density, and its elastic modulus [26]. Ironically, the accuracy of Earth-based gravity gradiometers is limited by the precision that  $G$  is known due to higher order moments of the Earth's field [27]. The gravitational constant also enters into several fundamental ideas of physics. The gravitational constant directly is part of the definition of the Planck scales of length, time, and mass which define the dimensions at which space-time becomes discontinuous [28]. Theories which predict the unification of forces at a high energy scale are influenced by the value of  $G$  [29].

---

<sup>3</sup>In many sources,  $G$  is called Newton's Constant. It has been pointed out that Newton did not, in fact, postulate a gravitational constant, and some object to the name "Newton's Constant" [24]. Newton merely stated a proportionality (which inherently implied a constant of proportionality). Another view is that the constant was called Newton's Constant in honor of the pioneer in gravity research. In any case, this work will refer to  $G$  as the gravitational constant in order to avoid controversy.

Whether  $G$  is even a “constant” at all has ramifications in General Relativity [30]. Finally, there have been several attempts to derive  $G$  from first principles to attempt to prove if it is even a fundamental constant [31]. A review of the various historical and current studies involving  $G$  as well as the significance of  $G$  can be found in [32].

The Committee on Data for Science and Technology (CODATA) released a 1986 accepted value of  $G$  of  $6.67259(85) \times 10^{-11} \text{ m}^3/\text{kg}/\text{s}^2$ , *i.e.* a part in  $\sim 10^{-4}$  uncertainty, based on a number of leading  $G$  measurements at that time [33]. In the following 10 years, a number of higher accuracy measurements were made, but these measurements disagreed from each other at the  $10^{-3}$  level [32]. This resulted in a 1998 CODATA value of  $6.673(10) \times 10^{-11} \text{ m}^3/\text{kg}/\text{s}^2$  [25], which is an uncertainty ten times larger than in 1986. These fluctuating error bars are a manifestation of the difficulty inherent in the measurement. Since the last CODATA value, there have been several extremely precise measurements of  $G$ , and it is likely that the uncertainty will drop with the next CODATA value. A summary of many of the significant measurements since 1969 is presented in Fig. 2.2.

The most precise measurements to date were all made using torsion balances [34]. A torsion balance is a modified version of the Coulomb balance using neutral proof masses to detect spatially varying gravity fields. It is based on a torsion pendulum, *i.e.* a mass suspended on a thin wire. A differential acceleration on two sides of the proof mass will cause the mass to rotate on the wire. A torquing force is applied to keep the mass from rotating, and the differential acceleration is proportional to the applied torque. The torsion balance was the first gravity gradient sensing device, invented in 1901 by Loránd Eötvös [20], and torsion balances have still proven to be extremely precise and accurate detectors of gravity. The most precise measurement of  $G$  by far was made by a torsion balance by Gundlach, *et al.*, and a value of  $6.674215(92) \times 10^{-11} \text{ m}^3/\text{kg}/\text{s}^2$  was obtained<sup>4</sup>. However, there are a number of systematics common to all torsion balances, *e.g.* anelasticity in the torsion wire and knowledge of the moment of inertia of the proof mass. For this reason, it is important to compare the macroscopic measurements of torsion balances with the fundamentally different

---

<sup>4</sup>This measurement represents a vast improvement over previous measurements. The introduction of modulation frequency to the measurement by rotating the torsion pendulum is an innovative method of removing biases and allows the nearly part-per-million accuracy to be reached.

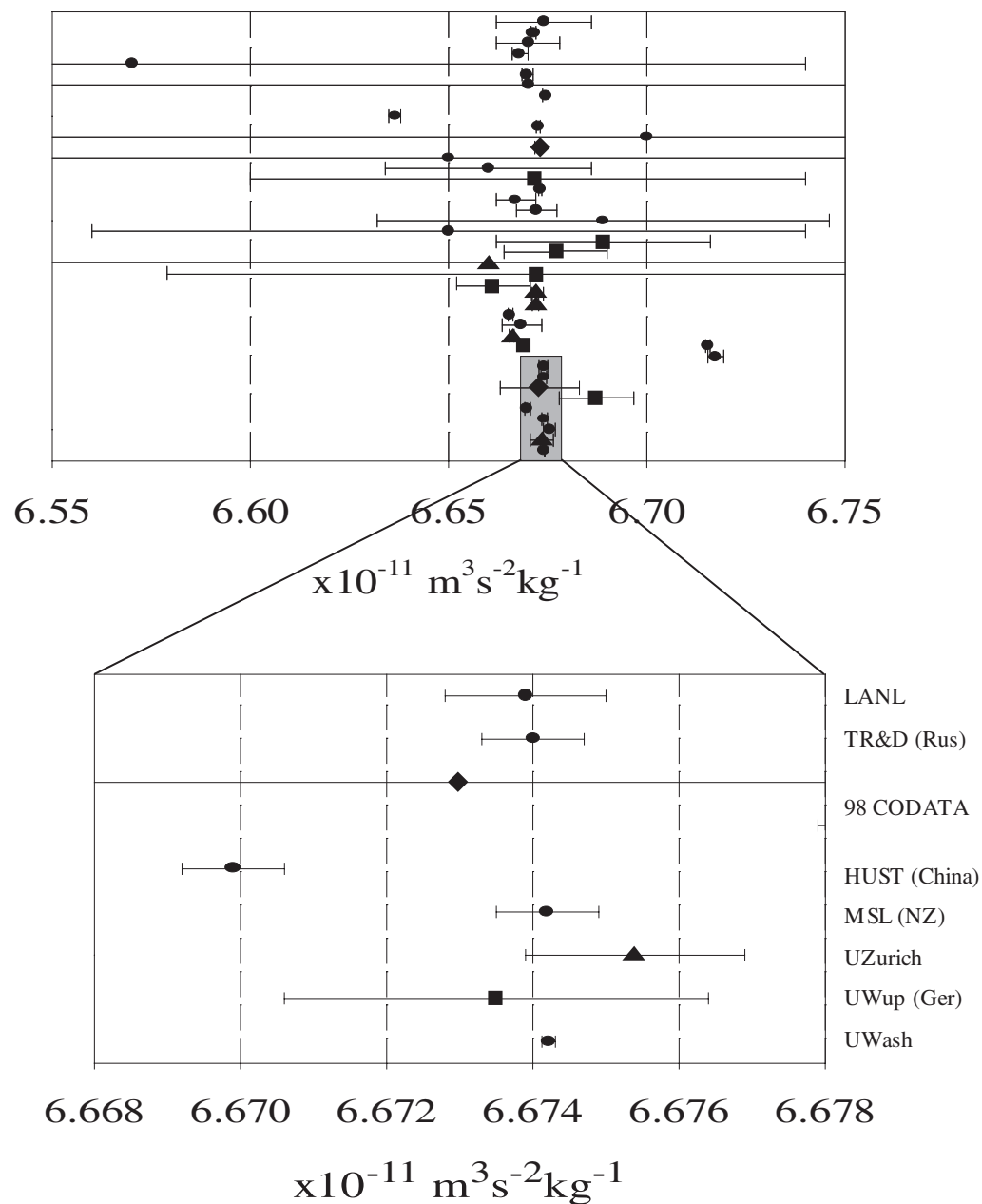


Figure 2.2: A summary of measurements of  $G$  since 1969. The data are from torsion balances (circles), Fabry-Perot cavities (triangles), and other methods (squares). The two most recent CODATA values (diamonds) are included as well. For complete references, see Refs. [25, 32].

microscopic measurements of an atom interferometer.

### 2.3.4 Tests of General Relativity

Another interesting application of the gravity gradiometer described herein are tests of General Relativity. There are string dilaton theories which predict the breakdown of General Relativity [30]. This breakdown could manifest itself in a number of ways, including time variation of  $G$  and thermal dependence of  $G$ . One class of tests seeks to find violations of the inverse square law of gravity. A Yukawa type potential,  $\alpha e^{-r/\lambda}$ , is predicted for wavelength  $\lambda$  less than 1 mm. Tests of the inverse square law at short range could be performed using an atom interferometer gradiometer using test masses extremely close to the atoms.

Additionally, a breakdown of General Relativity can lead to violations of the Equivalence Principle. The strong Equivalence Principle states that all laws of physics hold in all reference frames, while the weak Equivalence Principle (WEP) states that specifically the laws of gravity are true for all reference frames. In other words, the WEP implies that inertial mass is equivalent to gravitational mass, *i.e.* that gravity couples exactly to mass rather than some charge [35]. If there were any composition dependent gravitational forces, then the WEP would be violated. This test is the most sensitive test for General Relativity violations due to the predicted size of the effects. There are predictions of composition dependent differences in gravitational coupling at the  $10^{-12}g - 10^{-21}g$  level [30], just outside of the current limits set by torsion balances [36]. The gravity gradiometer presented herein is an ideal tool<sup>5</sup> for probing the composition dependence of gravity.

### 2.3.5 Fifth force experiments

An intriguing application for a gravity gradiometer is a search for “new physics.” Included in this category are experiments seeking a fifth force. There are theories which predict the existence of weakly interacting bosons called axions [37, 38, 39].

---

<sup>5</sup>This would not technically be a gravity gradiometer, but instead a dual-species differential accelerometer.

Axions might couple spin to matter through a scalar or a pseudo-scalar spin-gravity coupling. Such a coupling to matter could produce a spin-dependent potential of the form

$$U(r) \propto \mathbf{S} \cdot \hat{\mathbf{r}} \left( \frac{1}{\lambda r} + \frac{1}{r^2} \right) e^{-r/\lambda}, \quad (2.2)$$

for a dipole-monopole coupling with range  $\lambda$  between two particles of distance  $\mathbf{r}$ . Using two coupled atom interferometer accelerometers as in the gravity gradiometer, one could attempt to measure such a force or to put limits on the coupling strength. Such a measurement would use one accelerometer as a local oscillator and would compare the gravitational force experienced by atoms in a different spin state. If such an axion coupling existed one might see a change in acceleration between atoms in different spin states in the two interferometers.

## 2.4 Alternate gradiometer technologies

There are only a few different gradiometer technologies with both high precision and accuracy. Part of the reason for the dearth of devices is that gravity gradients are usually small and difficult to resolve. Additionally, vibrations enter the system as a noise component if care is not taken with the measurements, particularly with mechanical devices. This section briefly discusses three existing gradiometers. The difference between absolute and relative gravity gradiometers is highlighted as well.

### 2.4.1 Mass-spring gradiometers

The state-of-the-art in mobile gradiometers is the Universal Gravity Module (UGM) manufactured by Lockheed Martin, which is a device based on mechanical mass-spring accelerometers [40]. The UGM consists of four (or eight) accelerometers on a rotating platform. The accelerometers are devices which each capacitively measure the acceleration of a precisely machined proof-mass mounted on a spring. The accelerometers are rotated to reject systematic drifts as well as to calibrate the device with the known centrifugal acceleration produced by rotation. The sensitivity of this device ranges from  $2 \text{ E}/\sqrt{\text{Hz}}$  to  $20 \text{ E}/\sqrt{\text{Hz}}$  depending on the device baseline

and the vibration environment, and the accuracy is limited to around 10 E [41]. This device is currently employed for a variety of field applications including airborne oil and mineral detection (BHP Falcon Project) [42], land-based underground structure detection [43], and for navigational purposes aboard ballistic missile submarines [44].

### 2.4.2 Superconducting instruments

The leading device for short-term sensitivity is a superconducting gravity gradiometer [45]. The superconducting gradiometer levitates two superconducting macroscopic machined proof masses in a magnetic field using the Meissner Effect. The acceleration of the two masses is detected using two superconducting quantum interference devices (SQUIDS) which monitor the changing magnetic flux through current-carrying loops as the proof masses change position, and the differential acceleration constitutes the gradient signal. The SQUID loops are coupled so as to remove common-mode vibrations of the two masses. The short-term sensitivity of this device is  $\sim 0.1 \text{ E}/\sqrt{\text{Hz}}$ . The superconducting gradiometer is primarily limited by its poor long-term performance. The accuracy and stability are limited by severe  $1/f$  noise coming from the tare effect in superconductors, as well as the susceptibility of the device to mechanical and thermal shock [46, 47]. This drift, plus the necessity for large dewars of liquid helium, make the superconducting gradiometer impractical for use on mobile platforms.

### 2.4.3 Falling cornercube gradiometer

There is an absolute accelerometer that measures the acceleration of a falling cornercube in one arm of a Michelson interferometer. The chirp rate of the optical fringes is directly proportional to the acceleration experienced by the cornercube. By stacking two such accelerometers on top of each other and using the differential chirp rate, the gravity gradient is measured [48]. The currently demonstrated sensitivity of the falling cornercube gravimeter is only  $400 \text{ E}/\sqrt{\text{Hz}}$  however, and it remains to be seen if the device can reject common-mode vibrations effectively. The stability of the falling cornercube gradiometer should be excellent, as it references its calibration to the wavelength of light used.

### 2.4.4 Absolute gradiometry

All of the gravity gradiometers developed previously, save the falling cornercube gradiometer, are gradiometers that require periodic calibration and suffer from drift<sup>6</sup>. The atom interferometer gradiometer is the first demonstration of an absolute accelerometer. The calibration is referenced to the wavelength of the light used in the interferometer. The lasers are stabilized to a well known atomic transition in Cs, and their frequency is stable over long times. There is a popular saying in the inertial force sensing community that “all inertial force sensors are good thermometers,” due to their sensitivity to temperature change. However, that proves not to be the case with the light-pulse method of gradiometry, which is insensitive to drifts from environmental effects such as temperature and magnetic fields. The falling cornercube device also references its calibration to the wavelength of the light used and should be stable as well. An absolute accelerometer improves productivity by not requiring the return to previous data sites for recalibration. Additionally, an absolute device is essential for long-term use in inertial navigation systems and for scientific measurements with long integration times.

---

<sup>6</sup>These gradiometers are called relative gradiometers.



# Chapter 3

## Laser Cooling and Trapping

The goal of this section is to describe the basic atom-photon interactions, called atom optics, which are used throughout the experiments described in Chapter 5. This chapter summarizes some basic tools of modern atom physics and describes the results of the theoretical descriptions of them. There are a number of comprehensive references that derive the results presented herein from first principles [49, 50], and the reader is directed to them for complete derivations. The layout of the chapter is as follows: first the structure of atoms is reviewed, and their basic behavior in optical fields is summarized. Next is a description of optical forces on atoms and how they are used to cool and confine atoms. Finally, a summary of the two-photon Raman interactions used for the interferometer itself is given.

### 3.1 Atomic structure

In this dissertation, only alkali atoms will be considered, as they are the simplest to deal with and most convenient. The atomic structure of all alkali atoms is a closed inner shell plus the outermost electron in an S-shell. All alkali atoms are characterized by two hyperfine ground state levels separated by a few gigahertz, corresponding to a spin-flip of the valence electron, followed by a large spacing to the next allowed transitions, the  $D_1$  and  $D_2$  lines in the optical regime. This level spacing makes alkali

atoms particularly convenient to deal with, as they may effectively be treated as two-level atoms in certain situations. The hyperfine structures only need be included in a few specific calculations and are not necessary to derive many of the basic equations for light forces on atoms.

Cesium (Cs) atoms are used exclusively in the experiments presented here. The two hyperfine ground states of Cs are the  $6S_{1/2}$   $F = 3$  and  $F = 4$  levels, which are separated by a 9.2 GHz microwave spin-flip transition.  $F$  is the total angular momentum of the atom,  $F = J + I$ , where  $I = 7/2$  is the nuclear spin. The electron angular momentum is  $J = L + S$ ;  $L$  and  $S$  are the spin-orbit coupling and the electron spin respectively. It is this hyperfine splitting frequency that is the basis for the System Internationale definition of the second. This frequency is a defined quantity, and the Cs hyperfine transition is the basis for all primary time standards. The  $D_2$  line to the  $6P_{3/2}$  manifold is used for the cooling transition at 852 nm. The excited manifold has 4 hyperfine states  $F' = 2, 3, 4$ , and 5. The prime notation is used to denote the excited manifold throughout this dissertation. In the presence of a magnetic field, each hyperfine level is split further into  $2F+1$  Zeeman sublevels. These sublevels are degenerate with no magnetic field. See Appendix A for the detailed atomic structure of Cs, as well as for the physical properties of Cs.

## 3.2 Two-level atoms

The behavior of an ideal two-level atom in the presence of a single-frequency electric field is presented here to demonstrate the phenomenon of Rabi flopping. The ground and excited states are denoted  $|g\rangle$  and  $|e\rangle$  respectively. In the semi-classical approximation where the electric field is treated as a classical field, the Hamiltonian for such an atom in the presence of the field is:

$$H = \hbar\omega_g|g\rangle\langle g| + \hbar\omega_e|e\rangle\langle e| + \mathbf{d} \cdot \mathbf{E}. \quad (3.1)$$

The first two terms represent the internal energy of the two states,  $\hbar\omega_g$  and  $\hbar\omega_e$ , while the third term is the interaction between the electric dipole moment of the atom  $\mathbf{d}$

and the electric field

$$E = E_0 \cos(kx + \omega t). \quad (3.2)$$

The dipole interaction of the atom with the electric field gives an off-diagonal matrix element of:

$$\Omega_r = -\frac{\langle e | \mathbf{d} \cdot \mathbf{E} | g \rangle}{\hbar}, \quad (3.3)$$

which is the Rabi frequency for oscillation between the ground and excited state for resonant light, *i.e.* when  $\omega = \omega_e - \omega_g$  [49]. Spontaneous emission has been neglected here.

Using this Hamiltonian, the time-dependent Schrödinger Equation can be solved. The full details of this solution are outside of the scope of this dissertation, and the results will be summarized here. A complete description of Rabi flopping in a two-level atom can be found in [51, 49]. By applying the rotating wave approximation, shifting the arbitrary overall energy of the system, and transforming coordinates the problem can be reduced to a simple solution. Using the initial condition that the atom starts in the ground state  $|g\rangle$ , the probability of the atom being in the excited state after being exposed to the laser field for time  $t$  is given by:

$$P_e(t) = \frac{1}{2} \left[ 1 - \frac{\Omega_r^2}{\Omega'^2} \cos(\Omega' t) \right], \quad (3.4)$$

where  $\Omega'_r$  is the general expression for the Rabi frequency. Defining the detuning from resonance as  $\Delta = \omega - (\omega_e - \omega_g)$ , the generalized Rabi frequency is  $\Omega'_r = \sqrt{\Omega_r^2 + \Delta^2}$ . A similar formula is true for finding the transition probability to the ground states if the initial condition is  $|e\rangle$ . Additionally, the energy levels of the atom are shifted in the presence of light field, called the AC Stark effect, by an amount:

$$U_g^{\text{AC}} \simeq \frac{\hbar \Omega_r^2}{4\Delta}. \quad (3.5)$$

The AC Stark shift for the excited state is in the opposite direction as that for the lower state:  $U_e^{\text{AC}} = -U_g^{\text{AC}}$ . Equation 3.5 is only valid in the limit of large detuning. Following Equation 3.4, an atom in the ground or excited state illuminated with

resonant light for a time  $t = \pi/\Omega_r$  will be transferred to the opposite state with 100% probability; such a pulse is called a  $\pi$  pulse. If the atom is illuminated for time  $t = \pi/2\Omega_r$ , then the atom will be in an equal coherent superposition of the ground and excited states, and this pulse is called a  $\pi/2$  pulse. The terms  $\pi$  pulse and  $\pi/2$  pulse are borrowed from nuclear magnetic resonance terminology and refer to the pulse area. In practice, dephasing must be included due to effect like spontaneous emission and various inhomogeneous broadening, which causes the amplitude of the Rabi flopping to decrease.

An important concept to define is that of saturation of the atomic transition by the electrical field. Because the atom has a finite natural lifetime<sup>1</sup>  $\tau_n$ , it can spend at most half of the time in the excited state under incoherent scattering processes. This means that after a point, the scattering rate ceases to increase as the intensity of the driving field is increased. This phenomenon is called saturation, and the intensity at which the probability of finding the atom in the excited state is 1/4 is defined as the saturation intensity [52],

$$I_{\text{sat}} = \hbar c k^3 \frac{\Gamma_n}{2\pi}. \quad (3.6)$$

For the Cs  $F = 4 \rightarrow F' = 5$  transition,  $\Gamma_n = 2\pi \times 5.3$  MHz, and  $I_{\text{sat}} = 1.12$  mW/cm<sup>2</sup>.

### 3.3 Optical forces

There are two main forces due to light acting on atoms: scattering forces and dipole forces. Because the atoms are neutral, DC electrical forces are negligible unless extremely high electrical fields are present. The nature of each of the two primary forces is discussed here.

#### 3.3.1 Scattering force

The scattering force arises from the scattering of photons by an atom [49]. If a photon from a resonant or near-resonant travelling-wave laser beam is absorbed by the atom, through conservation of momentum, the atom receives a momentum kick

---

<sup>1</sup>The natural lifetime is the reciprocal of the natural linewidth, *i.e.*  $\tau_n = 2\pi/\Gamma_n$ .

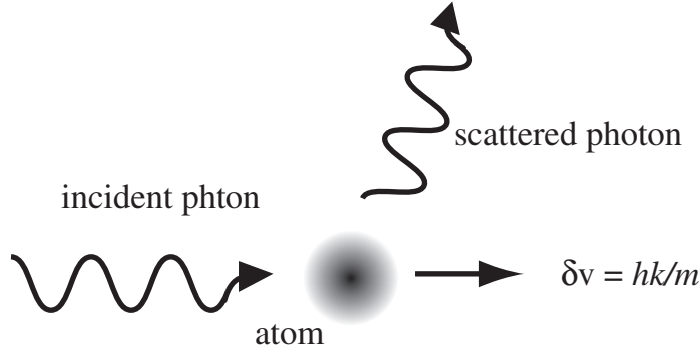


Figure 3.1: An atom absorbs a photon and receives a momentum kick, altering its velocity by  $\hbar k/m$ . The direction that the scattered photon is spontaneously emitted into is random, and no net momentum is transferred in this process.

of  $\hbar \mathbf{k}$  in the direction of the photon wavevector  $\mathbf{k}$ . The atom then decays back to the original state via spontaneous emission. The spontaneously emitted photon has a random direction, and when averaged over many absorption-emission events, no net momentum is transferred to the atom via spontaneous emission. This process is depicted in Fig. 3.1.

The force exerted on an atom illuminated for a time much longer than the natural lifetime of the transition is equal to the product of the rate of photon scattering with the average momentum transfer per scattering event. The scattering rate is given by

$$\Gamma_{\text{scat}} = \frac{1}{\tau_{\text{scat}}} = \frac{\Gamma_n}{2} \left[ \frac{I/I_{\text{sat}}}{1 + I/I_{\text{sat}} + 4(\Delta/\Gamma_n)^2} \right], \quad (3.7)$$

and thus the scattering force is

$$\mathbf{f}_{\text{scat}} = \frac{\hbar \mathbf{k}}{\tau_{\text{scat}}} = \frac{\hbar \mathbf{k} \Gamma_n}{2} \left[ \frac{I/I_{\text{sat}}}{1 + I/I_{\text{sat}} + 4(\Delta/\Gamma_n)^2} \right]. \quad (3.8)$$

The intensity of the driving field is  $I$ , and the detuning from resonance is  $\Delta$ . At saturation intensity, resonantly driving the Cs  $F = 4 \rightarrow F' = 5$  transition gives an acceleration of  $\sim 5000$  g. The scattering force is a dissipative force, as the atom couples to the vacuum field via spontaneous emission. This is a necessary aspect for laser cooling; there can be no cooling without some dissipation mechanism.

It should be noted that the  $F = 4 \ m_F = 4 \rightarrow F' = 5 \ m_F = 5$  transition is a closed transition for  $\sigma^+$  circularly polarized light (or  $F = 4 \ m_F = -4 \rightarrow F' = 5 \ m_F = -5$  for  $\sigma^-$ ) due to selection rules. In the limit of perfectly polarized light, the atom will cycle repeatedly through this transition. In practice, after many scattering events, the atom will optically pump to the  $F = 3$  state via a near-resonant transition from the  $F = 4 \ m_F = 4 \rightarrow F' = 5 \ m_F = 4$  due to a small component of linearly polarized light. The atom can then spontaneously emit down to the  $F = 3$  state, where it is unaffected by the laser. Thus, in an experimental situation, the addition of a repumping beam tuned to the  $F = 3 \rightarrow F = 4$  transition is necessary to repump the atoms out of the dark state so they continue to scatter photons on the cycling transition.

### 3.3.2 Dipole force

Next consider the case of an atom in an oscillating electric field that is spatially varying. The field shifts the energies of the atomic states by the AC-Stark potential (see section 3.2). The spatially varying electric field causes the atom to experience a force as given by the gradient of the potential,

$$\mathbf{f}_{AC} = -\nabla U_{AC} \simeq \frac{\Omega_r^2}{\Delta} \simeq -\frac{\hbar \Gamma_n^2}{2\Delta I_{sat}} \nabla I(r). \quad (3.9)$$

This means that an intensity gradient in a light field produces a force on an atom. This force, called the dipole force, can be thought of in terms of the field polarizing the atom and then exerting a force on the induced dipole. The dipole force can be used to trap atoms at the focus of an intense beam [53]. However, for the purposes of the experiments contained herein, the dipole force is an unwanted potential systematic effect but is typically negligible for the intensity gradients involved.

## 3.4 Magnetic forces

An atom with a magnetic moment  $\mu$  in a magnetic field  $\mathbf{B}$  will experience an energy shift that can be calculated by adding a magnetic field as a perturbation to the Hamiltonian. The potential energy shift due to the magnetic field is  $U_{\text{mag}} = -\mu \cdot \mathbf{B}$ .

The magnetic moment is given by  $\mu = m_F g_F \mu_B$ , where  $m_F$  is the quantum number of the Zeeman sublevel,  $g_F$  is the corresponding Landé g-factor, and  $\mu_B$  is the Bohr magneton. Calculations of the Landé g-factor can be found in many textbooks [49]. The g-factors of the two hyperfine ground states have opposite sign, meaning that the Zeeman shift is opposite for the Zeeman sublevels of the  $F = 3$  and  $F = 4$  states. The magnetic moment of ground state Cs atoms, in practical units, is  $m_F \times 350$  kHz/G. Atoms in the  $m_F = 0$  sublevel experience no first-order Zeeman energy shift. The perturbative approximation used to calculate the the energy shift must be carried out to second order in the magnetic field, and this energy shift is the second-order Zeeman effect. For Cs atoms in the  $m_F = 0$ , this shift is  $U_{\text{mag}} = 2\pi\hbar\beta B^2$ , where  $\beta = 400$  Hz/G<sup>2</sup>.

The force exerted by a magnetic field on an atom is given by the gradient of the magnetic potential,  $F = -\nabla U_{\text{mag}}$ . A static magnetic field exerts no force on a neutral atom, but a spatial field gradient will exert a force on an atom with a magnetic moment. Magnetic forces are used extensively in other atom trapping work [54], particularly Bose-Einstein condensation (BEC) related work [55]. However, in this experiment, they are only considered in the context of harmful systematic forces acting on the atoms.

## 3.5 Laser cooling

### 3.5.1 Doppler cooling

The scattering force is a dissipative force, and it can be used to cool atoms, *i.e.* to remove much of their kinetic energy<sup>2</sup>. Consider the situation depicted in Fig. 3.2, of an atom travelling towards a laser beam that is red-detuned from a closed cooling transition. The detuning seen by the atom will be modified by the Doppler shift  $\mathbf{k} \cdot \mathbf{v}$  due to the atom's velocity  $\mathbf{v}$ . The effective detuning for determining the scattering rate and scattering force is  $\Delta - \mathbf{k} \cdot \mathbf{v}$ . There are two effects of the Doppler-shifted detuning. The primary effect is that the laser will be Doppler-shifted towards

---

<sup>2</sup>The cooling discussed here damps the atom's center of mass motion.

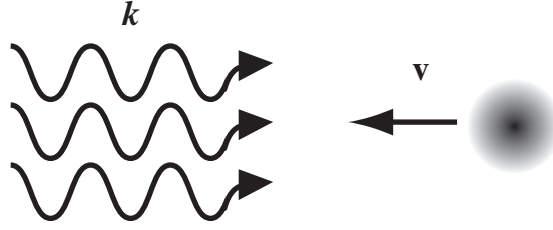


Figure 3.2: An atom moving towards a red-detuned beam will be Doppler shifted towards resonance by an amount  $\mathbf{k} \cdot \mathbf{v}$ .

resonance and will scatter more photons from faster moving atoms. The second is that the atom will absorb a red-detuned photon and then spontaneously emit a photon of higher frequency, resulting in a net energy loss regardless of the scattered direction, so long as the atom is moving faster than the photon recoil velocity. Over many cycles, the momentum given to the atom from spontaneous emission events average to zero, while the atom receives many photon recoils in the direction opposite to its velocity, along the direction of the laser beam. This mechanism is called Doppler cooling [49].

An optical molasses is created by intersecting three pairs of opposing red-detuned laser beams [5]. Any direction an atom moves in the optical molasses is viscously damped by the red-detuned beam opposing the motion. Because it is impossible to make perfectly circularly polarized beams to drive the closed cycling transitions, atoms will eventually pump into states that are dark to the molasses ( $F = 3$  states) and escape. The addition of a repumper beam tuned to the  $F = 3 \rightarrow F = 4$  transition pumps the atoms back into bright states<sup>3</sup> again. Atoms will undergo a random walk through the molasses due to the photon recoils from the spontaneous scattering; this random walk limits the Doppler cooling temperature to be

$$T_D = \frac{\hbar \Gamma_n}{2k_B}. \quad (3.10)$$

Additionally, there is no restoring force in an optical molasses, only viscous confinement, so atoms will eventually be ejected from the molasses during their random walks.

---

<sup>3</sup>Bright states scatter photons from a laser beam, while dark states do not due to selection rules.



### 3.5.2 Polarization gradient cooling

Early experimenters using optical molasses were astonished to find temperatures much lower than the Doppler cooling limit inside of optical molasses [56]. Temperatures more than an order of magnitude lower than  $T_D$  were observed. This extra cooling mechanism is called polarization gradient cooling, or Sisyphus cooling, and can only be understood by leaving the framework of the two-level atom. The mechanism of polarization gradient cooling is fundamentally different from Doppler cooling and is due to the non-adiabatic trajectory of an atom moving through a spatially varying light field. Such a spatially varying light field can be constructed with two counter-propagating travelling waves of  $\sigma^+ - \sigma^-$  polarizations or crossed-linear polarizations (called  $\text{lin} \perp \text{lin}$ ). Only the  $\sigma^+ - \sigma^-$  case is considered here.

The sum of the two  $\sigma^+ - \sigma^-$  polarized beams is a light field of linear polarization that rotates in space at a period of every  $\lambda/4$ . The principle of polarization gradient cooling relies on the AC Stark shift. The spatially varying polarization also creates a spatially varying AC Stark shift. At a given position in the field, the atomic population distributes itself in a particular way among the magnetic sublevels. As the atom moves to a different part of the field, the population distribution is no longer the lowest energy state for the new AC Stark shifts. The important point is that the atom moves *nonadiabatically* through the field, *i.e.* the atom moves fast enough that the population does not have time to redistribute. When the atom does decay, it will be into a lower energy state due to the different field configuration at its location. The atom will lose energy irrevocably to the vacuum field, dissipating its kinetic energy even further. For a full description of polarization gradient cooling, see [57, 58].

Below the Doppler limit, polarization gradient forces dominate. Polarization gradient cooling scales according to

$$T_{\text{PG}} = \frac{\hbar \Omega_r^2}{k_B \Delta}. \quad (3.11)$$

This means that the lowest temperatures are reached with large detuning and low light intensities. Polarization gradient cooling does have a fundamental limit. It

cannot cool below the limit of several photon recoils,

$$T_{\text{rec}} \equiv \frac{(\hbar k)^2}{2k_B m} \quad (3.12)$$

where  $m$  is the mass of the atom. At these temperatures, the behavior of the atom in the varying field, particularly in a three dimensional molasses, is complicated, and a more involved treatment is necessary. Also, as with Doppler cooling, there is no restoring force in polarization gradient cooling, and the atom will randomly walk through the viscous confinement until it leaves the molasses region. Again, a repumper is required with polarization gradient cooling to keep the atoms from pumping into a dark state.

## 3.6 Magneto-optical trapping

Optical molasses is a an effective tool for dissipating the energy of atoms and cooling them to ultra-cold temperatures. However, there is no restoring force to localize the atoms and allow a large number to be collected. The optical Earnshaw theorem states that it is not possible to trap atoms with light forces as long as the trapping force is proportional to the intensity of the light [59]. This is easy to see: for any given trapping volume, the optical energy entering the volume is the same as that leaving the volume, thus there is no position with force vectors pointing inwards from all directions. However because of the multiple atomic ground states, the addition of a magnetic field gradient with a field minimum in the center of the intersecting molasses laser beams provides an energy minimum and a restoring force that allows a large number of atoms to be confined. This magnetic field is a spherical quadrupole field created by two opposing coils of current-carrying wire in an anti-Helmholz configuration. The spherical quadrupole has a field zero at the intersection of the beams and a linearly increasing field directed radially outward.

To understand the trapping mechanism of a MOT, consider the one-dimensional case depicted in Fig. 3.3. The magnetic field gradient changes the effective detuning seen by an atom as it moves away from the field zero in the center, via the Zeeman

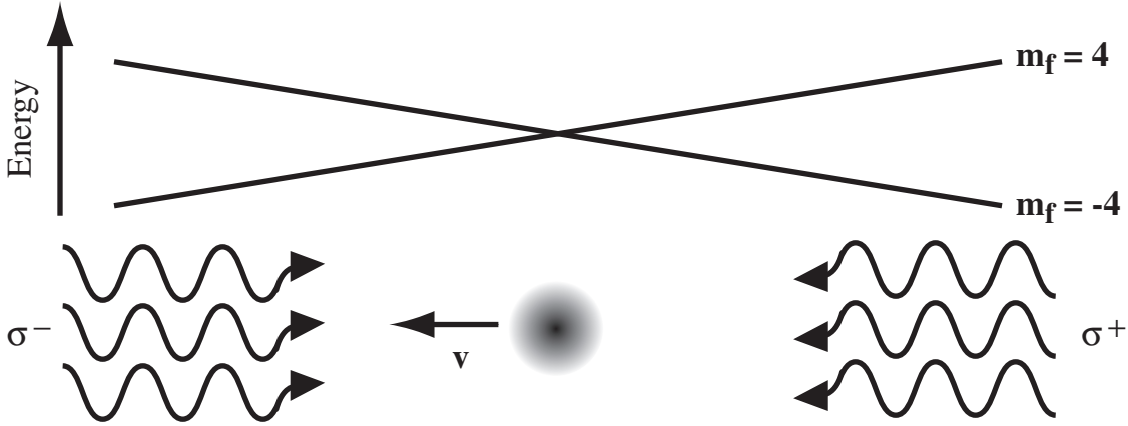


Figure 3.3: Illustration of an atom in a 1D MOT consisting of an opposing pair of  $\sigma^+ - \sigma^-$  polarized beams and a magnetic field increasing linearly with position from left to right (not shown). The Zeeman shifted energy of the  $F = 4$   $m_F = \pm 4$  states are shown as a function of position. The because the beams are red-detuned, the higher energy states are closer to resonance, linearly proportional to their distance from the field zero at the trap center.

shift, proportionally to its distance from the field zero, thereby lifting the degeneracy of the magnetic sublevels of each hyperfine state. An atom moving to the left in the figure will have the extreme Zeeman sublevel of the  $F = 4$  manifold,  $m_F = -4$ , shifted closer to resonance of the red-detuned optical fields by the magnetic field. Because of the relative strengths of the transition matrix elements for red-detuned  $\sigma^+$  and  $\sigma^-$  polarized light, as well as the Doppler shift, the atom will preferentially scatter light from the  $\sigma^+$  polarized beam towards which it is moving. This preferential scattering provides a force directed back towards the trap center, and the transition is a closed cycling transition, so many photons will be scattered. On the opposite side of the center of the trap, the same principle applies, but with the  $\sigma^-$  polarized light scattering preferentially off of the  $m_F = 4$  state which is now Zeeman shifted closest to resonance. The principle of a 3D MOT is identical with three pairs of opposing  $\sigma^+ - \sigma^-$  polarized beams.

MOTs have been shown to exhibit complex dynamics, including polarization gradient cooling, radiation pressure, and three-body collisions. However for the purposes of this dissertation, MOTs can be viewed as a robust source of ultra-cold atoms.

### 3.6.1 Trap loading

Atoms can be loaded into a MOT from a variety of sources. The simplest source is a thermal vapor [6]. A low pressure thermal vapor of atoms is introduced into the vacuum chamber. Atoms which enter the intersection of the trapping beams will be captured if their velocity is low enough. In practice, this amounts to trapping only the slow-atom tail of the Maxwell velocity distribution, which is sufficient for obtaining large numbers. In order to build up a large enough vapor pressure, the walls of the vacuum chamber must be coated with a mono-layer of atoms in order for a vapor cell to be established. Otherwise, the clean vacuum chamber walls themselves are an effective pump for alkali atoms. Other loading sources include beam loading, filament loading, and loading from other pre-loaded atom traps. Vapor cell loading is used exclusively in this dissertation.

The loading rate is primarily determined by only a few physical parameters relating to the trapping laser beams and the partial pressures of gases in the vacuum chamber [60]. The steady-state number of trapped atoms occurs at the point where the loading rate is balanced by the loss rate. The loading rate is determined by the density  $n$  and most probably velocity  $u$  of the Cs atoms as well as the parameters of the trapping lasers, *i.e.* the diameter  $d$  of the beams, the scattering rate for the cooling transition, and the recoil velocity  $v_{\text{rec}}$  of the atoms after a scattering event:

$$\Gamma_{\text{load}} = \frac{4nd^4\Gamma_{\text{scat}}^2 v_{\text{rec}}^2}{u^3}. \quad (3.13)$$

The primary loss mechanism in MOTs is collisions with untrapped atoms in the background gas. In a vapor cell MOT, these atoms are usually untrapped Cs atoms if the pressure of other background gases is sufficiently low. The collision rate is:

$$\Gamma_{\text{col}} \simeq n_{\text{back}}\sigma u, \quad (3.14)$$

where  $n_{\text{back}}$  is the total density of all background gases including the Cs vapor, and  $\sigma$  is the cross section for a background collision that ejects an atom from the trap.

The steady-state trap population is then given by:

$$N_{\text{ss}} = \frac{\Gamma_{\text{load}}}{\Gamma_{\text{col}}} = \frac{4d^4\Gamma_{\text{scat}}^2 v_{\text{rec}}^2}{\sigma u^4} \left( \frac{n}{n_{\text{back}}} \right). \quad (3.15)$$

In the limit where the Cs vapor pressure is small, the steady-state population is linearly dependent on the Cs pressure. The opposite limit is rather surprising: if the Cs vapor pressure is much larger than that of the other background gases, the total steady-state population is independent of the Cs pressure. This limit has larger steady-state populations as well. In practice this experiment is operated in the middle region where both the Cs vapor pressure and the background gas pressure need to be taken into consideration. There is also an upper bound on the Cs vapor pressure. If the background collision rate is faster than the time it takes to slow and trap a Cs atom, then a MOT is not possible. Experimentally, this high pressure cut-off occurs around  $10^{-7}$  torr. There is also a interferometric phase shift produced from collisions with other atoms, but this effect is dominated by collisions with cold atoms instead of the thermal background atoms at the standard operating pressures. Also of note is the large dependence on the size of the trapping beams. This size is the most important parameter to collect large numbers of atoms in a MOT.

### 3.6.2 Atomic fountains

Often experiments using trapped atoms require long interrogation times, particularly interferometers. If all the trapping fields are turned off, the laser-cooled atoms begin accelerating under the influence of gravity. Gravity causes the atoms to accelerate away from the experiment region of the vacuum chamber and become inaccessible to manipulation and detection after only tens of milliseconds. However, if the atoms are accelerated upwards before being released from the optical molasses they will follow ballistic trajectories and return to the initial trapping region after a time as long as a second. This allows for increased interaction time which is critical for the performance of highly sensitive interferometers. Such optically induced ballistic trajectories are called atomic fountains, and were first demonstrated in 1989 by Chu and Kasevich [61].

The atomic fountain is implemented as follows. After loading a MOT, the magnetic field is turned off, leaving the atoms confined in an optical molasses. If the downward pointing beams are detuned further from resonance than the upward pointing beams, the downward pointing beams will transfer less momentum to the atoms than the upward pointing beams, providing a net force upwards. This configuration results in a molasses moving upwards at a velocity given by the frequency difference between the upward and downward pointing beams. For the configuration shown in Fig. 3.4a the velocity of the molasses is simply

$$v = \frac{\delta\omega}{k} \quad (3.16)$$

for a frequency difference  $\delta\omega$  and an average wavevector  $k$ . This launching configuration has been shown to heat the atoms and is more difficult to work with than the following scheme. The (1,1,1) MOT configuration<sup>4</sup> shown in Fig. 3.4b does not significantly heat the atoms and is more robust to beam pointing instabilities. The velocity in this case is

$$v = \frac{\delta\omega}{k \sin\left(\frac{\pi}{3}\right)}. \quad (3.17)$$

The extra factor in the denominator is a geometric factor accounting for the projection of momenta onto the vertical axis. After the atoms are in the moving molasses, the launching light can be shut off, and the atoms will follow ballistic trajectories under the influence of gravity with the initial velocity of the moving molasses. Using such an atomic fountain is an effective tool to dramatically increase interaction times for cold atom experiments which require long interrogation times.

### 3.7 Two-photon stimulated Raman transitions

Raman transitions are a type of inelastic scattering of a light field by an atom. Through the process, the atom gains or loses energy, and thus has its momentum

---

<sup>4</sup>The notation (1,0,0) and (1,1,1) is taken from crystal geometries in condensed matter physics.

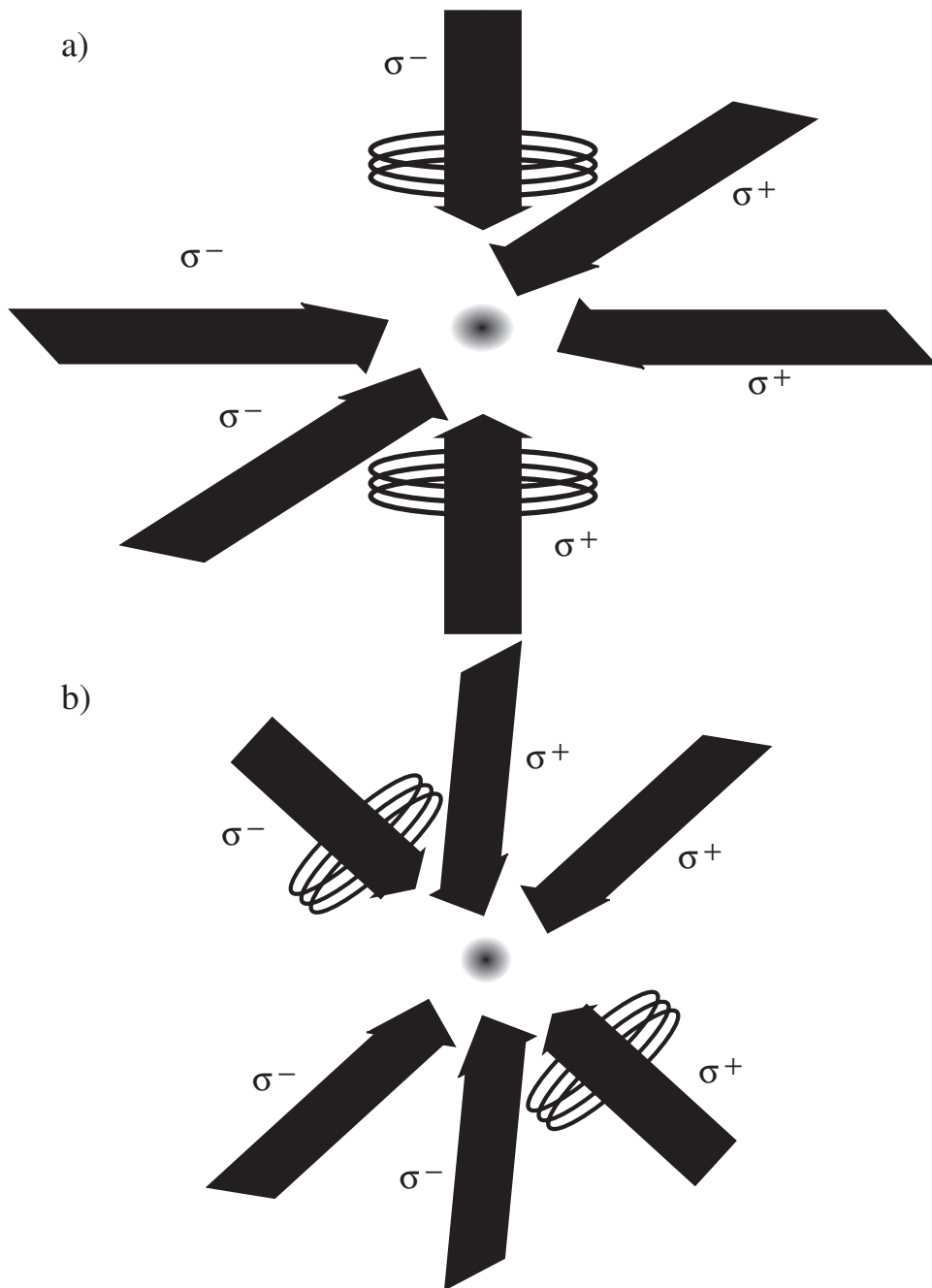


Figure 3.4: Beam geometries for three dimensional MOTs. The anti-Helmoltz coils that generate the trapping field are shown, and the polarization of the beams is noted. a) The (1,0,0) configuration with beams along the principal x, y, and z axes. b) The (1,1,1) configuration with all beams equally spaced by  $120^\circ$ .

altered by the scattering event. In particular, two-photon stimulated Raman transition will be discussed, as these are the transitions that are used in the interferometer [62, 14]. When an atom is illuminated with a light field of two frequencies whose sum or difference frequency is near an allowed transition, the atom absorbs a photon of frequency  $\omega_1$  from one of beam and is stimulated to emit a photon of frequency  $\omega_2$  in the direction of the second beam. In order for two-photon Raman scattering to occur, the two beams must be close to an allowed transition, called the intermediate state  $|i\rangle$ , but far enough from  $|i\rangle$  so that spontaneous emission is negligible. Of particular interest is the situation when the two Raman beams are counterpropagating, *i.e.*  $\mathbf{k}_1 \simeq -\mathbf{k}_2$ . In this configuration, the momentum recoil from the absorption and emission processes are both in the same direction. This recoil gives a relatively large momentum kick to the atom, and the Doppler sensitivity of this transition is twice the sensitivity of a one-photon transition. This special case of two-photon transitions will be considered below.

The theory of two-photon stimulated Raman transitions will not be presented here, but the results will be summarized. A complete description may be found in [52, 63]. The results for a two-photon stimulated Raman transition for an atom in a hyperfine state to another hyperfine state are presented. The frequency difference of the two Raman beams must be near the hyperfine frequency. In order to obtain the transition rate, the intermediate state is adiabatically eliminated in the interaction picture. Additionally, the electric dipole approximation and the rotating wave approximation are used, and spontaneous emission is neglected. The transition rate, *i.e.* the two-photon Rabi frequency, is

$$\Omega_{\text{eff}} = \frac{\Omega_{gi}\Omega_{ie}}{\Delta_{eg}}, \quad (3.18)$$

where  $\Omega_{gi}$  and  $\Omega_{ie}$  are the single-photon Rabi frequencies between the hyperfine states  $|g\rangle$  and  $|i\rangle$ , and  $|i\rangle$  and  $|e\rangle$  respectively<sup>5</sup>. The energy level diagram is shown in Fig. 3.5. The two-photon detuning is

---

<sup>5</sup>The two states  $|g\rangle$  and  $|e\rangle$  correspond to the two hyperfine levels  $F = 3$  and  $F = 4$ , usually the  $m_F = 0$  Zeeman sublevel of each, and the equations are symmetric with respect to driving the reverse transition, *i.e.* from  $|e\rangle$  to  $|g\rangle$ .



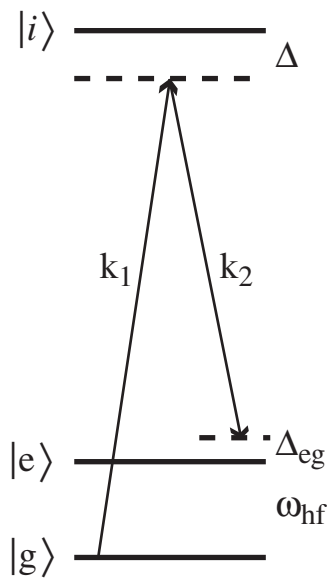


Figure 3.5: Energy level diagram for Raman transitions. The detuning  $\Delta$  of the virtual state is large compared to the two photon Rabi frequency, but small compared to the energy spacing between it and levels  $|e\rangle$  and  $|g\rangle$  (which is an optical transition in this experiment). The two-photon detuning  $\Delta_{eg}$  is shown, and is usually set to zero for driving transitions.

$$\Delta_{eg} = \omega_1 - \omega_2 - \left[ \omega_{\text{hf}} + v(k_1 - k_2) + \hbar \frac{(k_1 - k_2)^2}{2m} \right] + \Omega_{\text{AC}}. \quad (3.19)$$

The terms are, in order, the frequency difference of the two beams, the hyperfine splitting, the total Doppler shift of the two beams from the velocity component of the atoms along the propagation axis of the beams, the recoil shift from the momentum transfer by the two-photon scattering, and the AC Stark shift. The AC Stark shift is the sum of the one-photon AC Stark shifts:

$$\Omega_{\text{AC}} = \sum_{j=e,g} \frac{\Omega_{ji}^2}{4\Delta_{ji}}, \quad (3.20)$$

and typically the detuning has opposite sign for the two levels. Thus it is possible to null the AC Stark shift by adjusting the relative Rabi frequencies of the two Raman beams, *i.e.* by adjusting the beam balance. Finally, in the case of multilevel atoms, the transition rates and AC Stark shifts must be summed over all possible intermediate states.

In the limit where the two-photon detuning is zero, the transition equations for Raman lasers acting on the ground and excited states have a particularly simple form. In this case, state  $|\psi\rangle$  of an atom initially in state  $|g\rangle$  at time  $t_o$  after being illuminated by the resonant Raman lasers for time  $\tau$  is

$$|\psi(t_o + \tau)\rangle = \cos(\Omega_{\text{eff}}\tau/2) |g\rangle - i \sin(\Omega_{\text{eff}}\tau/2) e^{\phi} |e\rangle, \quad (3.21)$$

and for an atom initially in  $|e\rangle$ , the final state is given by

$$|\psi(t_o + \tau)\rangle = -i \sin(\Omega_{\text{eff}}\tau/2) e^{-\phi} |g\rangle + \cos(\Omega_{\text{eff}}\tau/2) |e\rangle. \quad (3.22)$$

Here  $\phi$  is the phase of the Raman lasers at the position of the atomic center of mass wavepacket. These transition equations can be summarized as follows: under a two-photon Raman transition, the wavepacket remaining in the initial state has no phase shift as a result of the interaction with the light, and the wavepacket making a transition to the other state picks up a phase factor of  $\pm\phi$  depending on whether the

atom was initially in the ground or excited state.

To summarize, stimulated, two-photon Raman transitions are useful tools for coherent manipulation of atoms. They transfer relatively large momenta to atoms and have high Doppler sensitivity. Also, the frequency difference of the two beams is the important quantity in the detuning of the lasers. This means that each laser does not have to be stabilized to a part in  $10^{15}$ , but rather that their frequency difference has to be stabilized to the same sub-Hertz level, or only a part in  $10^{10}$ . Finally, there are simple transition rules governing the atomic phase under a Raman transitions that make interferometer phase calculations straightforward.

### 3.8 Atom detection

It is essential to be able to read out the populations of the atomic states following an experiment. In a precision measurement this must be done as cleanly as possible. The detection must be state-selective as well in the case of two state atom interferometers. There are several types of detection available for neutral atoms with low energies: fluorescence, absorption, and dispersion detection. These detection methods are described briefly here and are discussed in depth in section 5.7.

Fluorescent detection is the easiest detection scheme to implement. The atoms are illuminated with light that is resonant or nearly-resonant to an optical transition. The photons spontaneously emitted from the atoms are detected on some imaging device, such as a photodiode, photo-multiplier tube, or a charge-coupled device camera. If the light is tuned to a closed transition, *i.e.* the cooling transition for an atom in the  $F = 4$  state, then the atom will scatter many photons before the atom optically pumps to a dark state via off-resonant excitations (the  $F = 3$  state here). Under typical experimental conditions for Cs atoms in the  $F = 4$  state, using light tuned to the cooling transition at  $I = I_{\text{sat}}$ , about 1000 photons will be scattered from each atom before it pumps into the  $F = 3$  state and goes dark to the detection light. Atoms in the  $F = 3$  state usually must be first pumped into the  $F = 4$  state with a repumper before detection, as there is no closed transition from the  $F = 3$  manifold.

Fluorescent detection scatters light into a solid angle of  $4\pi$  steradian. If the

solid angle that the detector (or the collection lens before the detector) subtends is significantly smaller than this, then very few photons per atom will be detected. These smaller signal levels can lead to problems with counting statistics and can be limited by technical noise as well. To overcome this solid angle problem, which is often limited by the fundamental geometry of the experiment, absorption detection may be used. The principle of absorption detection is similar to fluorescence detection, except that the intensity of the scattering beam is detected with a photodiode, and the photons not scattered by the atoms are detected. In this way, essentially all the scattered photons are detected (or more precisely the absence of the photons is detected), and the detection statistics are improved, provided the shot noise from the unabsorbed portion of the light is not too large.

The final detection method employed with ultra-cold atoms is a dispersive measurement. This is similar to absorption except the complex part of the atoms' index of refraction is measured here, whereas absorption measures the real part. The dispersion of an off-resonant detection beam as it passes through the atoms is measured by heterodyning it with a local oscillator. This method is primarily useful for dense clouds of atoms with large refractive indices, such as BECs. For the relatively diffuse clouds produced by atoms at MOT temperatures at low densities following atomic fountains, this method produces small signals and is not suitable.

### 3.9 Experiment synopsis

Having described some of the basic tools of atom optics, it is now possible to describe the gravity gradiometer experiment in more detail. First Cs atoms are cooled and trapped from a thermal vapor at two spatially separated regions in two MOTs. Each ensemble of cold atoms is then launched in an atomic fountain in a specially prepared hyperfine state. During the fountain, the atoms are interrogated with a three pulse  $\pi/2 - \pi - \pi/2$  interferometer sequence consisting of stimulated two-photon Raman transitions. The phase of the atoms following the interferometer is determined by the atoms' interaction with the interferometer laser fields as well as the free evolution of the atom, both of which are influenced by the presence of gravity. Following the

interferometer, the relative populations of the two hyperfine states are read out using a sensitive detection scheme. The difference between the gravitationally induced phases from the two ensembles of atoms is directly proportional to the gravity gradient.

# Chapter 4

## Atom Interferometry

It may seem obvious that the interferometer phase shift of an atom falling in a gravitational field is

$$\phi = \mathbf{k}_{\text{eff}} \cdot \mathbf{g}T^2, \quad (4.1)$$

to first-order. After all, this phase is simply the total distance travelled by the atom experiencing acceleration  $\mathbf{g}$  in time  $T$ ,  $gT^2/2$ , divided by the effective wavelength of the interferometer light used to “measure the distance,”  $1/k_{\text{eff}} = \lambda/2$ . It is not obvious how this is related to an interferometer however. This chapter attempts to explain the interferometer phase shift and to present several different techniques for obtaining precise phase shift calculations. First an intuitive heuristic description is given, followed by a discussion of the total interferometer phase. Each term of the interferometer phase is discussed and calculated. Particular detail is given to the phase shift from the free propagation of the atoms between interferometer pulses. The application of these methods to nonuniform acceleration fields is described. The limits and merits of each case are discussed. The fundamental assumptions made in the starting point for these phase calculations are considered. Finally, the application of these results to gravity gradiometers is discussed.

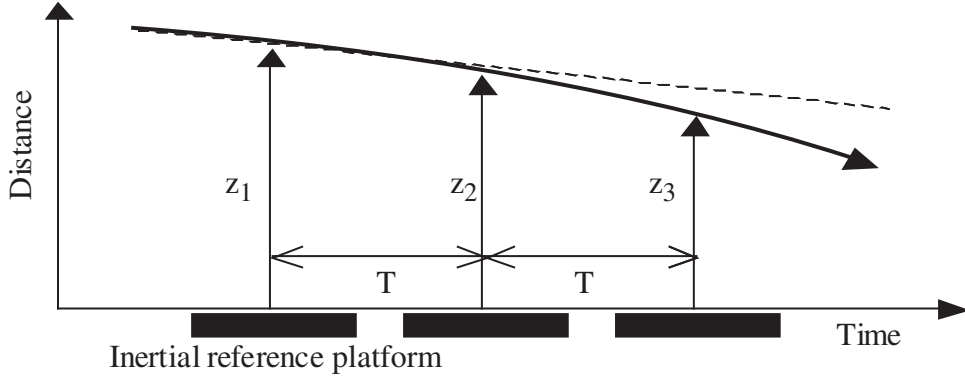


Figure 4.1: Gravity can be measured by measuring the difference between the gravitationally accelerated trajectory (solid line) and the unperturbed trajectory (dotted line) by making three measurements separated by time  $T$  with respect to a reference platform.

## 4.1 Intuitive analogy

The easiest way to understand the first-order results is to consider the following situation. Imagine one makes position measurements of a falling object, a mirror for instance, by reflecting a laser pulse off of it and timing the return at three equally spaced times. The mirror's average velocity can be calculated with two position measurements, and a third measurement can determine the change in velocity, *i.e.* the acceleration (see Fig. 4.1). The average acceleration experienced by the atom is given by

$$a = \frac{(z_1 - 2z_2 + z_3)}{T^2}. \quad (4.2)$$

Now consider the laser pulse itself as the measurement “ruler.” Because of its small wavelength, the laser makes a very fine “ruler.” The phase of the laser at the position of the atom is  $\phi_i = k_{\text{eff}} z_i$ . The relevant wavevector here is  $k_{\text{eff}} = k_1 - k_2$  because each interferometer pulse is a two-photon transition. Substituting into equation 4.2 and rearranging gives

$$\Delta\phi = k_{\text{eff}} g T^2. \quad (4.3)$$

This result is the correct result for an atom in free-fall, to first-order in the perturbation by gravity. The addition of gravity gradients, rotations, and the wave nature of

the atom complicates the situation. This gravitational phase shift is around  $10^6$  rad for typical experimental parameters in the presence of Earth's gravity. The goal of gradiometry is to detect differences that are typically  $10^{-8}g$  (0.01 rad) or much less between two such gravimeters.

## 4.2 Interferometer description

The interferometer is formed by three pulses, each driving a velocity-sensitive, two-photon, stimulated Raman transition between two long-lived hyperfine ground states [14]. The pulse sequence is a  $\pi/2 - \pi - \pi/2$  pulse sequence and is a modification of the Ramsey separated oscillatory field sequence<sup>1</sup>  $\pi/2 - \pi/2$  [8]. With the atom initially in the ground state  $|g\rangle$  the first  $\pi/2$  pulse puts the atom in a coherent superposition between the ground and excited states. This pulse acts as a beamsplitter by transferring momentum  $\hbar\mathbf{k}_{\text{eff}}$  to the wavepacket that makes the transition to the excited state. In this interferometer there is a one-to-one correlation between internal states and momentum states of the atom. The two wavepackets propagate freely, only influenced by inertial forces, while drifting apart with relative momentum  $\hbar\mathbf{k}_{\text{eff}}$ . At a time  $T$  later, the second pulse, a  $\pi$  pulse, is applied. This pulse interchanges the ground and excited states, while reversing their relative momenta. The two wavepackets then drift back towards each other for time  $T$ . Finally, at time  $2T$  after the first  $\pi/2$  pulse, the final  $\pi/2$  pulse recombines the two wavepackets, interfering them. This sequence is depicted in a recoil diagram in Fig. 4.2. During each pulse, the phase of the optical field at the position of the atoms is imprinted on the internal state probability amplitude of the atoms, as described in section 3.7. The probability of finding the atom in a particular state following the interferometer depends on the relative phase accrued by the two interfering wavepackets during the interferometer, and this phase depends on the inertial forces experienced by the atom [16].

---

<sup>1</sup>The modification is necessary because the Raman sequence transfers non-negligible momentum to the atom, and the extra  $\pi$  pulse ensures the two wavepackets overlap at the end of the interferometer.



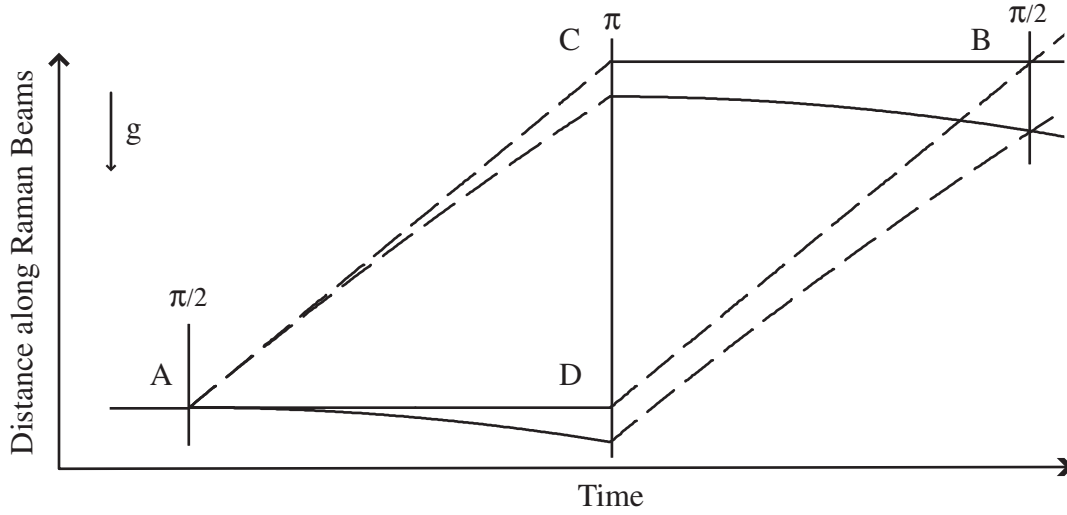


Figure 4.2: Recoil diagram of the interferometer sequence. Solid and dotted lines represent the  $F = 3$  and  $F = 4$  states respectively. The Raman interferometer pulses are denoted by the vertical lines at the appropriate times. In the absence of perturbing forces, the paths are straight and the loop is a parallelogram. In the presence of gravity, the paths sag. Points are label A, B, C, and D for reference.

If there is no acceleration present, the atoms follow straight paths, and the interferometer loop is a perfect parallelogram. In the presence of a uniform gravitational field however, the trajectories are deflected. The interferometer is no longer a parallelogram, but it is still a closed loop, deformed by the gravitational sag, as seen in Fig. 4.2. The addition of a gravity gradient further distorts the symmetry. Now the paths taken by the two wavepackets in the interferometer no longer meet. However, due to the finite spread of the atomic wavepackets, there is still overlap, and interference can still occur. Note that the actual physical area enclosed in the interferometer is zero; there is only enclosed area in recoil diagram space. The presence of unwanted rotations<sup>2</sup> and transverse velocities can complicate the situation further by causing the interferometer to enclose a physical area and to acquire an additional phase shift from the Sagnac effect [64].

Following the approach given in [65], the full interferometer phase shift is a sum

<sup>2</sup>The component of the centrifugal force parallel to gravity is usually included in  $g$ . This component is about 0.3% of  $g$ .

of three terms:

$$\phi_{\text{tot}} = \phi_{\text{prop}} + \phi_{\text{laser}} + \phi_{\text{diff}}. \quad (4.4)$$

The first term is the phase difference between the two interferometer arms acquired during the free propagation between laser pulses. The interactions with the Raman beams gives an additional shift,  $\phi_{\text{laser}}$ . The final term is a contribution that arises from non-ideal overlap in the two interfering wavepackets at the end of the interferometer, as in the presence of gravity gradients. Each of these terms is dependent on the inertial forces present in the interferometer and will be described in more detail in the following sections. The probability of the atom to be in state  $|4\rangle$  following the interferometer if it began in state  $|3\rangle$  is  $P_4 = \frac{1}{2} [1 - \cos(\phi_{\text{tot}})]$ . By measuring this probability, the phase shift accrued by the atom in the interferometer is measured, and an inertial force measurement can be extracted. Depending on the method of calculating the phase, the largest contribution to the gravitational phase appears to come from the laser interaction or the free propagation.

### 4.3 Wavepacket overlap phase

The final term in equation 4.4 is the easiest to understand. If the two interfering wavepackets do not perfectly overlap, then a phase shift will arise. In Fig. 4.3 an expanded view of the interference region is depicted. In the situation depicted, the two interfering paths are separated by  $z_{\text{diff}}$  and do not actually meet. However, because of the spatial extent of the atomic wavepackets, interference can still occur. It is easiest to calculate this term if the interfering states are assumed to be plane waves. The validity of this assumption is discussed in section 4.7. In this situation the phase of the wavefunction from the lower path at the position where it intersects the classical trajectory of the upper path is simply  $k_{\text{lower}} z_{\text{diff}}$ , where  $k_{\text{lower}} = mv_{\text{lower}}/\hbar$ . This term is zero in the presence of only a uniform acceleration, as the two interfering paths meet at one point.

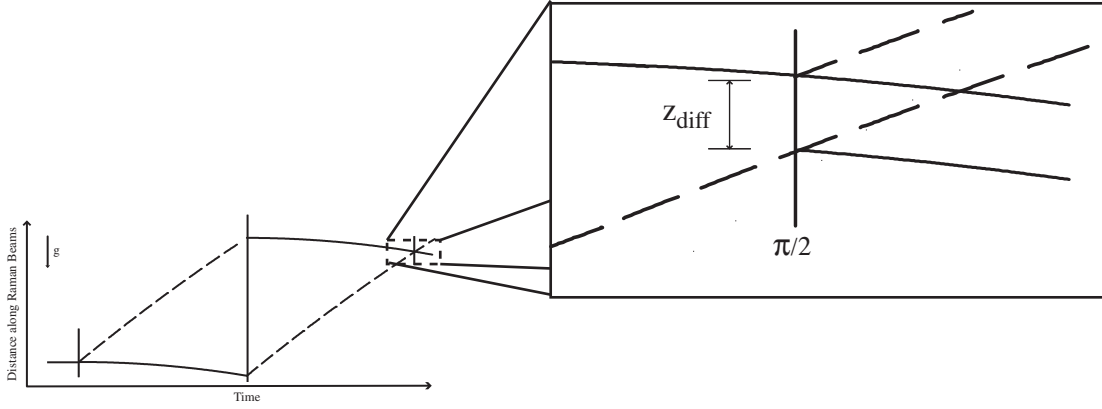


Figure 4.3: Recoil diagram showing the mismatch in paths  $z_{\text{diff}}$  after the interferometer in the presence of gravity gradients. Interference can still occur if  $z_{\text{diff}}$  is less than the coherence length of the atomic wavepacket.

## 4.4 Laser phase

The contribution to the total phase in equation 4.4 from the laser-atom interactions  $\phi_{\text{laser}}$  can be calculated from the rules for two-photon Raman transitions presented in section 3.7. The total laser phase is the laser phase imparted to the top path minus the phase imparted to the lower path. Assuming the atom initially starts in state  $|3\rangle$ , following the transition rules given in Eqs. 3.21 and 3.22 this phase is:

$$\phi_{\text{laser}} = \phi_1 - 2\phi_2 + \phi_3. \quad (4.5)$$

The phases  $\phi_i$  are the phases imprinted on the atom by the  $i^{\text{th}}$  Raman pulses. For an atom following a classical path in a uniform gravity field, each phase at time  $t_i$  and atomic center of mass position  $x_i$  is:

$$\phi_i = \omega_i t_i - \mathbf{k}_{\text{eff}} \cdot \mathbf{x}_i + \phi_i^\circ = \omega_i t_i - \frac{1}{2} k_{\text{eff}} g t_i^2 + \phi_i^\circ. \quad (4.6)$$

Here the trajectories and Raman beams are assumed to be parallel with  $\mathbf{g}$ ,  $\omega_i$  is the frequency of the Raman lasers at the time of the  $i^{\text{th}}$  pulse, and  $\phi_i^\circ$  is the arbitrary

phase of the laser. Recall that  $\mathbf{k}_{\text{eff}} = \mathbf{k}_1 - \mathbf{k}_2 \simeq 2\mathbf{k}_1$ . Only the case of

$$\begin{aligned} t_1 &= 0 \\ t_2 &= T \\ t_3 &= 2T \end{aligned} \tag{4.7}$$

is considered, *i.e.* an interferometer with pulses spaced equally by time  $T$ .

#### 4.4.1 Frequency term

For a constant frequency  $\omega$  the frequency terms in equation 4.6 cancel and equation 4.5 reduces to

$$\phi_{\text{laser}} = k_{\text{eff}}gT^2 + \Delta\phi^\circ, \tag{4.8}$$

where  $\Delta\phi^\circ = \phi_1^\circ - 2\phi_2^\circ + \phi_3^\circ$ . However, for typical experimental interaction times of 100 ms or more, the Doppler shift due to gravity is  $k_{\text{eff}}gT \sim 1$  MHz. This Doppler shift is much larger than the typical two-photon Rabi frequency  $\Omega_{\text{eff}} \sim 30$  kHz. Thus if the laser frequency is kept constant throughout the interferometer, the atoms quickly Doppler shift out of resonance with the beams due to the acceleration of gravity. Typically, to counteract this effect the frequency of the laser is linearly chirped at a rate  $\delta\dot{\omega}$  equal to the gravitational Doppler shift:

$$\omega(t) = \omega_\circ - \delta\dot{\omega}(t - t_1) = \omega_\circ - k_{\text{eff}}g(t - t_1). \tag{4.9}$$

The frequency term then exactly offsets the gravitational phase term in equation 4.6 and  $\phi_{\text{laser}} = \Delta\phi^\circ$ . In other words, the frequency is chirped at exactly the same rate as the atom is accelerating, and the atom sees wavefronts of constant phase in the falling frame. The gravity information is contained in the precise knowledge of the frequency chirp<sup>3</sup>. In theoretical discussions, including the rest of this chapter, this frequency chirp is typically ignored as an experimental detail.

---

<sup>3</sup>For the given transitions in Cs, the chirp rate is 23 MHz/s. Frequency chirps of this rate are routine to generate precisely. Additionally, for a gradient measurement, the frequency chirp is common to both accelerometers and is not an issue.

### 4.4.2 Initial phase

The third term in  $\phi_{\text{laser}}$ , the initial laser phase, is now examined. If the Raman lasers are temporally coherent across the time of the interferometer, then the initial phase for each pulse will be the same, and  $\Delta\phi^\circ = 0$ . The temporal coherence length for a single laser is  $1/\Delta\nu$ , the reciprocal of the linewidth, and is typically  $\sim 1/300$  kHz for a commercial diode laser. However, for a two-photon process, what is important is the temporal coherence of the difference frequency, not the absolute frequency. This difference frequency is locked to a microwave source at the hyperfine frequency which has a sub-Hertz linewidth. This linewidth translates into an effective coherence time of significantly greater than a second, which is the timescale for the interferometer pulses. If all frequency synthesizers used to generate the Raman pulses have typical coherences and the pulses themselves are generated in a phase-continuous way, *i.e.* as from a continuously chirped sine wave, then the initial laser phase contribution will be zero still. In this situation, and in the absence of gravity gradients or rotations,  $\phi_{\text{diff}}$  and  $\phi_{\text{prop}}$  are zero<sup>4</sup>, and the total laser phase reduces to the naive model given in equation 4.3,  $\phi_{\text{tot}} = k_{\text{eff}}gT^2$ .

However, if the reference platform on which the lasers are held is moving with respect to the freely falling atoms, then  $\Delta\phi^\circ$  can be nonzero. If the reference platform is moving with velocity  $v_o$  and acceleration<sup>5</sup>  $a$ , then the phase for each pulse is  $\phi_i = k(v_o + at_i)t_i$ . The constant velocity term cancels, but the acceleration remains. This is a manifestation of the equivalence principle. It is not possible to distinguish the acceleration of the reference platform from gravitational acceleration using a local measurement. Shot-to-shot variations in the platform acceleration appear in the measurement as phase noise on the interferometer phase. For this reason, gravimetry requires an ultra-stable reference platform. Gradiometry relaxes this constraint, as discussed in section 4.8.

---

<sup>4</sup> $\phi_{\text{prop}} = 0$  in the full, non-perturbative calculation for this case.

<sup>5</sup>If the acceleration of the reference platform is not constant over the interferometer, then the acceleration must be integrated to find the position of the platform at each time  $t_i$ .

## 4.5 Free propagation phase

### 4.5.1 Path integral formalism

Feynman path integrals are powerful tools for calculating the inertial force-induced phase shifts due to the free propagation of the atoms in between the laser pulses, called  $\phi_{\text{prop}}$  in equation 4.4. This approach was first applied by Kasevich and Chu [16] and further elucidated by Storey and Cohen-Tannoudji [65], and the results will be summarized here. The path integral approach is used to calculate the phase shift a particle accrues moving from point A to a point B. The path integral integrates the phase over all possible paths to determine the total shift. However, only the phases for the paths near the classical path contribute, because the phases from all other paths oscillate rapidly and destructively interfere. This fact has the appealing result that the propagation phase may be calculated using only the classical paths.

First a brief review of the classical path integral method is given. A more complete description is given in a number of references [66, 67]. The classical path integral approach is used to calculate the path that a particle takes travelling from point A to point B. There are an infinite number of paths the particle can take, but the Lagrangian of the system determines uniquely the one path the particle actually takes. The Lagrangian of a particle of mass  $m$  at position  $z$  in a potential  $V(z)$  is

$$L(z, \dot{z}) = \frac{1}{2}m\dot{z}^2 - V(z). \quad (4.10)$$

The action  $S$ , defined as the integral of the Lagrangian along a path  $z(t)$  between points A and B, is extremal for the actual path taken in the classical case. The action over the time at the two endpoints  $t_A$  and  $t_B$  is written

$$S_{AB} = \int_{t_A}^{t_B} L(z(t), \dot{z}(t)) dt. \quad (4.11)$$

The action  $S_{AB}$  is extremal for the classical path taken by the particle between the two endpoints, and the Euler-Lagrange Equations can be solved to obtain the classical equations of motion.

In the Feynman formulation [68, 69], the quantum propagator  $K_{AB}$  is used to describe the evolution of a quantum mechanical system from point A to point B over times  $t_A$  and  $t_B$ . Similar to classical Lagrangian mechanics, the propagator is a sum of the contributions from all paths connecting the two points. Along each possible path, the amplitudes of the components of the wavefunction are the same, but the phases for each path differ. Thus the propagator is given by

$$K_{AB} = N \sum_{\mathcal{P}} e^{\frac{iS_{AB}^{\mathcal{P}}}{\hbar}}, \quad (4.12)$$

where the sum is over the set of all possible paths  $\mathcal{P}$  and  $N$  is a normalizing constant. Far from the classical path, the action is much larger than  $\hbar$ , the phase oscillates rapidly, and these paths destructively interfere. Thus only paths close to the classical path contribute to the sum. The wavefunction at point B simply can be written as

$$|\Psi(t_A, z_B)\rangle \sim e^{\frac{iS_{AB}^{\mathcal{P}}}{\hbar}} |\Psi(t_A, z_A)\rangle. \quad (4.13)$$

This result means that the propagation phase can be obtained by considering the classical trajectories of the atomic center of mass wavepackets and integrating the Lagrangian along these trajectories. One of the key approximations in this approach is that the atomic wavefunctions are plane waves. The validity of this assumption will be discussed in section 4.7.

For an atom in an interferometer in the presence of a uniform gravity field with no gradients or rotations, the Lagrangian is:

$$L = \frac{1}{2}mv^2 - mgz. \quad (4.14)$$

In the exact treatment, this Lagrangian is evaluated along the classical paths shown in Fig. 4.2, where the paths are curved due to gravitational sag. The propagation phase is:

$$\phi_{\text{prop}} = \phi_{\text{prop}}^{\text{AC}} + \phi_{\text{prop}}^{\text{CB}} - \phi_{\text{prop}}^{\text{AD}} - \phi_{\text{prop}}^{\text{DB}}, \quad (4.15)$$

where the terms on the righthand side of the equation are the propagation phases

along each segment of the interferometer. However, this sum is equal to zero, which is to be expected from the symmetry of the interferometer. This is the situation described in section 4.4.2, and all the gravitational phase is contributed by the laser interaction in this description.

### 4.5.2 Perturbative approach

If one is only interested in finding the contribution of a small addition to the Lagrangian, for instance from rotations, gravity, or gravity gradients, then a perturbative approach can be taken. This approach is complementary to the exact approach given in the previous section. The extra force or potential may be considered as a perturbation  $L_1$  to the Lagrangian:

$$L = L_0 + L_1 \quad (4.16)$$

In this approach, the phase shift  $\phi_{\text{prop}}$  is obtained by integrating the perturbed Lagrangian over the unperturbed path:

$$\phi_{\text{prop}} = \frac{1}{\hbar} \int_{\Gamma_0} L_1 dt. \quad (4.17)$$

The integral is a path integral over the unperturbed path  $\Gamma_0$  representing the interferometer loop.

As an example, consider gravity as a perturbation to an atom moving with constant velocity in an interferometer. In this case:

$$L_0 = \frac{1}{2}mv^2 \quad (4.18)$$

$$L_1 = mgz. \quad (4.19)$$

Integrating the perturbation Lagrangian  $L_1$  over the straight, unperturbed classical paths gives  $\phi_{\text{prop}} = k_{\text{eff}}gT^2$ . In this picture,  $\phi_{\text{laser}} = \Delta\phi^\circ$  over the unperturbed straight paths, and  $\phi_{\text{diff}}$  still is zero because the two interfering wavepackets overlap perfectly. So in the perturbative approximation,  $\phi_{\text{tot}} = k_{\text{eff}}gT^2 + \Delta\phi^\circ$  exactly as in the exact



analytical treatment of section 4.4.2. These two methods are equivalent in the case of no gravity gradients or rotations.

## 4.6 Nonuniform acceleration fields

### 4.6.1 Exact solution

Even in the most complicated acceleration fields, for a given set of physical parameters it is not difficult to obtain the exact solution for the interferometer phase shift. Of course, this solution is only “exact” within certain fundamental assumptions discussed in section 4.7. The exact solution typically can only be obtained numerically. The full acceleration experienced by the atom is numerically integrated to obtain the exact equations of motion. The equations of motion are then used to calculate numerically the propagation phase shifts, laser interaction phase shifts, and wave packet difference phase shifts. In this manner, the exact phase shift can be numerically obtained. This is not a demanding calculation for modern computers and gives the accurate results for known physical parameters.

However it is desirable to have an analytic expression for the total phase shift. In complicated situations with rotations and gravity gradients, it is beneficial to be able to isolate certain terms. This is especially true when attempting to measure extremely small accelerations ( $10^{-15}$  g for instance). An analytic solution is useful for studying the phase noise induced by certain types of noise components (*e.g.* rotations or initial velocity fluctuations). Perhaps by varying certain experimental parameters such as interaction time and launch velocity, some terms can be measured independently of others. Also, it may be possible to measure other forces such as other components of the gravity gradient tensor or rotations by using an analytic expression with an ultra-precise gravity gradiometer. Finally, analytic expressions are sometimes faster than numerical models to compute and could be significant for analysis of large data sets.

### 4.6.2 Gravity gradients

The addition of gravity gradients to the constant gravity field complicates the calculations. In this case, none of the terms of equation 4.4 are zero in any of the approaches. Gravity gradients add a correction to the interferometer phase shifts of about a part in  $10^{-8}g$ , or around 0.01 rad for typical experimental parameters. The primary influence of gravity gradients is to break the symmetry of the interferometer. The upper and lower paths sag by different amounts now (see Fig. 4.3). In this case the total Lagrangian in the presence of a linear gravity gradient  $\alpha$  added on to a uniform gravity field  $g_o$  is:

$$L(z, v) = \frac{1}{2}mv^2 - mg_o z + \frac{1}{2}m\alpha z^2, \quad (4.20)$$

where  $\alpha$  is assumed to be positive (*i.e.* gravity decreases with increasing altitude). Near the Earth's surface, gravity falls off approximately inversely proportional to altitude, at a rate of  $\sim 1.5 \times 10^{-7}g/m$ , and a linear gradient is a good assumption, especially over the short span of an atomic fountain. This effect is a small effect that is amenable to the perturbative approach.

It is not surprising that, when using the perturbative approximation, the wrong answer is reached if both the homogeneous gravitational acceleration as well as gravity gradients are considered in the perturbed Lagrangian, *i.e.* the first two terms of the expansion of the gravitational potential. These two terms differ by seven orders of magnitude, and the wrong result for the gradient term is produced. The more correct approach is to consider gravity part of the unperturbed Lagrangian:

$$L_0(z, v) = \frac{1}{2}mv^2 - mg_o z \quad (4.21)$$

$$L_1(z) = \frac{1}{2}m\alpha z^2. \quad (4.22)$$

The  $\phi_{\text{laser}}$  is taken over the unperturbed path, including the uniform gravity component  $g_o$ , and is equal to the results of section 4.4. The propagation component of the phase is determined by integrating the perturbed Lagrangian  $L_1$  over the unperturbed path, where the parabolic unperturbed paths include the effect of gravity, but not

that of the gravity gradient. Performing this integral gives:

$$\phi_{\text{prop}} = \alpha k_{\text{eff}} T^2 \left( \frac{7}{12} g_{\circ} T^2 - v_{\circ} T - z_{\circ} \right). \quad (4.23)$$

In this situation, the two interfering wavepackets do not overlap perfectly at the time of the final  $\pi/2$  pulse, as seen in Fig. 4.3. This wavepacket separation gives an extra phase shift, and the total phase shift, to first order in  $\alpha$  becomes:

$$\phi_{\text{tot}} = k_{\text{eff}} g_{\circ} T^2 + \alpha k_{\text{eff}} T^2 \left( \frac{7}{12} g_{\circ} T^2 - v_{\circ} T - z_{\circ} - \frac{\hbar^2}{2m} T \right). \quad (4.24)$$

In this equation, the acceleration experienced by the two wavepackets was integrated over the two paths in order to determine their final separation and obtain  $\phi_{\text{diff}}$ . This case of gravity plus a linear gravity gradient can be solved analytically. Taylor expanding the analytic solution to first order in  $\alpha$  yields the same expression as equation 4.24. The perturbative approach works well for this case, giving good agreement with the analytic solution; it is only in the presence of rotations as well that the perturbative result begins to have difficulties.

### 4.6.3 Rotations

The presence of rotations vastly complicates the phase shift calculations. Rotations deflect the trajectory of the wavepackets from the vertical and convert a one-dimensional problem into a two- or three-dimensional problem. If the interferometer encloses any physical area, as opposed to only enclosing area in the recoil diagram-space, then a Sagnac phase shift due to the Coriolis acceleration will be included in the interferometer phase shift [70]. Additionally, centrifugal forces contribute phase shifts to the atoms in the presence of rotations. These phase shift are calculated similarly to the above gravitational phase shift, and the resulting phase shift for a rotation  $\mathbf{\Omega}$  is:

$$\phi_{\text{rot}} = 2\mathbf{k}_{\text{eff}} \cdot (\mathbf{v} \times \mathbf{\Omega}) T^2 + \mathbf{k}_{\text{eff}} \cdot (\mathbf{\Omega} \times (\mathbf{\Omega} \times \mathbf{r})) T^2. \quad (4.25)$$

The first term is the Coriolis term, while the second is due to centrifugal acceleration. Typically a perturbative approximation is used to calculate the influence of rotations on the interferometer phase for a gravimeter or gradiometer, as the rotation phase shifts are generally small in these configurations. The relative magnitudes of the two rotation terms depends on the exact interferometer geometry, particularly the alignment of the atomic fountain.

In the pursuit of the high precision measurements needed to test General Relativity and seek new forces as described in section 2.3, the accuracy of the analytic results of the perturbative method was examined. Several attempts have been made to examine the higher order corrections [22, 71], but they fall short at around  $10^{-10}g$ . Several colleagues performed a series of calculations designed to test the perturbative result to higher orders using a Taylor expansion approach [72]. The approach was as follows: in the rotating frame, *i.e.* the lab frame, the equations of motion were solved analytically using only uniform gravity and rotations. The perturbative path integral approach was then used to calculate the free propagation phase shift by integrating the Lagrangian, including gravity gradients, over the equations of motion. This path integral was carried out by Taylor expanding the Lagrangian and integrating over the Taylor expanded equations of motion. This approach results in an analytic solution, albeit a complicated one, that agrees with the exact numerical calculations to a part per  $10^{16}$  when the expansion is carried out to seventh order. This level is better than even the anticipated performance for a space-based gradiometer (see section 8.2). In this approach, higher order curvature is neglected, which contributes at about the level of the last digit (which is where the second order gradient correction enters).

## 4.7 Limitations to the theory

The numerical solutions labelled as “exact” here are only accurate within the framework of the approximations made in the theory. There are several fundamental assumptions to the theory presented here, particularly to the path integral approach of finding the free propagation phase, which bear a closer look. These approximations are certainly sufficient for almost all practical gradient sensing applications, which

usually require precision no better than  $10^{-10}g$ . However for the ultra-precise tests of General Relativity and searches for new physics discussed in section 2.3, some of the approximations may not be sufficient.

One of the fundamental approximations to the path integral method is to approximate the Gaussian atomic wavepackets as plane waves. To some degree it seems like a very poor approximation to do this, and it is surprising that the method works as well as it does. The reason for the success of the approximation is that the atomic wavepackets are essentially plane waves within a Gaussian envelope. In fact, the atomic wavepackets produced by the MOT are near Heisenberg-limited wavepackets. Initially the MOT localizes the atom to  $< \lambda/2$  and a temperature around  $1\mu\text{K}$ , which produces a wavepacket near the Heisenberg limit<sup>6</sup>. To determine fully the phase shifts for Gaussian wavepackets, the approach is to integrate numerically the entire wavepacket using the path integral method. Spreading of the Gaussian wavepacket must be considered, as well as distortion to the presence of gravity gradients. This is a difficult proposition and is only potentially a concern for precisions of the order of  $< 10^{-15}g$ .

In some gravitational fields the Lagrangian is not quadratic. Again, in this case, the path integral approach will break down. This is not due to a limitation in the theory of Storey and Cohen-Tannoudji, but rather in that of Feynman's original path integral theory. Feynman only proved the path integral approach to quantum mechanics for quadratic Lagrangians [68]. It is conceivable that for complicated gravitational potentials, the limit of only integrating along the classical path is not valid. The problem might become a true "quantum problem" requiring integration over a large number of non-classical paths. In this case, a direct numerical integration of the Schrödinger equation is called for. It is unlikely any analytic solution exists for this regime. Such a breakdown in the theory is only conceivable in the near-field limit of large test masses close to the proof masses. In the far field limit, the gravitational contribution to the Lagrangian is always quadratic (assuming a reference frame that is at most slowly rotating).

---

<sup>6</sup>The full description of atoms in a MOT is a complicated proposition requiring solving the Fokker-Planck equation, but the approximation of Heisenberg-limited Gaussian wavepackets is a reasonable one.

Another approximation in the theory lies in the laser-atom interactions. In section 3.7 the theory of stimulated Raman transitions was described using the short, intense pulse limit. The length of the Raman pulses was neglected since it is typically four orders of magnitude shorter than the interferometer interrogation time. For ultra-precise measurements, it is certainly called for to integrate the phase over the envelope of the Raman pulses. Even more than this effect, the fundamental process of the Raman transition needs to be studied. Questions regarding what happens during the Raman transition need elucidating. During the transition itself, the atom certainly behaves non-classically, and there is not a single point where momentum is instantaneously imparted to the wavepackets. Such questions merit full integration of the Schrödinger Equation.

## 4.8 Application to gradiometry

So far, the theory has been described only for single interferometer gravimeters. By taking two spatially-separated interferometers and directly subtracting the interferometer phases, a phase proportional to the gravity gradient is obtained<sup>7</sup>. Explicitly, the gradiometer phase shift is the difference of the total interferometer phase shifts for the two gravimeters:

$$\Delta\phi = \phi_{\text{tot}}^{(1)} - \phi_{\text{tot}}^{(2)}, \quad (4.26)$$

where 1 and 2 represent the two gravimeters. In the case of a linear gravity gradient on top of a uniform gravity field with no rotations, this phase reduces to:

$$\Delta\phi = k_{\text{eff}}T^2\alpha \left( z_{\text{o}}^{(1)} - z_{\text{o}}^{(2)} \right) + \left( \Delta\phi_{(1)}^{\text{o}} - \Delta\phi_{(2)}^{\text{o}} \right), \quad (4.27)$$

where  $z_{\text{o}}^{(1)}$  and  $z_{\text{o}}^{(2)}$  are the initial positions of the two atom ensembles. This solution is obtained considering the gravity gradient in each interferometer in the perturbative limit. Note that  $\phi_{\text{diff}}$  drops out as it depends only on the gravity gradient at each interferometer, and that gradient is assumed to be linear and constant here. Additionally, the large first order gravity shift cancels as expected. The first term of

---

<sup>7</sup>This phase is modulo  $2\pi$  but is typically less than  $2\pi$  for most of the gravity gradients involved.

equation 4.27 is just the difference in gravity between the initial positions of the two accelerometers and is usually written as  $k_{\text{eff}}\delta g T^2$ .

The key virtue of gradiometers is manifested in the second term of equation 4.27. As described in section 4.4.2, this term contains the acceleration noise induced by vibrations of the reference platform (the optical table containing the Raman lasers) which plagues gravimeters. However, because the same reference platform is used and the same lasers simultaneously drive the two interferometers  $\Delta\phi_{(1)}^\circ - \Delta\phi_{(2)}^\circ = 0$ . In the instance of perfect common-mode coupling of the two gravimeters, the gradiometer is completely immune to reference platform noise. It is this immunity to vibrational noise that makes gravity gradiometers the instruments of choice for mobile studies of gravity and studies requiring extremely high precision.

Another important benefit of gradiometers is that several of the higher order effects discussed in the previous section have a high degree of commonality between the two gravimeters<sup>8</sup>, which lessens the constraints on the rigor of the calculations. For instance, the second order curvature of the Earth's field is only  $\sim 10^{-6} T_{zz}$  over 1 m, and can be safely neglected if the measurement baseline is not too large and the required instrument accuracy is less than this level. Other effects, such as changing gravity due to tides, *i.e.* changing gravitational attraction due to the position of the Sun and the moon, contribute to a gravimeter at  $10^{-7}g$ , but to a 10 m gradiometer at  $10^{-12}g$ , and again this effect can be neglected for most applications.

Of final note is that the accuracy of the gravity gradiometer is limited by the accuracy to which the separation between the two accelerometers is known. The uncertainty of the spacing leads to an uncertainty in the gradient in a linear fashion. However for the purposes of the measurements contained herein, video imaging of the position of the atom ensembles is sufficient to locate them within the chambers to around 0.1 mm, and the spacing between the chambers is measured to similar accuracy. This is an uncertainty of approximately one part in  $10^4$ , which is sufficient for this dissertation.

---

<sup>8</sup>This is particularly true for far-field mass distributions and not necessarily the case for complex gravity fields typical of near-field masses.

# Chapter 5

## Experimental Apparatus

### 5.1 Apparatus overview

The apparatus consists of two laser cooled and trapped sources of Cs atoms in two separate ultra-high vacuum (UHV) chambers. The atoms are launched on ballistic trajectories and prepared in a particular internal state with optical and microwave techniques before undergoing the interferometer sequence. Following the interferometer sequence, atoms are detected using a normalizing detection method. The total cycle time is 0.7 - 1.4 s, depending on the trap loading parameters. Each of these stages is described below. In addition, the operation of an actively controlled vibration isolation system which is used to validate the data acquisition methodology is described. Finally, the subsystem for generating microwaves is described. A picture of the gravity gradiometer apparatus is shown in Fig. 5.1.

### 5.2 Vacuum system

#### 5.2.1 Motivation for vacuum

Laser cooling and trapping experiments need to be performed in a region of UHV. There are two main considerations that determine what level of vacuum is necessary: loading of the MOT and coherence in the interferometer. The MOT is loaded from



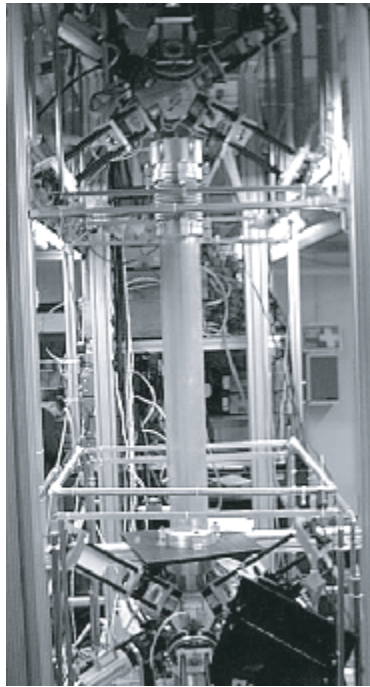


Figure 5.1: Picture of the gravity gradiometer apparatus showing the two separate vacuum chambers and the tube through which the Raman beams propagate in between the chambers. The black rods coming off of each vacuum chamber define the axes on which the trapping beams are coupled to the chamber.

a thermal vapor, and from Eq. 3.15, if the background pressure is significantly less than the Cs vapor pressure, the steady-state number of atoms trapped is independent of the vapor. However, the loading rate still increases with vapor pressure. At about  $10^{-7}$  torr, MOT formation is not possible due to background collisions hindering the cooling process.

The second criterion is that during the trajectories of the laser cooled atoms in the interferometer, the atoms must be free from collisions with the background gas. While the atom is in a coherent superposition of hyperfine states in the interferometer, the most likely result of a collision by a atom from the background is that enough momentum will be transferred to the atom so that it will be lost from the fountain and will not be detected following the interferometer. The more problematic collision result is a collision that changes the atom's internal state, thus randomizing its phase, without knocking it out of the fountain. These inelastic collisions cause a loss in interference fringe contrast and decrease the maximum obtainable signal-to-noise ratio (SNR). The collision frequency for air at  $20^\circ\text{C}$  is  $4 \times 10^{14}\text{ cm}^{-2}\text{s}^{-1}$  at  $10^{-9}$  torr [73], which corresponds to a collision frequency of  $\sim 10^{-3}\text{ s}^{-1}$ , or  $\sim 3 \times 10^{-4}$  collision probability per atom during the 320 ms interrogation time. At  $10^{-8}$  torr, the collision probability is 0.3%, which is close to becoming a significant loss in interference fringe contrast. Thus a vacuum of  $\sim 10^{-9}$  torr is needed.

### 5.2.2 Vacuum chamber design and preparation

Having established the need for UHV chambers, the next key issue is the chamber design and construction. Aluminum was chosen for the vacuum chamber because it is nonmagnetic. Even nonmagnetic alloys of stainless steel can have local domains with several mG fields, and these field inhomogeneities could change over time as the steel becomes magnetized by any ambient fields. For this reason aluminum was chosen over steel. Aluminum does have the drawback that it is a good conductor, and it sustains eddy currents for significantly longer than steel, making rapid magnetic field switching difficult. Glass chambers circumvent the magnetic field problems but are hard to anti-reflection coat and are more fragile. Finally, aluminum has an outgassing

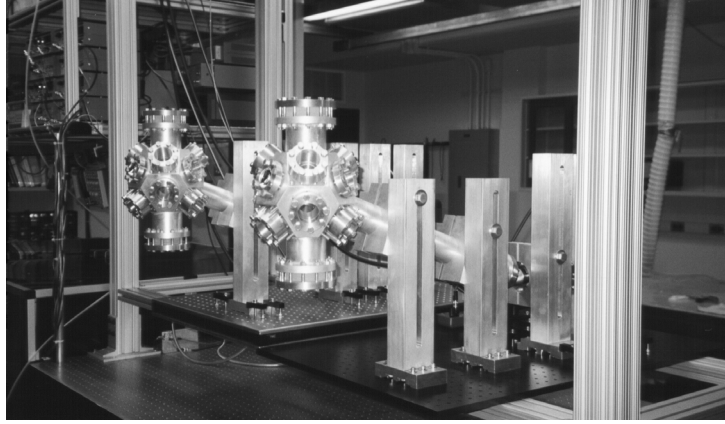


Figure 5.2: Aluminum vacuum chambers used in the apparatus. Trapping beams are injected on six of the smaller side windows, while the large top and bottom flanges are ports for the Raman beams. The picture was taken prior to attaching the auxiliary optics.

rate of  $\sim 20$  times that of steel which limits the base pressure [74].

The central part of each chamber was machined out of a monolithic block of aluminum into a fourteen-sided chamber (see Fig. 5.2). One of the sides is brazed onto a long aluminum tube to be attached to the vacuum pump. The other thirteen sides have through-holes for optical access. Six of the ports are used for the six laser beams which generate the MOT, and five ports are used for detection, state preparation, and observation of the atoms. The final two access holes, on the top and bottom of the chambers, are brazed to short aluminum tubes to accommodate the atomic fountain height. These two ports are both 3 in. diameter holes to allow passage of large interferometer beams, while the other ports are 1.5 in. diameter. The two vacuum chambers are identical.

Prior to assembling the vacuum system, each aluminum chamber was specially prepared in order to achieve the cleanest possible system. After the long pump tube and the two upper and lower tubes, the Raman beam tubes, were brazed on, the aluminum portion of the vacuum chamber was subjected to a chemical cleaning to remove contaminants such as oils, gases, and magnetic particles trapped near the surface of the aluminum that would limit the vacuum or cause stray magnetic fields. The cleaning process first consisted of using a solution of Ardrex, an aluminum

penetrant, for 15 min. at 140° F to remove certain magnetic materials. Next, after a high-pressure rinsing with water, the chamber was soaked in an aluminum pickle for  $\sim 30$  s to further clean the chamber. Following another rinsing, a 3 min. soak in 30% nitric acid removed any remaining surface contaminants. Finally, the chambers were rinsed with several successively more pure baths of high-pressure heated de-ionized water. These steps were necessary to achieve the lowest possible base pressure and obtain the least magnetic chamber possible using aluminum. Finally a coating of Vac-Seal, a commercial UHV sealant, was applied to the outside of each brazed joint in order to seal a few small micro-leaks.

Following the rigorous chamber cleaning, the sealing of the vacuum chamber is accomplished as follows. An anti-reflection coated glass window seals each port by means of an indium seal<sup>1</sup>. Each indium seal consists of a length of 1 mm diameter indium wire formed into a ring slightly smaller than the diameter of the window. The vacuum seal is formed simply by tightening the window down using an aluminum retaining ring placed on top of the window. A mylar spacer ring is placed between the retaining ring and the window to evenly distribute the force applied by the retaining ring in order to keep the window from shattering. The aluminum bolts used to tighten the retaining ring need only be tightened about one quarter turn past finger tight to flatten the indium and make a tight seal. Indium seals can always be tightened further when the vacuum chamber is tested for leaks.

Prior to evacuating the chamber, the Cs reservoir is prepared and attached to the chamber. A glass ampoule containing 5 g of Cs is placed inside a narrow vacuum tube whose inner diameter is barely large enough to accommodate the ampoule. This tube is attached to a glass tube to be used as the temperature controlled reservoir, called the cold finger. This assembly is evacuated with a turbo-molecular pump, baked for several days at  $\sim 200^\circ$  C to remove gases trapped on the walls of the assembly, and then sealed off from the pump. The Cs ampoule is broken by squeezing the narrow tube containing it with a C-clamp until the glass shatters. The tip of the cold finger is cooled to  $\sim -30^\circ$  C and the rest of the chamber is kept heated in order to collect

---

<sup>1</sup>For these windows, the surface quality of each window is only  $\lambda/4$ , as the wavefront distortion of the trapping beams is not as critical as the Raman lasers.

the Cs in the cold finger. After maintaining these temperatures for several days, all the Cs accumulates in the cold finger, and the cold finger is valved-off and attached to the aluminum vacuum chamber on one of the five side ports not used for the MOT laser beams.

### 5.2.3 Chamber evacuation

The chamber is sealed and evacuated with a 25 l/s noble diode ion pump (Varian 9115050) attached to the end of the long aluminum pump tube. The pump tube is long to place the magnet for the ion pump as far as possible from the interferometer region of the chamber. The chamber is first evacuated with a turbo-molecular pump backed by an oil-free diaphragm pump. Then the chamber is heated for one week to degas the chamber walls. The aluminum parts of the chamber are baked at  $\sim 100^\circ \text{C}$  ( $60^\circ$  below the melting point of indium), and the steel portions of the chamber are heated to  $250^\circ \text{C}$ . Following the bake-out, the ion pump is turned on, the chamber is valved-off from the external pumps, and the base pressure falls below  $5 \times 10^{-10}$  torr, using the ion pump current as a pressure gauge. The pressure slowly rises to an equilibrium pressure of  $\sim 9 \times 10^{-10}$  torr due to outgassing of the aluminum chamber. This base pressure is sufficient to not limit the MOT loading or the interferometer fringe contrast.

Finally, the temperature of the Cs cold finger is brought to  $10^\circ \text{C}$ , and the valve to the main chamber is opened. It takes about a day for the Cs partial pressure to build up enough to load a MOT with sufficiently large numbers, because the Cs vapor adsorbs onto the clean chamber walls until a monolayer has built up. The Cs partial pressure is adjusted by either control of the cold finger temperature or by adjusting the valve between the cold finger and the central chamber.

It should be noted that the positioning of the cold finger is critical. If the cold finger is too far away from the central chamber, *i.e.* at the end of the long pump tube near the vacuum pump, it takes a long time (greater than a week) for the pressure in the trapping region to become large enough to form a MOT. This long time is because the entire length of the pump tube must be coated with a monolayer of Cs, and the

bulk of the Cs gets pumped by the ion pump first. Ion pumps are not designed to pump large concentrations of metal vapors like Cs. Therefore, placing the cold finger near the pump will ultimately cause filaments of Cs to form between the anode and cathode of the ion pump, causing a leakage current to flow, giving an erroneous pressure reading and limiting the pump lifetime and speed. Baking the pump again or applying a high voltage of  $\sim 20$  kV to the pump will remove these filaments, but this process cannot be extended indefinitely without shortening the life of the pump. Therefore, the cold finger is placed directly on the vacuum chamber as close to the trapping region and as far away from the ion pump as possible. Additionally, the inside of the pump tube is coated with graphite, which increases the adsorption of Cs because of its large surface area, thereby increasing the lifetime of the pump.

## 5.3 Laser system

The laser system for cooling, trapping, state preparation, and atom detection consists of a frequency stabilized master laser and several power amplifiers. Several configurations based on different types of lasers were used. This section discusses the relative merits of the various laser configurations used and also describes the frequency control and light delivery elements common to all of the laser systems employed<sup>2</sup>.

### 5.3.1 Master laser

In order to obtain a source of cold atoms with minimal fluctuations, the master laser must be frequency stabilized and have a narrow intrinsic linewidth. In the proof-of-principle gradiometer experiment, a distributed Bragg reflector (DBR) laser (SDL 5712) was the master laser. In subsequent experiments an external cavity, grating-stabilized laser (New Focus Vortex) replaced the DBR. The master laser frequency must be near the  $F = 4 \rightarrow F' = 5$ , so the master laser is locked several hundred MHz below this frequency in order to accommodate the frequency shifts necessary for dynamic frequency control.

---

<sup>2</sup>For a detailed description of many of the standard optical elements used in atomic physics experiments see [75, 76] for instance.

The master laser is frequency stabilized to an atomic resonance in Cs vapor using a modulation transfer saturated spectroscopy lock [77]. The lock setup is the same as was used in [70]. A small amount of light ( $\sim 1$  mW) is picked off from the master laser and sent to the locking optics. This beam further is split into two beams: the pump and the probe beams for the saturation lock. The pump beam is double-passed through an 80 MHz acousto-optic modulator (AOM, Isomet 1205C). A Hewlett Packard 8770 arbitrary waveform generator (AWG) generates a radio frequency (rf) frequency modulated (FM) waveform that drives the AOM. The pump beam then propagates through a 3 in. glass cell containing Cs vapor. The probe beam counterpropagates through the Cs cell collinear with the pump beam, and the FM on the pump beam is translated into amplitude modulation (AM) on the probe beam near the narrow atomic resonances. The AM probe is detected on a photodiode (Thorlabs FDS-100) and demodulated using a lock-in amplifier (Stanford Research Systems SRS810). The frequency is actively stabilized to one of the resonances, using proportional, integral, and differential (PID) feedback to the laser controller.

Originally, a DBR laser was the master laser. This laser was locked to the  $4/5$  crossover resonance of the  $F = 4 \rightarrow F' = 5$  transition using an AOM frequency of 72 MHz, with a modulation frequency of 50 kHz and a modulation depth of  $\sim 8$  MHz. The intrinsic linewidth of the DBR was 3 MHz. The DBR was also particularly sensitive to optical feedback. All lasers in the experiment use double-stage optical isolators (Optics for Research IOT-2.7-852-LP) which provide 60 dB of isolation from back reflections. However the small amount of light that is backscattered from the anti-reflection coated front window of the isolator is enough feedback to create a cavity and perturb the DBR frequency. For this reason the isolator is slightly misaligned, and an aluminum tie-rod is attached to the isolator and the laser mount in order to stabilize the length of the cavity formed by backscattering and to minimize changes in the frequency shifts from feedback.

In work subsequent to the proof-of-principle work, a Vortex grating stabilized laser replaced the DBR as the master laser. Because of its extended cavity, the Vortex has a linewidth of 300 kHz, ten times narrower than that of the DBR. The Vortex laser is located in the neighboring lab and is locked to the same Cs resonance as the DBR

was. The locked laser has a stability of  $1 \text{ kHz}/\sqrt{\text{Hz}}$ . Light from the Vortex laser is coupled into a 20 m polarization maintaining (PM) optical fiber and delivered to the gradiometer lab. This light then injection locks the DBR laser at an identical frequency as when the DBR was independently locked [78]. The injection-locked DBR takes on the spectral properties of the Vortex laser which seeds it, thereby reducing its linewidth significantly [79]. The more stable master laser reduces the shot-to-shot rms number fluctuations of the MOTs by a factor of five to a SNR of 200:1. In addition, frequency induced noise during the detection of the atoms following the interferometer is greatly reduced.

### 5.3.2 Laser amplifiers

The MOTs require higher laser powers than the master provides, necessitating the use of amplifier lasers to generate sufficient power for cooling and trapping. The amplifier lasers are all injection locked with the master laser in a master oscillator-power amplifier configuration. The injection locks transfer the frequency stability of the master laser, without addition of extra frequency or intensity noise [79]. Before injecting the slave lasers, the master laser is split in two, and each half is sent through a double-passed AOM. These AOMs are the principal frequency-control AOMs for the trapping and detection beams, and they allow differential frequency control for the two amplifier lasers, one for the upward-pointing set of trapping beams and one for the downward-pointing set of trapping beams. Additionally, two different types of amplifiers were used, tapered amplifiers and standard single-mode amplifier diodes, and their relative merits are discussed here.

#### Tapered amplifiers

Tapered amplifiers are 500 mW laser diodes (SDL 8630E). By using a tapered gain region, the gain does not saturate as in standard rectangular gain regions, and higher output powers are achievable [80]. Because of the taper, the amplifier output is highly elliptical,  $\sim 100 : 1$  aspect ratio. A 2.8 mm aspheric lens is used to collimate the output in one dimension, and a 35 mm cylindrical lens is used to collimate the other



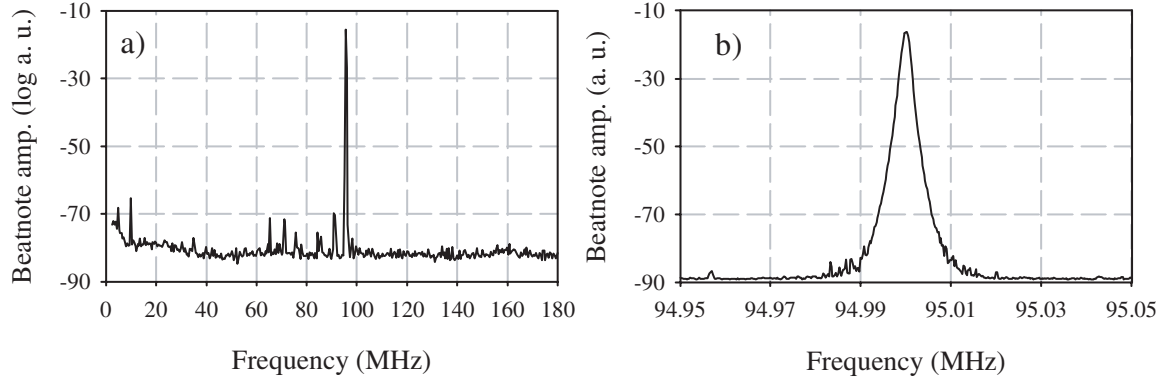


Figure 5.3: Beatnotes between a tapered amplifier locked and the master laser used to lock it on a) log scale and b) linear scale. The extra spikes in a) are due to rf pickup, and the power in the injected mode of the tapered amplifier is  $> 98\%$  of the total power.

axis. The injecting light is coupled into the rear of the tapered amplifier using a 4.5 mm aspheric lens preceded by an anamorphic prism pair to mode-match to the  $\sim 4 : 1$  aspect ratio of the tapered amplifier input. An injection power of  $\sim 10$  mW is required to produce 500 mW of output power. In order to produce the 10 mW necessary to lock two tapered amplifiers, the 5 mW Vortex first injections locks two 150 mW single-mode amplifier laser diodes (SDL 5422). Prior to this injection lock, the Vortex laser passes through the two double-passed AOMs described above, one for each amplifier laser, in order to provide frequency control during the experiment. The 150 mW amplifiers directly inject the tapered amplifiers with 10 mW each. The spectral purity of the tapered amplifier output is displayed in Fig. 5.3, which shows a beatnote between a tapered amplifier and a Vortex grating stabilized laser.

Although the tapered amplifiers provide high powers, there are several difficulties in using them. The fundamental problem lies with their pointing stability. The tapered amplifiers are mounted on water-cooled aluminum blocks which act as thermal reservoirs for the peltier coolers used to stabilize the amplifier temperatures. If the temperature of the cooling water changes, then the pointing of the laser can change slightly, and this slight pointing change is often sufficient to degrade the coupling into the optical fibers which deliver the light to the vacuum chambers. This problem could be surmounted with a redesign of the amplifier mount; however, there is also a

fundamental instability in the diode chips themselves. Even in a highly temperature-controlled environment, some pointing walk was observed. Directly replacing the most unstable laser with another laser of the same type, using the same cooling mount, reduced the pointing instability, which implies that there is a variation in the mechanical stability of individual laser chips.

In addition to the pointing instability, the anti-reflection coatings on the facets of the tapered amplifiers age and degrade rapidly, on the scale of around six months. This aging is manifested in a lower lasing threshold for free-running tapered amplifiers and increased mode-competition, making it difficult for the amplifier to operate in a single longitudinal mode. Single-mode operation requires greater injection power to overcome the mode-competition, and this higher power often shortens the life of the amplifier further. Finally the price and availability of the tapered amplifiers coupled with their short lifetime limits their utility.

### **Single-mode amplifiers**

A more stable and less expensive alternative to the tapered amplifiers is to use four of the SDL 5422 150 mW single-mode amplifiers instead of two tapered amplifiers. The overall power is lower in this configuration, but the stability is greatly increased. The single-mode amplifiers can be coupled into fibers with high efficiencies as well (55% as opposed to 35%), because their output is closer to diffraction-limited. These lasers require only several hundred  $\mu\text{W}$  of power to injection lock robustly and are stable over times of many days. The two lasers formerly used as auxiliary amplifiers for the tapered amplifiers now comprise two of the four single-mode amplifiers. Light from these two lasers is then used to drive two more single-mode amplifiers. These four lasers are coupled into fibers and delivered to the chamber. The fiber coupling of these lasers is stable to a few percent over a week, evidencing a vast improvement in the pointing stability relative to the tapered amplifiers. Each one of these lasers then drives three of the twelve total MOT beams. A block diagram of this configuration is shown in Fig. 5.4.

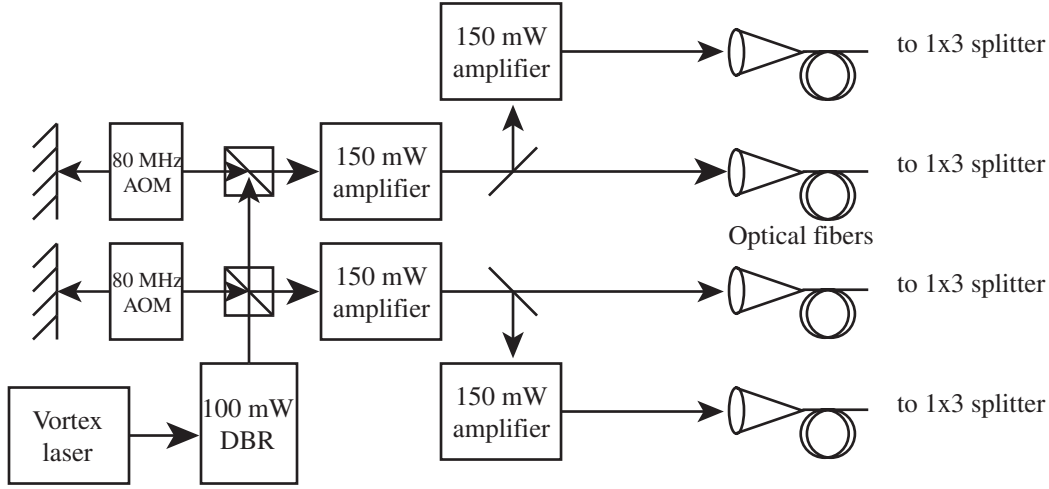


Figure 5.4: Schematic diagram of the trapping laser system using four single mode amplifier laser to provide three of the twelve trapping beams each. The two double-passed AOMs are used to tune the frequency of the lasers for cooling and launching of the MOT.

### 5.3.3 Optical fiber system

The amplifier lasers are coupled into optical fibers, split into twelve equal outputs, and delivered to the vacuum chambers for cooling and trapping (six fibers for each MOT). The fibers are PM fibers (Rifocs 2424) with an extinction ratio of 30 dB and are all FC-connectorized for ease of use and angle-polished to reduce etalon effects. In order to achieve maximum stability, a polarizing cube is used to purify the polarization of the input light directly before each fiber. A half-wave plate then aligns the polarization of the light to be along the axis of the PM fiber. Aspheric, FC-connectorized lenses are used for the fiber input coupling. In addition to PM fibers, polarizing (PZ) fibers were tested too. It was found that the polarization purity of the PM fibers is 3 dB - 6 dB greater than that of the PZ fibers. AOMs operating at 90 MHz are used to switch the light through the fibers as required during the experimental cycle.

The fiber configuration is slightly different depending on which amplifier lasers are used. When the tapered amplifiers were used, each tapered amplifier output was divided in half with a polarizing beamsplitting for each vacuum chamber. One tapered amplifier supplied light for the upper set of trapping beams in both chambers, and the

other supplied light for the lower set of trapping beams. In this way, identical light was used for the MOTs in each chamber, which provided a high degree of common-mode behavior between the two MOTs. After being split in two, each amplifier laser was further split into three equal outputs using a fiber beamsplitter system. The fiber splitters (Optics for Research Fiberbench system) consist of a polarizer to purify the polarization after the input fiber, half-wave plates and calcite polarizers to divide the beam into three equal outputs, and half-wave plates to align the polarization to the fiber. These fiber splitters are all low-profile optics mounted on a small steel base and have excellent stability (a few percent drift over several months). When the four separate 150 mW lasers are used to power the MOTs, each laser is coupled into a PM fiber and then into a three-way splitter. Each laser powers either the top set of three beams or the bottom set of three beams for one of the two MOTs.

## 5.4 Laser cooled atomic sources

The main purpose of the quiet, stable laser system is to obtain a bright source of cold atoms with minimal fluctuations in number. The trapping beams from the twelve fibers are delivered to the two vacuum chambers and are allowed to propagate uncollimated to the two MOTs. The beams first pass through a polarizing cube to purify the polarization and a quarter-wave plate to give the appropriate helicity for trapping. The MOTs are in the (1,1,1) configuration, *i.e.* with three beams pointing downward and three beams pointing upward. The polarizations of the beams are  $\sigma^+ - \sigma^-$  for opposing beams. By not collimating the beams, the beam size limit imposed by the window apertures was circumvented. Using uncollimated beams for the MOTs gives a factor of two improvement in total number of atoms trapped versus collimated beams. The approximate beam waist at the trapping position is 2.5 cm ( $1/e^2$ ), and the intensity is about  $1.2 I_{\text{sat}}$  per beam. The trapping beams are detuned 8 MHz to the red of the  $F = 4 \rightarrow F' = 5$  cooling transition.

The MOTs are loaded from a thermal vapor of Cs. The Cs reservoir in the cold finger is maintained at  $\sim 10^\circ \text{C}$  by a thermoelectric cooler. The exact Cs partial pressure is maintained by operating with the cold finger valve partially open to control

the flow of Cs to the trapping region. The optimal vapor pressure is chosen by opening the valve until the number of atoms detected after the fountain ceases to increase. If opened further, the increased vapor pressure reduces the number of atoms in the MOT due to collisions with untrapped atoms during the atomic fountain. At around this vapor pressure, collisions start to decrease interferometer contrast as well. With optimal vapor pressure and optimized loading parameters, the traps contain about  $2 \times 10^8$  atoms in each MOT.

After loading the MOTs from a thermal vapor for 1 s, the molasses beam detuning is increased to 20 MHz in order to compress the MOTs. Then the cold atoms are launched in ballistic trajectories in atomic fountains. The trapping quadrupole magnetic fields are turned off prior to launching. Because the vacuum chambers are aluminum, the atoms must be held in the 20 MHz detuned optical molasses for 30 ms while the eddy currents from the field switching damp out<sup>3</sup>. Following this holding period, for each MOT, the frequency of the upper three molasses beams are ramped down by 1 MHz over 5 ms using the double-passed AOM for frequency control, while the frequency of the lower three beams is ramped up by an equal amount. This frequency ramp smoothly transfers the atoms to an optical molasses moving at 1.5 m/s (see Fig. 5.5). This ramp is necessary to transfer all atoms to the moving frame, as a discontinuous jump into the moving frame leaves a significant portion of the atoms behind. To cool the atoms to a final temperature of  $2.3 \mu\text{K}$ , the frequency of the trapping beams is stepped down to about 40 MHz detuned, still in a moving molasses, and the intensity is ramped down to half intensity in 1 ms, held for 0.5 ms, and ramped completely off in 0.5 ms more. All of the frequency and intensity ramps are accomplished using direct digital synthesis from the Hewlett Packard HP8770A AWGs and are highly stable. Following this launching and cooling phase, the cold atoms move freely in a 320 ms, 12 cm high fountain during which they are prepared in a special state and then interrogated by the interferometer sequence.

---

<sup>3</sup>In retrospect, a chamber constructed out of titanium alloy or glass would have solved this problem without sacrificing the magnetic purity of aluminum. However, precision machined titanium is expensive and glass is difficult to anti-reflection coat in the required chamber geometry. Future designs most likely will employ different materials.

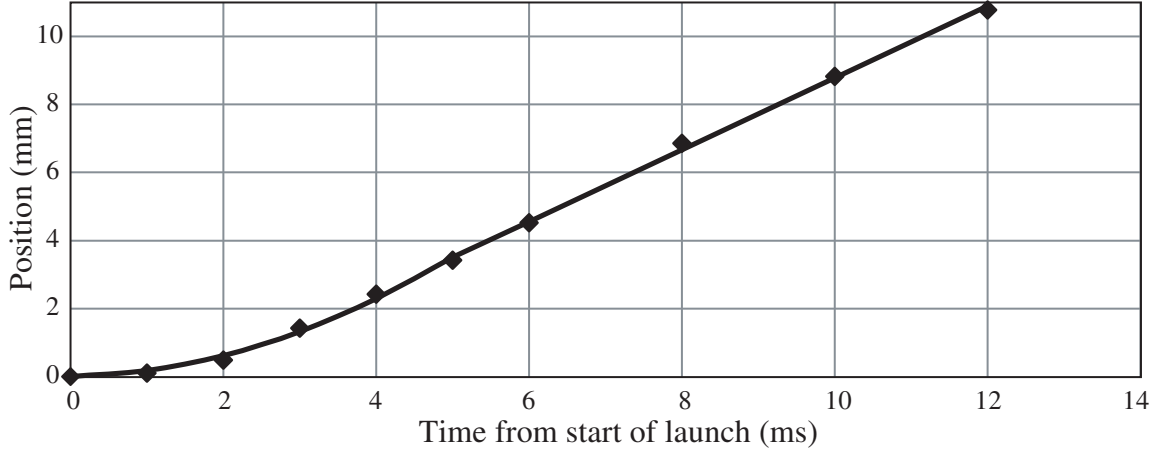


Figure 5.5: Position of the cold atoms as measured by detecting scattered fluorescence with a CCD camera during the launch phase. The atoms are slowly ramped into the moving frame, where they move with constant velocity. The solid line is a quadratic fit for the acceleration during the initial ramp, followed by a linear fit for the atoms moving with constant velocity in the moving molasses after the ramp is concluded. The launch velocity shown is slightly less than the typical launch velocity.

## 5.5 State preparation

Before the atom interferometer, a selection sequence prepares the atoms in a magnetically insensitive  $m_F = 0$  sublevel and also selects atoms with a narrower velocity spread than the total spread of the cold cloud. The state selection is important for obtaining good fringe contrast in the atom interferometer while using as many atoms as possible. A sequence of microwave and Doppler-sensitive Raman pulses accomplishes this selection. The details associated with this state selection are discussed below.

Following their launch, atoms are initially distributed nearly evenly among the magnetic sublevels of the  $F = 4$  ground state. Three orthogonal pairs of magnetic field coils, roughly in a Helmholtz configuration, zero the Earth's magnetic field and apply a vertical bias field of  $\sim 100$  mG. This bias allows selective addressing of individual  $F = 3$  to  $F = 4$  ground state hyperfine transitions with a 9.2 GHz microwave field (delivered to the atoms through a Narda 640 X-band gain horn). First, a microwave composite  $\pi$  pulse (see section 5.5.2) transfers atoms from the  $F = 4$ ,  $m_F = 0$  to

the  $F = 3, m_F = 0$  sublevel. Composite pulse sequences accomplish the population transfer more closely to an ideal  $\pi$  pulse in an experimentally robust way, as described in section 5.5.2. Next, a near-resonant pulse from the upper trapping beams tuned slightly above the  $6S_{1/2}, F=4 \rightarrow 6P_{3/2}, F' = 5$  transition clears atoms in the remaining  $F = 4$  sublevels (via the scattering force). Another composite microwave  $\pi$  pulse then returns  $F = 3, m_F = 0$  atoms to  $F = 4, m_F = 0$ . An optical velocity selective composite Raman  $\pi$  pulse is now applied which transfers  $F = 4, m_F = 0$  atoms within the velocity range encompassed by the Raman pulse envelope to  $F = 3, m_F = 0$ . Finally, a second, near resonant, blue detuned pulse clears away the remaining  $F = 4$  atoms. At this point, the remaining (state prepared) atoms are ready for use in the interferometer. A considerable fraction of atoms are eliminated from the initial ensemble in this process:  $\sim 8/9$  from the internal state selection and another  $\sim 2/3$  in velocity selection, leaving roughly 4% for the interferometer. This sequence is schematically shown in Fig. 5.6 (note that the figure is not to scale as the state preparation and optical pumping only take  $\sim 2$  ms).

### 5.5.1 Optical pumping

In order to increase the  $m_F = 0$  population, an enhanced optical pumping scheme has been implemented. This method essentially recycles atoms which are not initially in the  $m_F = 0$  state by a cyclic optical pumping sequence. In practice as much as a factor of three improvement in usable atoms was observed with this method.

The sequence begins with a composite microwave  $\pi$  pulse applied to drive atoms from the  $F = 4, m_F = 0$  to the  $F = 3, m_F = 0$  state as before. Then a de-pumping beam tuned to the  $F = 4$  to  $F' = 4$  transition is applied to optically pump the remaining atoms from  $F = 4, m_F \neq 0$  into  $F = 3$ . The de-pumping process incoherently redistributes the atomic population, with approximately  $1/7$  of the remaining atoms ending up in  $m_F = 0$ . The process is then reversed with a composite microwave  $\pi$  pulse transferring  $F = 3, m_F = 0$  to  $F = 4, m_F = 0$  followed by application of a repumping beam to the  $F = 3$  to  $F' = 4$  transition. In principle, this entire sequence could be repeated many times, resulting in an ideal pumping efficiency of 100%.

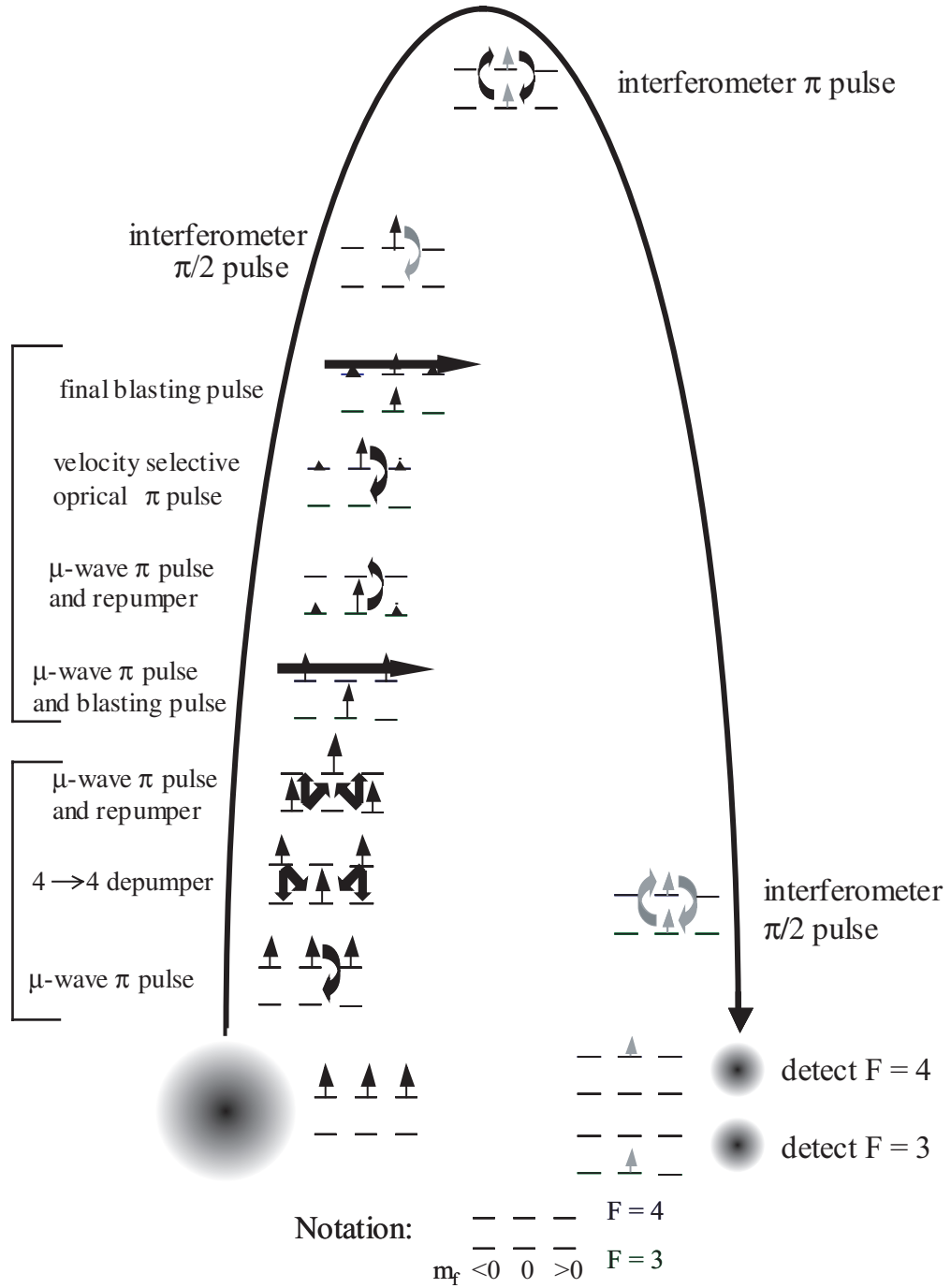


Figure 5.6: Diagram showing the atomic fountain with the state preparation, interferometer, and detection pulses. The atomic state is depicted by arrows in the level diagrams. Gray arrows represent superposition states.



In practice, inefficiency of the microwave pulses (see section 5.5.2), heating due to spontaneous emission in the pumping sequence, and the availability of only a finite amount of time to execute the sequence limit the process efficiency. We realize a factor of three improvement with just one cycle of the sequence described in the previous paragraph.

For vapor cell loaded traps there is another effect which limits the overall efficiency by the presence of the background atomic vapor. In this case, the de-pumping photons can excite atoms in the background vapor which then can emit light at the repumping frequency as they spontaneously decay. These rescattered photons then redistribute atoms in the  $F = 3$ ,  $m_F = 0$  state to other  $m_F \neq 0$  states. Thus there is a trade-off between background vapor pressure (which sets the loading rate) and the overall efficiency of the pumping scheme (which works best at low vapor pressure). For the operating parameters of this experiment, the optical pumping typically improves the usable number of atoms by a factor of 1.5 - 2. Finally, it is noted that this method substantially increases shot-to-shot atom number fluctuations (from 200:1 to 60:1). However, the normalized detection method is able to effectively suppress the impact of these fluctuations on the interferometer signals. It is not understood what drives the increased noise.

### 5.5.2 Composite pulse techniques

The above state preparation methods work best with efficient coherent population transfer between  $F = 3$  and  $F = 4$  states. Less than unit transfer efficiency during a standard  $\pi$  pulse between the ground states can result from an inhomogeneous Rabi frequency of the microwave or optical pulse seen by the atoms, as well as by detunings due to the velocity spread of the atoms. In this apparatus, the microwave  $\pi$  pulses are typically only 80% efficient due to inhomogeneous field strengths across the atom clouds (since the microwave transitions are driven with horns placed outside the vacuum chamber). Furthermore, the state selection and optical pumping require a series of one optical and four microwave  $\pi$  pulses in the two separate chambers. With the current system, it is difficult to match the pulse conditions for all pairs of

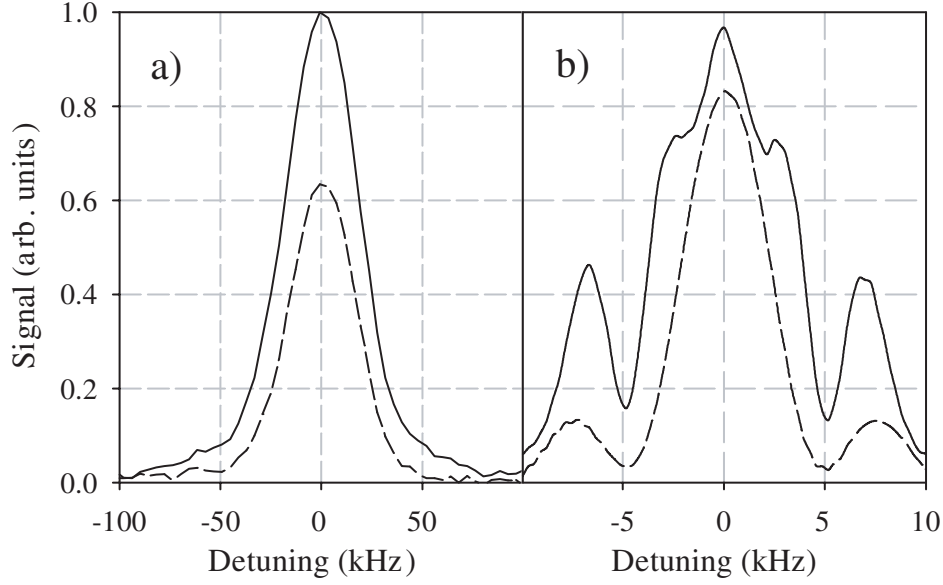


Figure 5.7: A comparison of the transfer efficiency of composite  $\pi$  pulses (solid traces) with regular  $\pi$  pulses (dotted traces) in (a) optical Doppler sensitive transitions and (b) microwave transitions. The detuning shown is from the  $F = 4 \text{ m}_F = 0 \rightarrow F = 3 \text{ m}_F = 0$  transition. The finer structure of the optical transition is not visible due to inhomogeneous broadening from the thermal width of the atoms.

pulses due to different microwave intensity gradients in each chamber.

Borrowing from techniques pioneered in nuclear magnetic resonance work [81, 82], in composite pulse sequences a standard  $\pi$  pulse is replaced with a sequence of pulses with variable area and relative phase. In this work, a  $\pi/2 - \pi_{90^\circ} - \pi/2$  pulse sequence is employed in place of a  $\pi$  pulse. The subscript  $90^\circ$  indicates that the phase of the center  $\pi$  pulse is shifted  $90^\circ$  relative to the  $\pi/2$  pulses. The use of this sequence increases the transfer efficiency of a pulse for inhomogeneous distributions of Rabi frequency and detuning across the atomic ensemble. Employing these pulses for the microwave state preparation pulses increases the transfer efficiency from 80% with a regular  $\pi$  pulse to 95%, and composite pulses give a 60% increase in efficiency for optical transitions. Fig. 5.7 compares a frequency scan with regular and composite  $\pi$  pulses. The transfer efficiency is plotted as the detuning of the fields are swept across the resonance for both microwave and optical Doppler sensitive transitions. More advanced interferometer pulse sequences may benefit from the use of composite

pulses for the optical pulses (see Fig. 5.7) but are not employed at the moment (see section 7.2.2).

In comparison with the adiabatic rapid passage technique (ARP), where the detuning of the laser is swept across the resonance rapidly so that the state vector follows adiabatically [51], composite pulses are easier to implement experimentally and require less time (or total pulse area) to achieve efficient transfer. For example, it is found that approximately  $5\pi$  total time (here time is referenced to the time to drive a  $\pi$  pulse at the resonant Rabi frequency) is needed for ARP to achieve results similar to those achieved with only  $2\pi$  time for the composite sequence. Additionally, ARP gives significantly more spontaneous emission for optical pulses due to the increased length.

## 5.6 Atom interferometer

This section describes the operation of the atom interferometer and the directly related subsystems. The generation of the Raman lasers is detailed, as well as their delivery to the atoms. A technique to remove systematics based on the reversal of the propagation vector of the Raman beams is presented. The rationale behind the specific Raman beam operating parameters is discussed. Finally, the operation of the interferometer itself is described.

### 5.6.1 Raman lasers

As the acceleration-induced phase shifts depend critically on the phase and wavevector associated with the laser beams used to drive stimulated Raman transitions, possible contributions of laser frequency noise to the relative stabilities of the interferometer signals is analyzed. The constraints on laser frequency stability are considered here, and then the Raman laser system which was designed to meet these constraints is described.

In the gradiometer geometry, the two ensembles are separated by  $\sim 1.4$  m. The Raman fields propagate in an asymmetric way to these ensembles as seen in Fig. 5.8.

The rationale behind the asymmetric design is given in section 5.6.2. Consider the propagation paths of the optical fields following the beamsplitting optic which separates the two Raman fields. The beam of frequency  $\omega_1$  propagates roughly  $x_1^1 \simeq 0.3$  m before it passes through the first ensemble of atoms, while it propagates roughly  $x_1^2 \simeq 1.7$  m before it passes through the second ensemble. On the other hand, the beam of frequency  $\omega_2$  propagates  $x_2^1 \simeq 3.7$  m before it passes through the first ensemble, while it propagates  $x_2^2 \simeq 2.3$  m before it passes through the second ensemble.

If the laser frequencies drift on a time scale short compared to the interrogation time  $T$  between pulses, an asymmetric phase shift will be read into the atomic coherences due to this path asymmetry. For example, suppose the laser frequency jitter is  $\delta\omega$ , while the differential path length travelled by the Raman lasers for the two ensembles is

$$\begin{aligned}\ell &\equiv (\text{effective path to ensemble 1}) - (\text{effective path to ensemble 2}) \\ &= (x_2^1 - x_1^1) - (x_2^2 - x_1^2) \simeq 2.8\text{m}.\end{aligned}\tag{5.1}$$

This frequency noise leads to differential phase noise of  $\delta\phi_{\text{laser}} \sim (k\ell)(\delta\omega/\omega)$ . For a target interference SNR of 1000:1,  $\delta\phi_{\text{laser}} < 1$  mrad. For our parameters, this implies  $\delta\omega < 2\pi \times 20$  kHz.

In order to achieve frequency stability at this level, a second Vortex laser is used as the master laser for the Raman laser system. This laser is locked to the  $6\text{S}_{1/2}$ ,  $F = 3 \rightarrow 6\text{P}_{3/2}$ ,  $F' = 2$  crossover resonance (also via modulation transfer spectroscopy) using several AOMs to offset the frequency to obtain the desired Raman detuning. The lock is maintained through the use of a digital signal processor (DSP, Spectrum Signal Indy TMS320C32). The DSP processes the lock error signal through a highpass and lowpass channel, each operating at a sampling rate of 25 kHz. The high and low frequency channels are divided to provide feedback to the laser current and to the cavity piezo element respectively. Due to the presence of long term drift in the piezo element a third, very low frequency channel is provided through a GPIB command to the laser controller, which allows the laser to stay locked over several days. The measured stability of the laser is comparable to that of the master laser used for

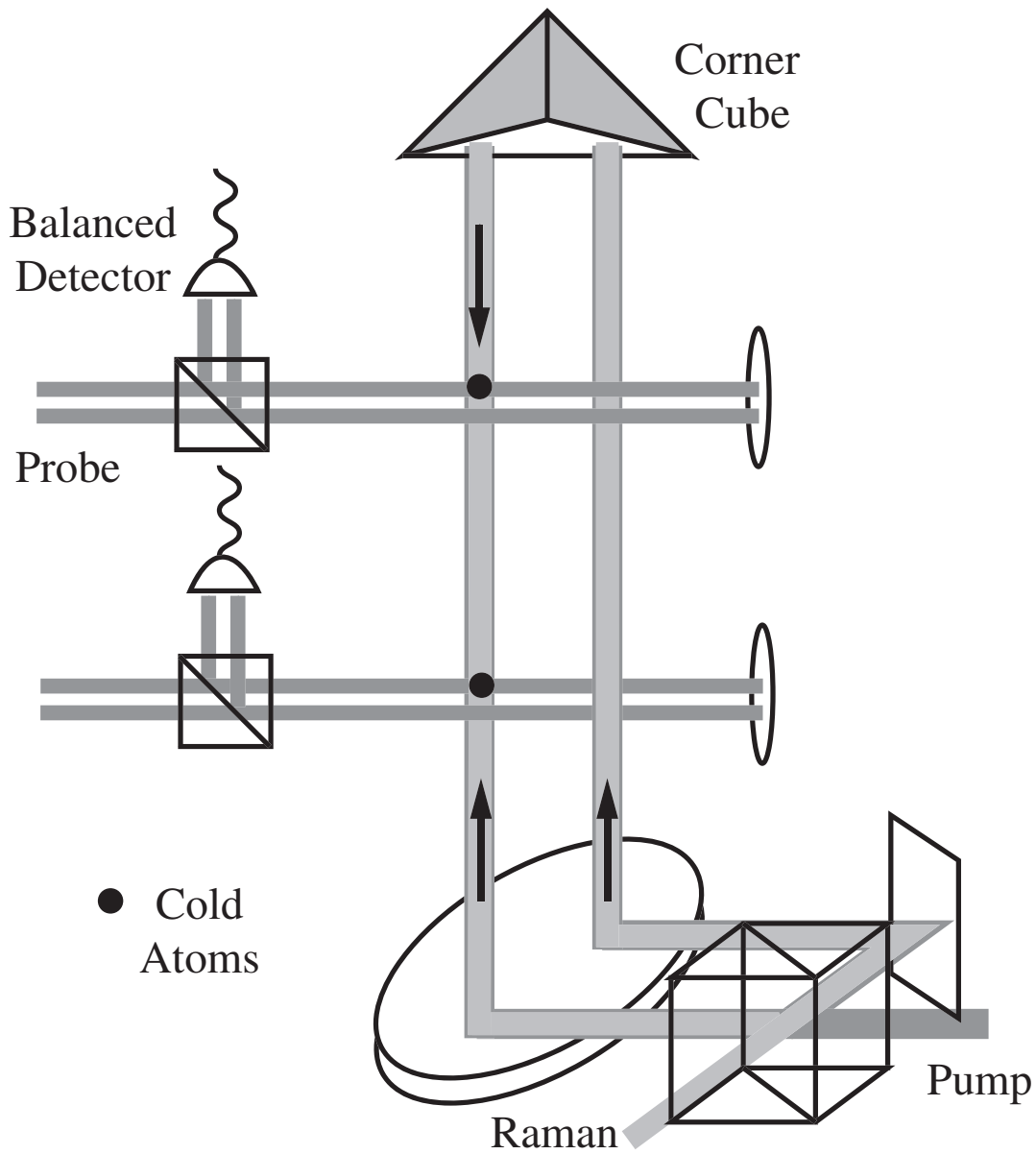


Figure 5.8: Schematic illustration of the Raman beam racetrack geometry showing the detection beams as well. The figure is not to scale, as each atom cloud is less than 1 cm in diameter, and the separation between chambers is 1.4 m.

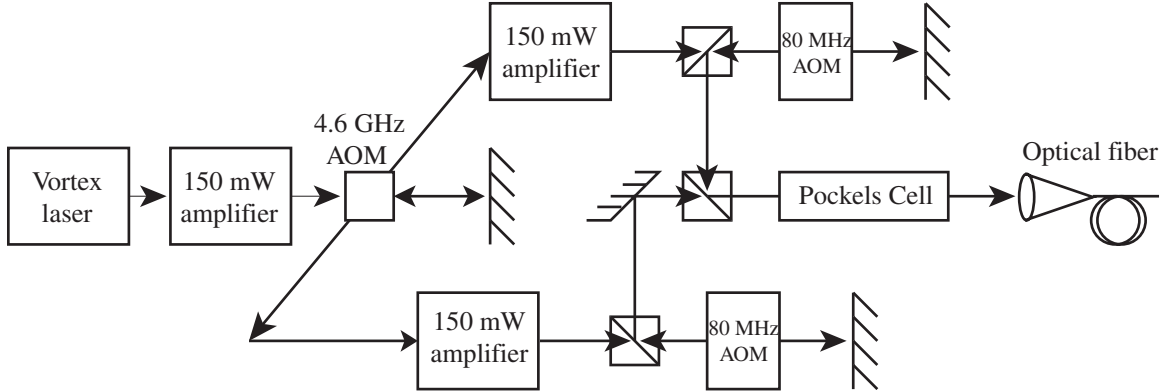


Figure 5.9: Schematic of the Raman laser system, showing the master and slave lasers along with the low and high frequency AOMs for frequency and phase control.

the optical molasses and is primarily limited by a 5 kHz resonance of the laser's piezo-electric transducer.

The Vortex laser directly injection locks a 150 mW (SDL 5422) slave diode laser. This laser is then shifted up and down in frequency by 4.756 GHz (160 MHz above half the Cs hyperfine splitting) with a high frequency AOM. The diffracted orders are then used to injection lock two more 150 mW slave laser diodes at a frequency 700 MHz red detuned from the  $F = 3 \rightarrow F' = 4$  and  $F = 4 \rightarrow F' = 4$  transitions, respectively [83], as shown in Fig. 5.9. The frequency noise on the master Raman laser exists on both the slave lasers, but their frequency separation remains fixed at the Cs ground state hyperfine transition. The 700 MHz detuning from the  $F' = 5$  level reduces the effect of spontaneous emission due to off-resonant single photon excitations from each Raman beam.

### 5.6.2 Beam delivery

The Raman beams are delivered to the vacuum chambers with a polarization maintaining optical fiber in order to increase the pointing stability of the Raman beams as well as to spatially filter them. Prior to coupling into the fiber, the two Raman beams are double-passed through 80 MHz AOMs. These AOMs are controlled by another HP8770 AWG which allows dynamic frequency, phase, and intensity tuning

of the Raman beams during the interferometer pulse sequence. During the interferometer, the frequency of the Raman lasers must be chirped in order to maintain a resonance condition with the accelerating (Doppler shifting) atoms<sup>4</sup>, as described in section 4.4.1. The chirp is accomplished digitally in a phase-continuous way, *i.e.* each pulse applied to the AOMs for the Raman pulses is a short pulse taken from a single continuously chirping waveform. It is this phase continuity that causes  $\Delta\phi^\circ$  from section 4.4.2 to be zero for each accelerometer in the absence of vibrational phase noise. The double-passes themselves are necessary to prevent the frequency chirp from turning into an unwanted amplitude chirp via the beam pointing changing along with the chirp and degrading the coupling of the beam into the delivery fiber. This optical path is schematically shown in Fig. 5.9. Furthermore, the AOMs are first switched on far off-resonance at low power 20  $\mu$ s before each Raman pulse in order to remove phase noise associated with switching the Raman beams on. The low power, off-resonant pulses couple little light into the fiber and have negligible effects on the interferometer.

The two Raman beams are overlapped with orthogonal linear polarizations on a polarizing beamsplitting cube and passed through a Pockel's cell polarization modulator (ConOptics 350-50) after the double-passed AOMs. The Pockel's cell is used to reverse the effective Raman laser propagation direction  $\mathbf{k}_{\text{eff}}$ , as described below. The Raman beams then are coupled into a polarization maintaining fiber with 75% efficiency and sent to the gradiometer. For wavefront quality after the fiber spatially filters the beams, the Raman beams are collimated with a 1.1 cm focal length aspheric lens in conjunction with a high surface quality 50 cm focal length spherical lens. This lens combination results in a uniform phase front for the Raman beams. After collimation the Raman beams have a 1.0 cm ( $1/e$ ) beam waist. All optics in the Raman beams' propagation path after the optical fiber are of high surface figure ( $\lambda/10$  or better) in order to preserve the phase front homogeneity of the Raman beams<sup>5</sup>. With these operating parameters, and a typical one-photon detuning of 1 GHz, the resonant two-photon Rabi frequency is  $\sim 40$  kHz.

---

<sup>4</sup>The Doppler shift across a 300 ms interrogation time is  $2\pi \times 7$  MHz for a two-photon transition.

<sup>5</sup>A poor quality Raman phase front causes dephasing in the interferometer as the atoms essentially see random position-dependent phases.

There are several different Raman beam geometries that generate the two counterpropagating Raman beams necessary to drive the interferometer transitions. The most straightforward geometry is to allow the two Raman beams to copropagate after collimation through the two atom ensembles and then to retroreflect them with a high surface quality mirror on the far side of the vacuum chambers. The major advantage of direct retroreflection, besides its simplicity, is no extra optics are required to split the two Raman beams. Using no extra optics means the beams are not apertured by the size of the optics, thereby reducing diffraction effects in the Raman beams. Even with appropriate polarization optics in place, direct retroreflection can produce standing waves of the Raman light fields. Standing waves cause interference, leading to an intensity modulation of the light field. This can introduce amplitude noise on the interference fringes as the atoms experience non-ideal, fluctuating interferometer pulse areas from shot-to-shot. These fluctuations vary at the positions of the two interferometers and therefore contribute non-common noise to the gradient signal. Also, spontaneous emission is double in this configuration relative to two purely counterpropagating light fields.

The direct retroreflection geometry was abandoned in favor of a racetrack geometry. After collimation, the Raman beams enter a racetrack geometry in order to obtain counterpropagating beams for the Raman interaction (see Fig. 5.8). The racetrack configuration starts with a polarizing beamsplitter cube that separates the two orthogonally polarized Raman beams. The two Raman beams then parallel propagate vertically through the vacuum chambers with one beam passing through the axis of the atom ensembles and the other 2 cm off-axis. After passing through both chambers, a corner cube retroreflector redirects the off-axis Raman beam to counterpropagate with the on-axis Raman beam, resulting in two counterpropagating beams. The use of the corner cube decreases the tilt sensitivity of the apparatus by keeping the Raman beam propagation axis constant as the cube is subjected to spurious tilts. In this racetrack, standing waves are eliminated, which maintains overall intensity stability by suppressing etalon effects from the Raman beams. Also, spontaneous emission is reduced by half compared to using collinear retroreflected beams.



Furthermore, a fluctuating index of refraction of the medium between the chambers will cause differential phase noise too, appearing as a fluctuating effective path length similar to the way laser frequency noise couples into the measurement. For these measurements, it is sufficient to use a tube between the two chambers to shield the beam path from air currents. For higher sensitivity measurements however, it might become necessary to fill the region between the chambers with helium or even to evacuate it.

### 5.6.3 Propagation reversal

A technique to reduce many systematic interferometer phase shifts involves reversing the effective Raman propagation vector  $\mathbf{k}_{\text{eff}} = \mathbf{k}_1 - \mathbf{k}_2$ . Because the gravitational phase shift is proportional to  $\mathbf{k}_{\text{eff}} \cdot \mathbf{g}$ , reversing the sign of  $\mathbf{k}_{\text{eff}}$  changes the sign of the gravitational phase shift. However, several systematic phase shifts, such as second-order Zeeman shifts from magnetic fields and any residual AC Stark shifts, have no dependence on the Raman wavevector direction. Subtracting the phases obtained from consecutive experimental cycles using two reversed propagation directions gives twice the gravitational phase shift, but removes these systematic shifts. The propagation reversal is accomplished using the Pockel's cell. The Pockel's cell rotates the polarization of both Raman beams by  $90^\circ$  when activated. This rotation causes the direction the Raman beams take through the racetrack to switch, *i.e.*  $\mathbf{k}_{\text{eff}} \rightarrow -\mathbf{k}_{\text{eff}}$ . The propagation direction can be switched from one shot to the next, but is typically only switched after scanning 16 points over an interference fringe with each propagation. In practice this has been shown to remove magnetic phase shifts by at least 26 dB. When the propagation is switched, the rf applied to the low frequency AOMs must be changed to accommodate the Doppler shift, which changes sign with the propagation reversal. In addition, when switching the propagation direction, the Pockel's cell requires about  $150 \mu\text{s}$  to completely settle before any pulses are applied, in order to not produce polarization noise on the Raman beams.

To illustrate the efficacy of the common-mode rejection of systematics using the

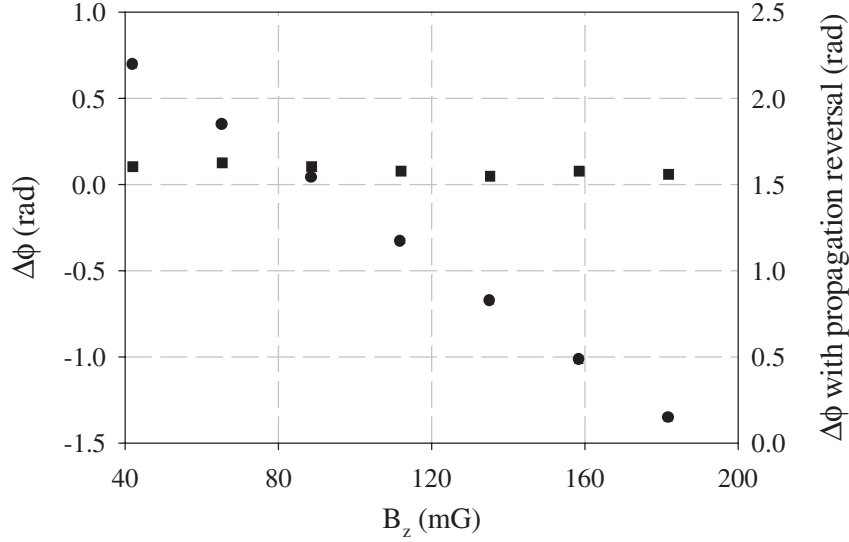


Figure 5.10: Rejection of induced magnetic phase shifts using reversal of the Raman wavevector. The circles show the raw phase shifts from one of Raman propagations as a function of the magnetic bias field  $B_z$ , and the squares show the phase obtained from subtracting the reversed propagation.

propagation reversal method, a magnetic phase shift was induced in one interferometer. An extra magnetic field in the vertical direction was applied using the Helmholtz coils which are used to zero the ambient magnetic field and to apply the small bias which defines the spin axis of the atoms. The Zeeman phase shift then was removed by switching between the two propagations, subtracting the resultant phase shifts, and dividing by two to leave only the phase shift due to gravity. This study is shown in Fig. 5.10. This rejection represents a reduction of systematic magnetic phase shifts by at least 30 dB.

#### 5.6.4 Raman beam parameters

A theoretical study of the interferometer contrast as a function of Raman beam waist and detuning was performed. The finite Raman beam size gives rise to a spatially inhomogeneous Rabi frequency across the atom cloud, causing dephasing during the interferometer. Similarly, the velocity spread of the atoms along the Raman beams causes more inhomogeneous broadening due to differential Doppler shifts across the

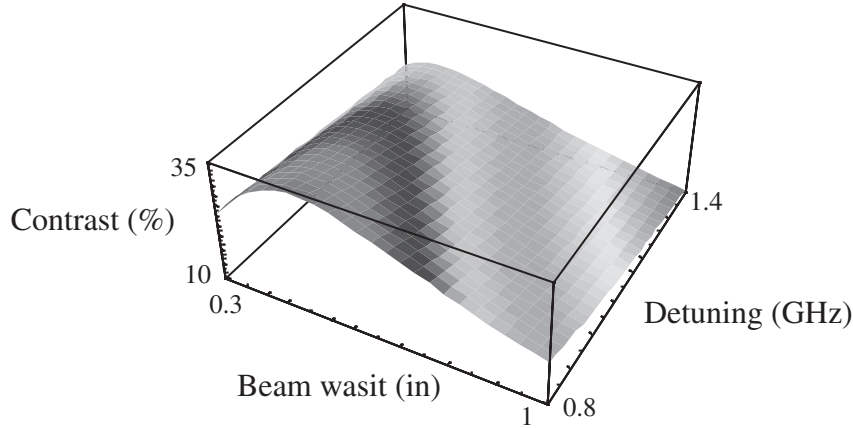


Figure 5.11: Simulation of interferometer fringe contrast used to find the optimal Raman beam size and detuning (shown here from the  $F = 4 \rightarrow F' = 5$  transition).

atom ensemble. Typical Rabi frequencies are around 30 kHz, and the thermal width is about 45 kHz. The Rabi frequency of the Raman transitions scales inversely with detuning; thus the detuning characterizes the velocity selectivity of the Raman pulses. Incorporating a finite beam size and a Boltzman distribution for the velocity of the atoms, the results indicated an optimal 30% contrast for a Raman beam waist of 1.0 cm radius ( $1/e$ ), and a detuning of  $\sim 1$  GHz from  $F' = 5$ , which is the chosen operating point. Fig. 5.11 shows the results of the simulation. This simulation assumed a constant available Raman beam power and found the beam waist and detuning which minimized the dephasing from the velocity spread and the nonuniform intensity profile of the Raman beams by integrating over the atom cloud.

In addition to the interferometer contrast, systematic AC Stark shifts were studied. AC Stark shifts from the Raman pulses themselves cause spurious phase shifts in the interferometer if unconstrained. However, with a two-photon Raman transition, the AC Stark shift is the difference between the individual AC Stark shifts from each beam and can be zeroed by adjusting the ratio between the two Raman beams. The Stark shift is balanced with a beam intensity ratio of  $\sim 1.6:1$  for the chosen Raman detuning. The Stark shift is balanced empirically by inserting off-resonant Raman pulses within a microwave  $\pi/2 - \pi - \pi/2$  interferometer and adjusting the Raman beam intensity balance to zero the optically induced phase shift. This ratio of 1.6:1

for the chosen Raman detuning agrees well with theoretical predictions.

### 5.6.5 Interferometer operation

The gradiometer is typically operated in its most sensitive configuration with the interferometer pulses at a spacing of  $T = 150$  ms. The interferometer time can be lengthened to as much as  $T = 157.5$  ms, but care must be taken to avoid driving transitions at the apex of the atomic fountain. At this point, the atoms have zero velocity, and Doppler sensitive transitions are degenerate with Doppler insensitive transitions which can be driven due to small amounts of polarization impurity in the Raman beams. The maximum interferometer time is limited by the vacuum chamber size which constrains the fountain height to 12 cm. Following the three-pulse interferometer sequence, the population distribution of the atoms in each ensemble is measured using the method described in section 5.7. In order to obtain interference fringes and extract the gravitationally-induced phase shift, the phase of an interferometer pulse needs to be scanned. The scanning is accomplished digitally with the AWG by scanning the phase of the rf waveform applied to the low frequency AOMs in the Raman beam paths. Any of the pulses can be scanned to produce fringes; typically the first pulse is scanned. This phase scanning is in addition to the frequency chirp to counteract the Doppler shift applied during the pulse. Typically the phase is scanned over  $2\pi$  rad in 16 points. The number of points is kept small to limit drift of signal amplitude and fringe contrast. Within a period shorter than the drift time, the length of a scan is not important, as the noise behaves as a white noise source.

## 5.7 Detection system

### 5.7.1 Background

In order to realize a sensitive gravity gradiometer, the atoms must be detected with high precision following the interferometer. Standard techniques for atom detection include measuring scattered fluorescence or absorption. Both these techniques require careful stabilization of the amplitude and frequency of the probe light to achieve a high

SNR. Fluorescence detection can be hampered by significant scattered light from the background thermal vapor, although it can achieve quantum projection (shot noise) limited performance under the right conditions [84]. In this experiment fluorescence detection of cold atoms was limited to a SNR of 300:1 by photon shot-noise from light scattered by background atoms in the vapor-cell trap due to the small solid angle of light scattered by the cold atoms collected by the detection system. Using FM probe light in fluorescence detection suppresses the background signal, but does not improve the photon shot-noise limited SNR. Using absorption of the probe beam effectively collects the entire amount of light scattered from the cold atoms and overcomes this noise source. However, due to the large background of unabsorbed light, absorption detection places very tight constraints on probe amplitude and frequency stability. Use of a FM probe (in a Pound-Drever-Hall configuration [85]) eases these constraints, but residual amplitude modulation<sup>6</sup> (RAM) at the  $10^{-5}$  level limited the SNR to 100:1. In order to overcome these limits, a balanced, modulation transfer detection system was designed to eliminate background vapor noise as well as to maximize the SNR limit from the cold atoms.

Balanced detection makes use of the fact that the experiment requires detection of atoms in a coherent superposition of two internal atomic states following an atom interferometer, *i.e.* detection of population differences. Common-mode suppression of technical noise sources arising from laser amplitude and frequency noise is made possible by detecting population differences. In the method described below, following the interferometer, the two states are spatially separated using light induced forces, which also projects the coherent superposition onto a statistical mixture of atoms in each of the two states. After the spatial separation, the absorption of two near resonant probe beams (each derived from the same laser) is measured on a balanced photodetector (where the photocurrents from two matched photodiodes are subtracted before amplification). In the case of equal populations between the two atomic states, this simultaneous differential detection produces a null signal, with high immunity to frequency or intensity noise from the laser.

---

<sup>6</sup>Residual amplitude modulation occurs due to etalon effects affecting the frequency modulated sidebands differentially, leading to amplitude modulation.

In addition, a modulation transfer technique is employed to further suppress technical noise sources. A near-resonant FM pump beam and a probe beam are overlapped on the cold atoms cloud. The FM pump beam modulates the complex index of refraction of the atoms, which in turn modulates the absorption of the probe beam [86, 87] through a nonlinear four-wave mixing process [88, 89, 90]. The amplitude modulation on the probe is detected on a photodetector and mixed down to DC. The pump and probe beams are aligned to be nearly orthogonal. This provides a Doppler selectivity to atoms at or near rest velocity, thus rejecting spurious signals from the background thermal vapor (which is Doppler-shifted out of resonance with the pump and/or probe beams). Furthermore, transfer of the RAM on the pump beam to the probe beams is a second-order effect and should be reduced to less than  $10^{-10}$ . Any residual signal arising from the thermal vapor signal is also rejected by the balanced detection method described in the previous paragraph.

### 5.7.2 Detection apparatus

Balanced, modulation transfer detection was demonstrated using the gravity gradiometer apparatus [91]. The pump and probe beams were derived from two of free running slave lasers described in section 5.3.2. The pump beam was modulated using an electro-optic modulator (EOM) placed before the injection-locked laser to reduce RAM<sup>7</sup>. The pump and probe beams were switched into polarization maintaining optical fibers using AOMs and delivered to the detection region. In order to be matched to the atom cloud size, each beam was collimated to 7 mm diameter ( $1/e^2$ ) with the pump beam propagating vertically through the vacuum chamber, orthogonal to the two horizontally propagating probe beams, each vertically separated (by 2.5 cm) (see Fig. 5.12). The exact size of the beams was determined to not be critical. All beams were retroreflected to avoid driving the cold atoms out of the detection region via momentum transfer. The pump beam uses the Raman racetrack depicted in Fig. 5.8.

The modulated absorption of the two probe beams was measured with a balanced

---

<sup>7</sup>Injection locks are effective at removing amplitude noise from the injecting beam

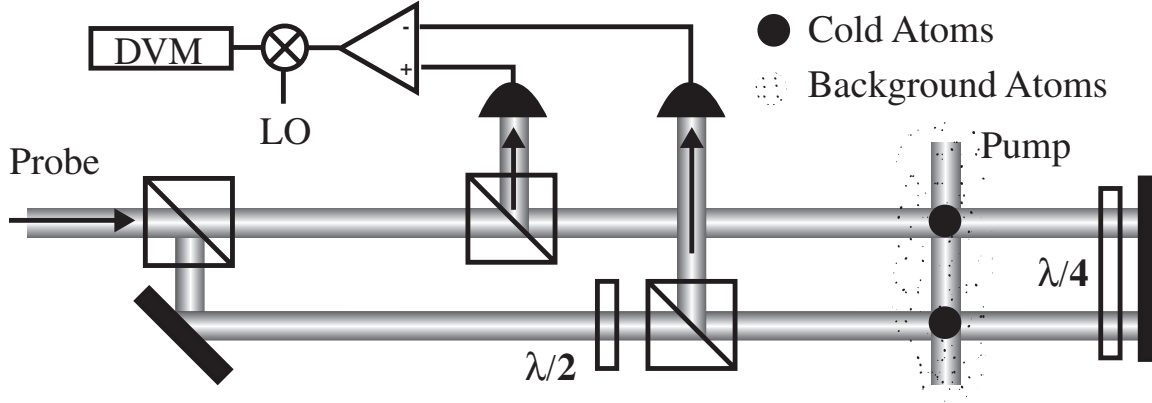


Figure 5.12: Diagram of the detection apparatus with two parallel probe beams for balanced detection and orthogonal pump beam for modulation transfer. The probe beams were detected on a balanced detector, mixed down to DC with a local oscillator (LO), and integrated on a digital voltmeter (DVM). All cubes are polarizing beamsplitters.

homodyne detector (Femto HCA-S), which consists of two matched Si PIN photodiodes, and which provides 40 dB of common mode noise rejection. Typical absorption levels for the cold atom signal were 0.1% for  $10^6$  atoms, while absorption by the background vapor was 8%. The signal from the balanced photodiode was mixed down to DC and acquired on a HP 3458A low-noise digital voltmeter. An identical setup of two probe beams and another balanced detector was used on the second interferometer using the same vertical pump beams and probe beams derived from the same laser.

The exact intensity, detuning, modulation, and polarization parameters for the pump and probe beams were chosen after a systematic study of their effect on the modulation transfer signal size (see Fig. 5.13). An AOM was used to shift the relative frequency between the pump and probe beams, and the signal size was strongly dependent on the probe detuning and the pump carrier detuning being the same to 100 kHz or less. This was far smaller than the transition linewidth ( $\Gamma = 2\pi \times 5$  MHz). The optimal intensities of the probe and pump beams were found to be  $9 \text{ mW/cm}^2$  and  $5 \text{ mW/cm}^2$  respectively, as compared with a saturation intensity of  $1.1 \text{ mW/cm}^2$ . These features were indicative of a strong nonlinear process. Each

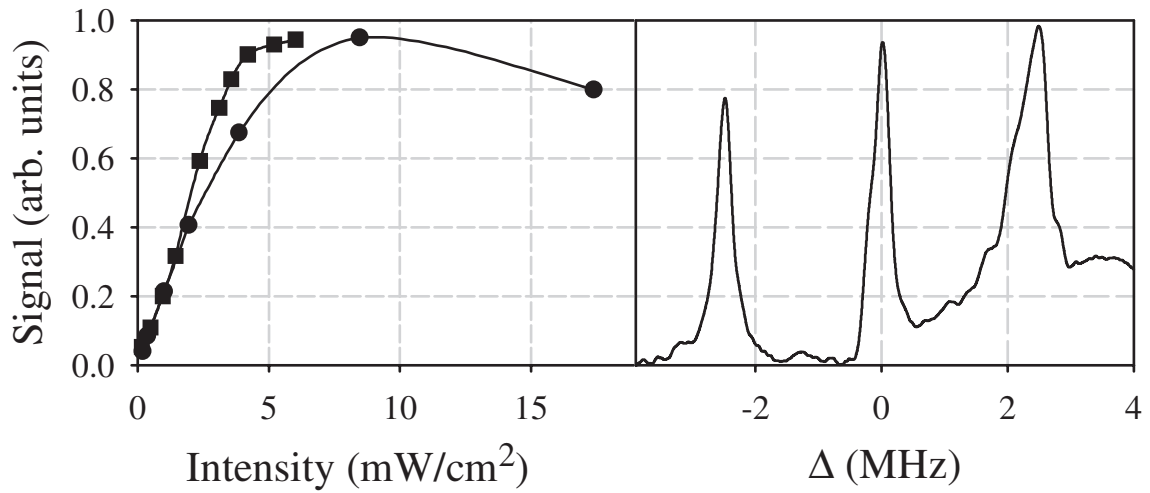


Figure 5.13: (a) Modulation transfer signal size as a function of pump intensity (squares) and probe intensity (circles) using the pump configuration shown in Fig. 5.12. The two data curves were taken at the probe and pump powers which, respectively, gave optimal signal. (b) Typical frequency lineshapes where  $\Delta$  is the pump detuning from the fixed probe frequency. The three peaks come from the correspondence of the probe frequency with the pump carrier and two sidebands. As the detuning becomes positive, one sideband nears resonance, which resulted in excessive noise.



sideband contained 20% of the total power. The probe beams and the pump beam carrier were detuned 6.5 MHz red of the  $6S_{1/2}$ ,  $F = 4 \rightarrow 6P_{3/2}$ ,  $F = 5$  transition. A 2.5 MHz modulation frequency was chosen based on theoretical predictions of maximal signal with a modulation frequency of  $\Gamma/2$  [86]; experimentally this value was optimal as well. The optimum polarizations for the pump and probe beams were  $\sigma+$  and linear respectively.

The pump and probe beams had a kinetic effect on the cold atoms which could be exploited to obtain long interrogation times. Because the beams were retroreflected and red-detuned, they formed a two-dimensional optical molasses. The molasses slowed and stopped atoms returning from the fountain while confining them along the second axis as well. For this geometry, atoms in the  $6S_{1/2}$ ,  $F = 4$  state optically pumped to the  $6S_{1/2}$ ,  $F = 3$  level via off-resonant excitations with a time constant of 4.6 ms. With the addition of a repumping beam, the time constant was extended to 16 ms, here limited by heating of atoms along the unconstrained axis. Alternatively, the motion along all three axes could be constrained by using frequency modulated molasses beams as the pump beams. In this configuration, detection times as long as 50 ms were achieved. However, in situations where there is significant phase noise, such as in a gravimeter, it is not possible to remain centered on a fringe, and this form of balanced detection with FM molasses beams is not suitable. More explicitly, if the signal is not perfectly balanced, thereby rejecting fluctuations in atom number, a different approach must be taken to remove the number fluctuations.

Using the pump configuration shown in Fig. 5.12, a two pulse detection sequence was used in order to measure the total number of atoms as well as the difference signal. First atoms in the  $F = 4$  state were detected in the upper probe beam. These atoms were stopped by a 2-D molasses consisting of the vertically oriented pump beam and one of the horizontally oriented probe beams. Atoms in the  $F = 3$  state continued to fall. After 7 ms the  $F = 3$  atoms were centered in the lower probe beam. A repumper then pumped all atoms to the  $F = 4$  state, and the differential signal was detected. This signal consisted of the difference between the original  $F = 4$  atoms in the upper probe beam and the repumped  $F = 3$  atoms in the lower. The total atom number was inferred from a combination of the signals from the two detections

and then the signal was normalized to remove noise from shot-to-shot atom number fluctuations (see section 6.2.1 for an explicit description of this). The difference signal is used, rather than the sum, in order to remove any residual noise component from the absorption of the probe lasers by the background Cs atoms.

### 5.7.3 Detection system performance

As a demonstration of the power of the detection system, shot noise limited detection of population differences was achieved with this normalization using  $10^6$  atoms in a microwave clock experiment. Two  $10\ \mu\text{s}$  spaced microwave  $\pi/2$  pulses drove a Ramsey clock sequence [8]. The geometry of this experiment is similar to the gradiometer measurement, but no Raman beams were used for the interferometer. The  $F = 4$  population level and total number of atoms were detected following the fountain with the two pulse sequence described in the previous section. Scanning the phase of the final microwave  $\pi/2$  pulse generated Ramsey fringes (see Fig. 5.14a). A sinusoidal least-squares fit was performed on the normalized fringe. Scale factors for the detection signals were fit to account for small differences in detection efficiencies for the two states. The fit gave a SNR of 1000:1, consistent with the shot noise limit of  $N_{at}^{1/2}$ .

To study further the sensitivity of this detection method a study was performed of detection noise as a function of atom number. For this study, the MOTs were launched in the  $F = 3$ ,  $m_F = 0$  state in a 320 ms atomic fountain, again similarly to the preparation for the gradient measurements. A microwave  $\pi/2$  pulse was used to divide the population equally between the  $F = 3$  and  $F = 4$ ,  $m_F = 0$  states. With the molasses beams modulated as pump beams, the balanced signal was integrated for 33 ms following the fountain. The long integration time was used to minimize the effects of photon shot-noise when detecting small ( $< 10^4$ ) numbers of atoms. With equal populations in the balanced mode a null signal was produced that was free of laser induced noise. The total atom number was varied by varying the efficiency of the pulses in the selection sequence of section 5.5. The SNR was computed for each atom number by comparing the standard deviation of the balanced signal with the

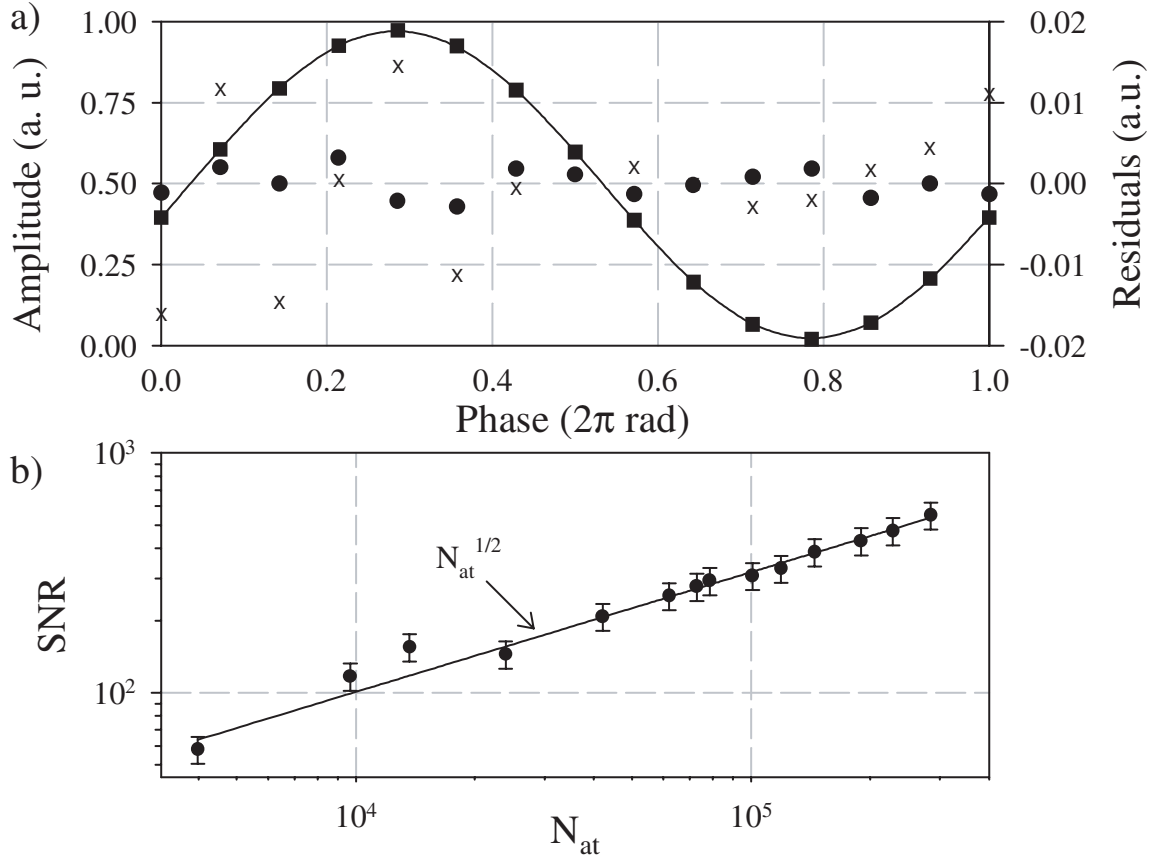


Figure 5.14: a) Normalized Ramsey fringe (squares) showing 1000:1 SNR. The solid line is a least squares fit. The residuals are from the fit for the data before (X) and after (•) normalization. b) SNR detected in balanced mode for various atom numbers  $N_{at}$  using FM molasses beams as pump beams. The solid line represents the shot noise limit of  $N_{at}^{1/2}$ , in good agreement with the measured SNRs.

peak signal from all the atoms in one state (*i.e.* the maximally imbalanced signal). The measured SNRs agree well with shot noise limited detection ( $N_{\text{at}}^{1/2}$ ) as shown in Fig. 5.14b.

The peak performance of the modulation transfer method was exhibited with an ensemble of  $\sim 10^7$  atoms, launched in the  $F = 4$  state, but not state selected into the  $m_F = 0$  sub-level. Normalizing the ensemble by detecting it with the two pulse sequence yielded an SNR of 2350:1. Without normalization, the shot-to-shot atom number fluctuations limited the SNR to 200:1.

Common-mode noise rejection ratios were measured for both laser amplitude and frequency noise as well as atom number fluctuations by deliberately inducing these noise sources. Balanced detection rejected these noise sources at the 40 dB, 24 dB and 27 dB levels respectively. The laser amplitude noise rejection of 40 dB (dc - 10 MHz) was limited only by the balancing of the balanced photodiode pair. Frequency noise rejection was characterized by driving high frequency noise at 2.5 kHz during a shortened detection pulse<sup>8</sup> as well as by making low frequency changes to the pump and probe beams together in the balanced detection. Both tests showed similar results. With this noise rejection, we inferred that atom shot noise limited performance could be achieved for atom numbers up to  $10^{10}$  atoms, corresponding to an inferred maximum achievable SNR of  $10^5$ :1. On the other hand, photon shot noise placed a lower limit on the operating range of  $\sim 10^3$  detected atoms. Below this atom number, the photon shot noise began to become larger than the atom shot noise limit.

#### 5.7.4 Noise analysis

The amplitude of the modulated absorption signal at the photodiode is about 0.8 pW per atom. The detection photodiodes have noise-equivalent powers corresponding to a 60 atom detection sensitivity in the 4.6 ms measurement window. The digital voltmeters that acquire the signal from the photodiodes are only slightly noisier with a noise floor corresponding to a 100 atom minimum detectable signal. The largest

---

<sup>8</sup>The detection pulse was shortened to avoid averaging the high frequency noise.

contribution to the intrinsic noise comes from the detection light itself. Because absorption detection is used and the absorption is a small component of the total light, there is a substantial amount of unabsorbed light,  $> 99\%$ , striking the detector. Shot noise on the number of photons incident on the detector during the integration window is the leading intrinsic noise source. The shot noise power is 0.25 nW, resulting in a minimum detectable signal of  $\sim 300$  atoms. This noise dominates the technical noise sources, and it is this noise component that begins to limit the SNR for low atom numbers.

There is also a noise component of similar size due to a small number of atoms in undesired states which survive the state preparation. Slight changes in laser frequency and selection pulse efficiency during the state preparation cause this number to fluctuate. However, this background noise is common between the two chambers and is also suppressed by the balanced detection method.

To summarize, the noise of the detection system allows detection of transition probability following the interferometers at the atom shot-noise limit when there are at least  $\sim 10^5$  atoms contributing to the signal. Below this level, the SNR decreases linearly with number of atoms detected. These noise limits are discussed in the context of the overall instrument sensitivity in section 6.3.

## 5.8 Vibration isolation subsystem

At the most sensitive gradiometer operation, vibration phase noise is large<sup>9</sup>, and a data analysis method capable of extracting phase information in the presence of large common-mode phase noise must be employed (see section 6.2). However, in order to verify the validity of such an algorithm, a vibration isolation system was constructed to remove most of the vibration-induced phase noise from the interference fringes. With this reduction in phase noise, a straightforward least squares fit algorithm also can be used to reduce the data and compare analysis methods.

---

<sup>9</sup>A moderately quiet unfloated optical table in a “standard” lab has a residual vibration level of up to  $10^{-5}$  g which can amount to phase noise of  $\pi$  rad.

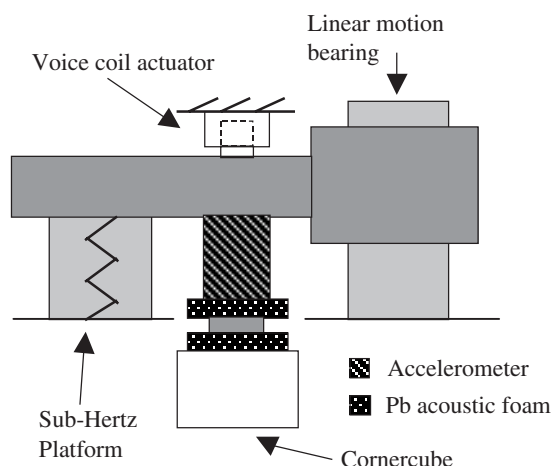


Figure 5.15: A diagram of the vibration isolation system featuring active and passive elements to isolate the suspended cornercube.

### 5.8.1 Mechanical design

The primary object in the instrument that must be isolated from vibrations is the Raman beam corner cube. All other optics are positioned so that any vibrations Doppler shift the two Raman beams in a common way, and the Raman difference frequency remains unchanged. The Raman beam corner cube retroreflector is mounted on a Newport sub-Hertz platform (SHP) which provides the principal vibration isolation (see Fig. 5.8.1). The SHP is guided by a linear air bearing (New Way S4010002) along the vertical axis. The SHP provides isolation in the range of 0.5 Hz - 40 Hz. An accelerometer (Teledyne Geotech S-510) is mounted on the SHP to monitor platform accelerations. The corner cube is attached to the platform by a stack of two pieces of 1 in. thick lead filled acoustic foam separated by a 0.5 in. thick sheet of aluminum. The double stack of acoustic foam reduces vibrations of 30 Hz and higher by more than 20 dB. A linear voice coil actuator provides active feedback to the SHP. Additionally, the voice coil can be used to drive platform accelerations; this shake-testing is the subject of section 6.5.1. The entire apparatus is mounted above the two chambers, and the Raman beams propagate from below the chamber and reflect from the cornercube from below (see Fig. 5.8).

### 5.8.2 DSP servo system

The active servo system for the SHP platform is now described. The active feedback loop starts with the accelerometer to monitor vibrations. The accelerometer output is processed by a DSP (Spectrum Signal Indy TMS320C32), which is used to filter digitally the accelerometer input (as described below) and generate the feedback error signal. The feedback signal, after being buffered by a voltage amplifier, closes the feedback loop by driving the voice coil mounted between the SHP and the platform support. We apply the following digital filters in processing the accelerometer signal. First, a lag filter with a bandwidth of 1 Hz to 80 Hz rolls off the feedback below the accelerometer's 100 Hz high frequency cut-off. Next, a second lag filter with identical bandwidth is used to make the gain roll-off second order. Finally, two lead filters are applied to keep the system from oscillating at low frequency near the closed-loop SHP resonance of 0.03 Hz, which is also close to the internal high pass frequency of the accelerometer. The two lead filters have bandwidths of 38 mHz - 200 Hz and 380 mHz - 200 Hz respectively. The total gain of all four filters is 1600. This work is similar in concept to that reported in Ref. [92]. The transfer functions of the SHP-voice coil system as well as the filter transfer functions and discrete implementation of the digital loops are contained in Appendix B.

Using this servo, the vibrations were reduced to near the noise floor of the accelerometer ( $10^{-8}$  g/Hz<sup>1/2</sup>) over a bandwidth of 40 mHz - 25 Hz. Higher frequencies are passively attenuated by the acoustic foam. The power spectral density of the vibrations is plotted in Fig. 5.16. With the addition of the vibration isolation system, phase noise from accelerations of the corner cube is reduced to less than 1 rad, and least squares sinusoidal fits may be performed on the fringes for the longest interrogation times.

## 5.9 Microwave generation

The generation and delivery of the 9.2 GHz microwave field is briefly described here. The microwave field is coupled to the atoms through rf horns attached to viewports

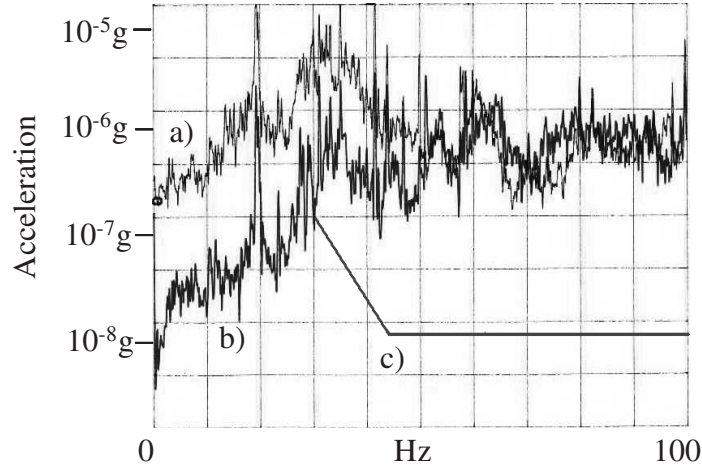


Figure 5.16: Power spectral density of the vibrations of the platform, as measured by the on-board accelerometer. a) Freely floated platform. b) Actively servoed platform. c) Predicted level of vibration for the cornercube mounted on the acoustic foam.

on the MOT chambers. The microwave frequency is tied to a 10 MHz reference, temperature stabilized, master crystal oscillator (Oscilloquartz OCXO, stability of  $1.4 \times 10^{-13}$  in 1 s). The reference oscillator drives a 100 MHz phase locked oscillator (PLO, Wenzel 500-0732) which is the input to a Microlambda (MLPE 1162) 9.2 GHz PLO. The rf is mixed in a single sideband mixer with an  $\sim 7.4$  MHz signal from an AWG which is also phase locked to the reference oscillator. The AWG is used to scan the rf frequency and phase. The mixer output is amplified up to  $\sim 1$  W and sent to the horns. The rf power is controlled by the AWG output, and the relative power to the two chambers can be adjusted with appropriate attenuation in the two paths. Coupling the microwaves into the chambers by simply directing the horns towards the MOTs is not an optimal approach. The microwave field is complex in the chamber due to reflections from the chamber. Across the cloud of atoms, there is often a significant phase and amplitude variation in the microwave field. However, the solution to this, construction of an optimized cavity, is hardly optimal either, as it would restrict optical access to the atoms.

A microwave  $\pi/2 - \pi/2$  clock experiment [8] is performed as a diagnostic to check the phase noise performance of our oscillators and the noise performance of our detection system. Detection of microwave clock fringes with 1000:1 SNR was shown using



the normalized detection as described in section 5.7.3 [91]. This SNR is at the atom shot noise limit for the fountain with no velocity selection ( $\sim 10^6$  atoms/shot).

# Chapter 6

## Results

This chapter first details the initial results of the gradiometer, a measurement of the Earth's gravity gradient, in section 6.1. Following the implementation of the atomic fountain and the sensitive detection scheme described in section 5.7, new levels of sensitivity were achieved [93]. With this enhanced sensitivity, considerable effort was devoted to the problem of extracting phase information from the two coupled interference fringes, particularly in the presence of large amounts of common-mode, vibration-induced phase noise. A thorough discussion of the data analysis routines employed is given in section 6.2. Using these data extraction methods an analysis of the sensitivity and accuracy is performed in section 6.3 and 6.4 respectively. Finally, section 6.5 details studies of the gradiometer in the presence of a noisy reference platform.

### 6.1 Proof-of-principle results

The initial measurement performed was a measurement of the Earth's gravitational gradient over a 1.1 m baseline [19]. In order to verify that the phase difference between interference fringes was indeed due to a gravity gradient, the change in the Earth's field between the two accelerometers was measured. In this initial experiment, the MOTs were constructed out of three pairs of retroreflected beams. With this configuration launching the atoms was not possible, so the total interaction time was

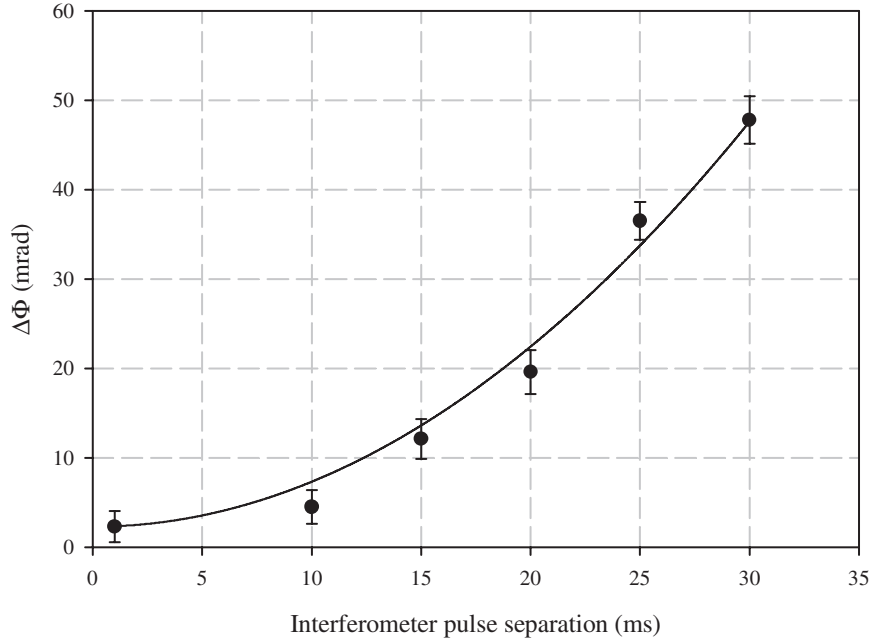


Figure 6.1: Proof-of-principle measurement of the Earth’s gravity gradient over 1.1 m, prior to many sensitivity enhancements. The points are the data, and the solid line is a quadratic least squares fit in good agreement with the expected Earth gradient.

limited to about 60 ms, after which the atoms fell out of view of the viewports in the vacuum chamber. In order to measure the Earth’s gradient, the interferometer pulse spacing  $T$  was increased. The gravitationally accrued phase shift from the Earth’s gravity gradient as a function of increasing interrogation time  $T$  is shown in Fig. 6.1. Each data point in Fig. 6.1 represents six hours of data collection. In order to remove systematic shifts, the Raman propagation was reversed as described in section 5.6.3 every three hours by manually rotating the Raman beam polarizations with a half-wave plate.

The data are fit to  $\Delta\phi = k_{\text{eff}} \delta a T^2$  for the differential acceleration  $\delta a$ . In this initial configuration, the Earth’s gravity gradient was measured to be  $3370 \pm 175$  E, consistent with the expected value of 3080 E assuming an inverse square scaling law for  $g$  and ignoring any gradients from near-field inhomogeneities. This measurement established the ability to detect gravity gradients even in this highly limited configuration. The next generation of the experiment then took full advantage of the techniques and

experimental apparatus described in Chapter 5 to vastly improve the sensitivity and stability [93].

## 6.2 Signal extraction

Equally important to the experimental apparatus and the data collection itself is the signal extraction technique. For this reason different methods of extracting phase information from the interference fringes were investigated. In order to appreciate the virtues of the best method, which is based on fitting ellipses to the data, all methods investigated are described here. The simplest of these methods is nonlinear least squares sine fitting. This method is the least applicable to noisy data however. A Gaussian elimination routine is a simple method for dealing with data with high phase noise, but it can give misleading results if care is not taken and is only suitable within a small phase range. Fitting the data using a circle fitting method offers the substantial benefit that it is utterly immune to common-mode phase noise, but the circle method gives a systematic shift for large relative phase shifts. The most robust fitting method is a method based on fitting ellipses to the data to extract the gradiometer phase, and this is the only fitting method that performs well with nearly all interferometric phases. The methodology is described in this section, and the experimental figures are given in section 6.3.

### 6.2.1 Normalization

Before describing the phase extraction methods, the normalization procedure used in all methods is detailed here. The loading of a vapor cell MOT is a stochastic process, and even a MOT constructed from highly stable laser beams and magnetic fields will have number fluctuations. In order to eliminate noise from this fluctuating number of atoms contributing to the interferometer from shot-to-shot, a normalization is performed for each interferometer signal based on the two-pulse detection sequence described in section 5.7. The goal of the normalization is primarily to remove atom number fluctuations, but also to remove any residual noise from the detection process

itself (such as from laser frequency and intensity drifts). After each interferometer cycle (which represents one gradient measurement) two samples are acquired in each accelerometer: signals proportional to the  $F = 4$  population and to the differential population, *i.e.* proportional to the number of atoms in  $F = 4$  minus the number of atoms in  $F = 3$ . The two samples are combined to infer the total number of atoms present in the interferometer during each experimental cycle. Let  $S_1^{(1)}$  and  $S_1^{(2)}$  be the signals from the two detection pulses in the first chamber<sup>1</sup>.  $S_1^{(1)}$  is proportional to the number of atoms in the  $F = 4$  state, and  $S_1^{(2)}$  is proportional to the number of atoms in the  $F = 4$  state minus the number in the  $F = 3$  state, with constants modifying each state due to small inefficiencies in the detection. The quantity  $N \propto S_1^{(1)} - cS_1^{(2)}$  then is proportional to the total number of atoms detected in both states, where  $c$  is a constant containing the detection inefficiencies. Dividing the  $F = 4$  interference fringe produces a normalized signal that is proportional to the transition probability only:

$$S_1 = \frac{S_1^{(1)}}{N} \propto \frac{S_1^{(1)}}{S_1^{(1)} - cS_1^{(2)}}. \quad (6.1)$$

Performing this normalization removes number fluctuations from the  $F = 4$  interference fringe<sup>2</sup>.

### 6.2.2 Interference fringe fitting

As described in section 5.6.5, the phase of the final interferometer pulse is scanned electronically. The most straightforward method of extracting gravity gradient information is to determine the gravitationally induced phase shifts in each atom ensemble by performing least squares sinusoidal fits on the observed interference fringes for each chamber. This fitting is possible when vibration-induced phase noise is approximately less than 1 rad. The gravity gradient is obtained by subtracting the two phase shifts

---

<sup>1</sup>The same normalization procedure is applied to the second chamber, but with slightly adjusted proportionality constants.

<sup>2</sup>It is important to note that shot-to-shot number fluctuations are not equivalent to shot noise. Shot noise arises from the statistics of projecting the superposition state of the interferometer onto the two basis states during the detection. Shot-to-shot number fluctuations primarily come from noise on the trapping lasers.

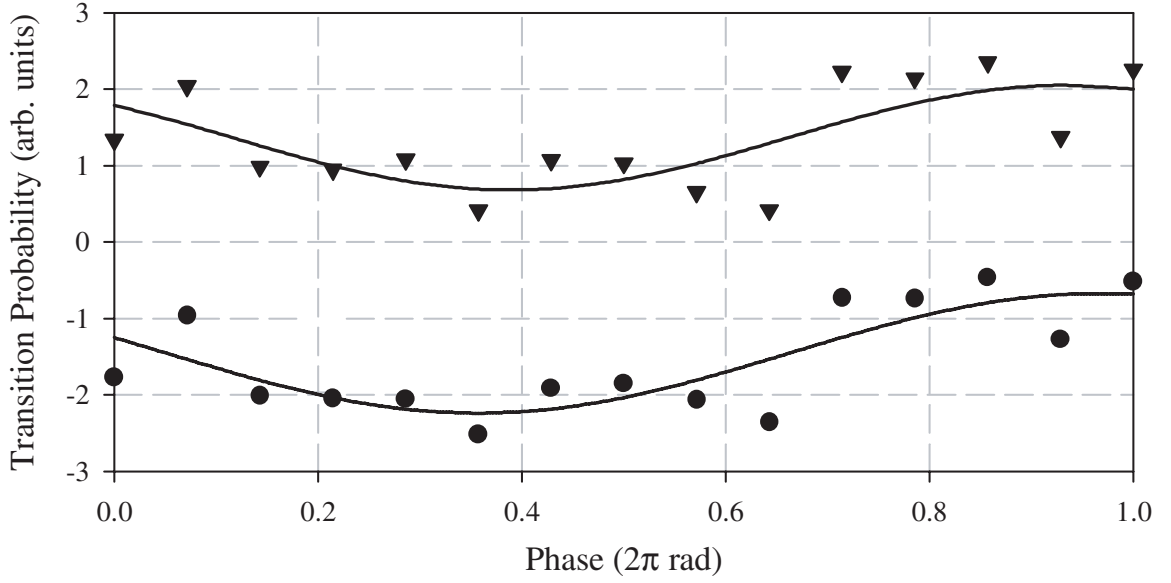


Figure 6.2: Sinusoidal least squares fits (solid lines) to typical  $T = 157$  ms interference fringes. The phase shift between the upper and lower interferometer fringes (circles and triangles respectively) of  $\sim \pi/2$  rad due to the Earth’s gravity gradient has been removed using the magnetic phase shifting of section 6.2.3. Note the high degree of common-mode noise.

from each other. Vibrational phase noise and local oscillator phase noise cause the phase extracted by the sine fits to be shifted. However, these noise sources couple to the two accelerometers in a common-mode way. This common-mode behavior results in the two sinusoidal fits being shifted by an identical amount, and any effect of common-mode noise is cancelled in the subtraction used to obtain the gravity gradient. We study the statistics of the resulting phase differences under static gravity gradient conditions to estimate instrument noise. This fitting method is only effective at removing common-mode phase noise if the two fringes are in phase with each other. If they are out of phase, then the phase noise will not pull the fits in a common way, and the noise is not removed in the subtraction of the fitted phases. To remove number fluctuations, each fringe is normalized as in section 6.2.1 first. Typical interference fringes fit in this way are displayed in Fig. 6.2.

The distribution of the residual noise contains outlying points. Eliminating these outlying points increases the SNR by up to a factor of six. The reduction of the

number of points is incorporated into the data collection time in determining the sensitivity. The source of this noise component is still unclear.

The ratio of the interference fringe amplitude to the standard deviation of the phase difference distributions determines the instrument SNR. The side of a fringe, *i.e.* the linear slope of a sine wave, is most sensitive to phase shifts, with a sensitivity given by  $\delta\phi = 1/\text{SNR}$ . For gravitationally induced phase shifts, the sensitivity to a change in the gravitational acceleration is  $\delta g = \delta\phi / (2k_{\text{eff}}T^2)t^{1/2}$ , where  $t$  is the data acquisition time to achieve the uncertainty  $\delta\phi$ . Dividing by the chamber separation determines the sensitivity to gradients. In high phase noise regimes, the vibration isolation system must be used to limit the vibrations so fringes can be fit. Use of the isolation system defeats the point of gradiometry; therefore other analysis methods were sought.

### 6.2.3 Magnetic phase shifting

Good common-mode noise suppression by fitting fringes requires that the lower and upper chamber fringes be acquired in phase. However, the Earth's gravity gradient of  $\sim 3000 \text{ E}$  will cause a relative phase shift of  $\sim 1.5 \text{ rad}$  between the two chambers. In order to accommodate this shift, a bias magnetic field is pulsed on for 67 ms in the lower chamber during the atom interferometer. This field pulse causes a phase shift due to the second-order Zeeman effect. The amplitude of this pulse is chosen to produce a shift which compensates the shift due to the gravity gradient, allowing both fringes to be acquired in phase.

A quantitative study of the effectiveness of common-mode noise suppression as a function of the phase alignment of the interferometer fringes was performed. Fig. 6.3 shows a comparison of the predicted dependence of the noise on the relative phase between fringes with experimental SNR data. For simplicity, we scanned the relative phase between pulses simply by changing the interrogation time  $T$ . (For this study, we disabled the magnetic phase shifter and worked with relatively short interrogation times.) The data shown in Fig. 6.3 is the SNR of the phase difference between the two

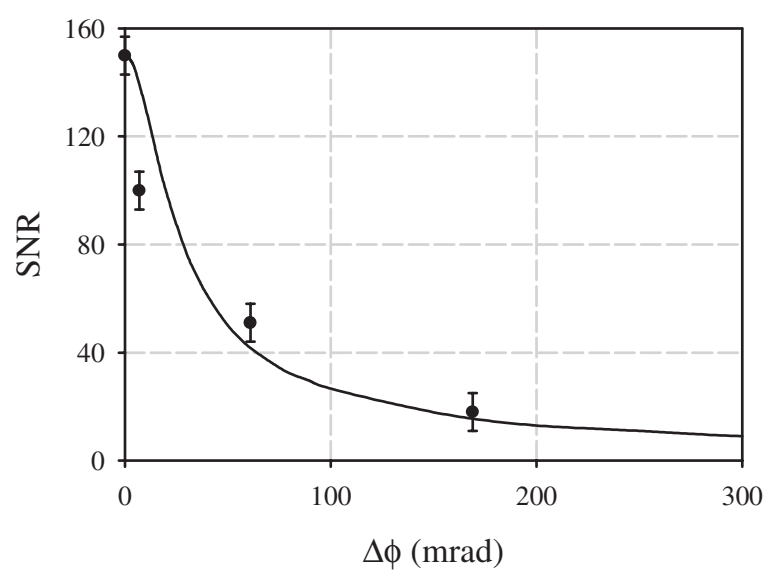


Figure 6.3: Using sinusoidal least squares fits, the decrease in the gradiometer SNR is shown due to a phase mismatch induced by the Earth's gravity gradient. The phase shift  $\Delta\phi$  is the gradient phase shift from increasing the interferometer time  $T$  ( $\Delta\phi \propto T^2$ ). The solid line is a theory based on the noise from two mismatched sine waves in quadrature with photon shot noise from the detection system.



fringes obtained by performing least squares fits as described above on a set of interference fringes. The prediction is the simulated SNR of the phase difference between two phase-mismatched sine functions with phase noise added. The predicted SNR is added in quadrature with uncorrelated detection noise in order to compare the simulation with experimental data in this curve. As shown, the data is in good agreement with the theory, demonstrating the need for the magnetic phase shifting pulse with this analysis routine.

One concern is that by adding an extra bias field, absolute accuracy and long-term stability will be sacrificed. To study this, the stability of the bias field used in the magnetic shifter has also been studied. High frequency noise on this bias field could lead to extra phase noise on the gravity gradient signals as well. This noise has been investigated by applying a bias pulse in a microwave clock  $\pi/2$ - $\pi/2$  experiment and comparing the SNR for a weak pulse (phase shift  $\sim 1.2$  rad) and a strong field pulse (phase shift  $\sim 67$  rad). For the large phase shift, no extra phase noise or drift is seen at a fractional uncertainty in the phase of less than  $3 \times 10^{-6}$ . This implies that for a 1 rad shift, the bias pulse contributes noise at a level below  $8 \times 10^{-13}g$ . However, it is certain that at some level below this, the stability level is not sufficient for making ultra-precise measurements. For such measurements, adding possible systematics like a magnetic field is undesirable.

#### 6.2.4 Gaussian elimination reduction

In the case where phase noise is greater than 1 rad, the noise renders it impossible to characterize instrument noise using the least squares method described above. In the most sensitive modes of operation, the vibrations of the reference platform induced phase noise much larger than this level. A different analysis technique can be performed in this regime, using a point-by-point analysis. After collection of the gradiometer data, the normalization algorithm is applied to remove common amplitude fluctuations in each chamber. After removing amplitude noise, a cross-chamber normalization is performed to reject phase noise that is primarily vibration-induced.

The details of this noise analysis procedure are as follows. The two interferometer fringes are first normalized using the procedure of section 6.2.1. To remove common phase noise between the two chambers, a series of experimental cycles is taken (typically 16), and a least squares minimization (via Gaussian elimination) is performed on the quantity  $(S_1 - \alpha S_2 - \beta)^2$  where  $S_1$  and  $S_2$  are the shot-by-shot normalized  $F = 4$  population levels from the two interferometers. The fit constants  $\alpha$  and  $\beta$  are used to compensate for possible differences in interference contrast between the two accelerometers. The rationale behind this analysis method is that in the limit of small relative phase shift  $\Delta\phi$ , the difference between the two fringes is:

$$\sin(\phi) - \sin(\phi + \Delta\phi) \simeq \Delta\phi \cos(\phi). \quad (6.2)$$

Even more appealing, at the zero crossing of the sine waves when  $\phi = 0$  or  $\pi$ , this difference reduces to just  $\Delta\phi$ . Thus with this method, the phase shift is directly proportional to the offset  $\beta$  used to perform the Gaussian elimination. This method is ideally employed not by scanning fringes, but by acquiring data only on the side of a fringe (which is difficult to do in a high phase noise environment).

The residuals of the Gaussian elimination procedure are used to estimate instrument noise, as show in Fig. 6.4. Again, this distribution is non-Gaussian, and outlying points are discarded to obtain SNR and short-term sensitivity estimates. However, the Gaussian elimination routine is an unsatisfying data reduction method. If the relative efficiencies of the detection pulses changes, it is possible to be misled by the data analysis. Because of the nature of the signal acquisition and the subtraction, if care is not taken with the analysis, it is possible to obtain artificially small residuals, producing an erroneously high SNR. Finally it requires the addition of a bias field (as described in section 6.2.3) to operate at a nearly perfectly in-phase condition to obtain good common-mode suppression between the two chambers.

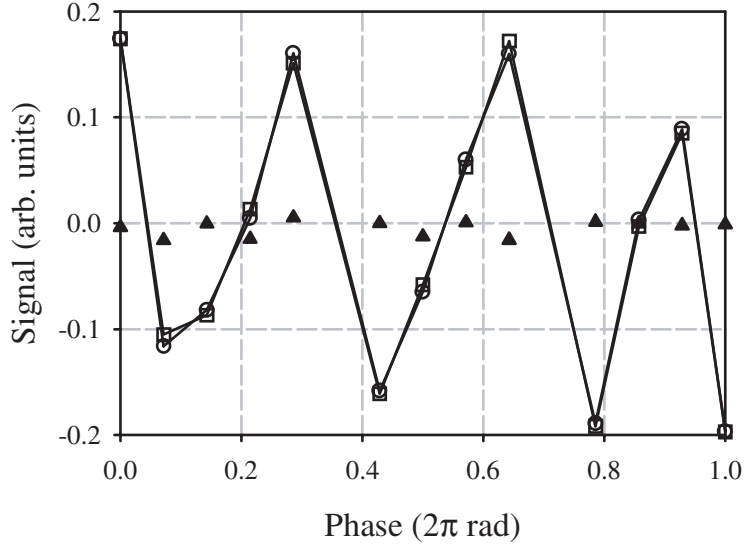


Figure 6.4: Gradiometer interference fringes with  $T = 157.5$  ms. Squares and circles represent the normalized upper and lower chamber fringes respectively, after compensating for contrast differences between the chambers. Triangles show the lower chamber residual signals after reducing the data using the Gaussian elimination method section 6.2.4.

### 6.2.5 Circle fitting

An innovative method for extracting the phase from the gradiometer relies on the trigonometric relationship between two coupled sinusoids<sup>3</sup>. If the data  $S_1$  and  $S_2$  are two sinusoids,  $\sin(\theta)$  and  $\cos(\theta + \Delta\phi)$ , out of phase by approximately  $\pi/2$  rad, *i.e.*  $\Delta\phi$  is small, then the data lies approximately on a circle of radius  $r$  when plotted as the interference fringe for one accelerometer versus the other. The virtue of this method is that it is totally immune to common-mode phase noise; the data points always lie on the circle, no matter what the phase noise is, as long as it is common to both interferometers. The radius of the circle is defined as:

$$r^2 \equiv S_1^2 + S_2^2 = \sin^2(\theta) + \cos^2(\theta + \Delta\phi) \simeq 1. \quad (6.3)$$

---

<sup>3</sup>This method is applicable for any system of coupled sinusoids with an appropriate phase relationship of  $\sim \pi/2$  rad.

Simplifying and rearranging this equation leads to:

$$r^2 - 1 = \sin(4\theta + 2\Delta\phi) \sin(\Delta\phi). \quad (6.4)$$

Experimentally, the angle  $\theta$  is extracted for each point using the relationship:

$$\theta' = \tan^{-1} \left( \frac{S_2}{S_1} \right), \quad (6.5)$$

where  $\theta' = 2\theta$  due to the range of  $\tan^{-1}$ . It is then straightforward to extract the phase from equation 6.4, by either performing a least squares fit to the function

$$\Delta\phi = \sin^{-1} \left( \frac{r^2 - 1}{\sin(2\theta')} \right) \quad (6.6)$$

or by using a computationally faster Fourier analysis<sup>4</sup> by multiplying both sides of equation 6.4 by  $\sin(2\theta')$  and summing over all  $\theta'$ :

$$\Delta\phi = \frac{\sum_{\theta'} (r^2 - 1) \sin(2\theta')}{\sum_{\theta'} \sin^2(2\theta')}. \quad (6.7)$$

The key approximation in this approach is  $\sin(4\theta + 2\Delta\phi) \simeq \sin(4\theta)$ , which is only true in the limit of small  $\Delta\phi$ .

To summarize, in the limit of two sinusoids out of phase by nearly  $\pi/2$  rad, the data lies close to a circle when plotted as one sinusoid versus the other. The deviations from a perfect circle are due to slight phase deviations from  $\pi/2$  and are sensitive to small phase shifts. Fitting these deviations allows for extraction of the phase difference between the chambers. Before fitting, the data is normalized using the two detection pulses as described in section 6.2.1. Then a circle is fit to the data to normalize it to the unit circle; this fit is performed merely to adjust the scaling and offset parameters for each fringe. For the typical parameters in this experiment the gravity gradient of the Earth conveniently causes a shift of  $\sim \pi/2$  rad between the two

---

<sup>4</sup>The Fourier approach only works in the limit of a large number of points that sample uniformly over the circle.

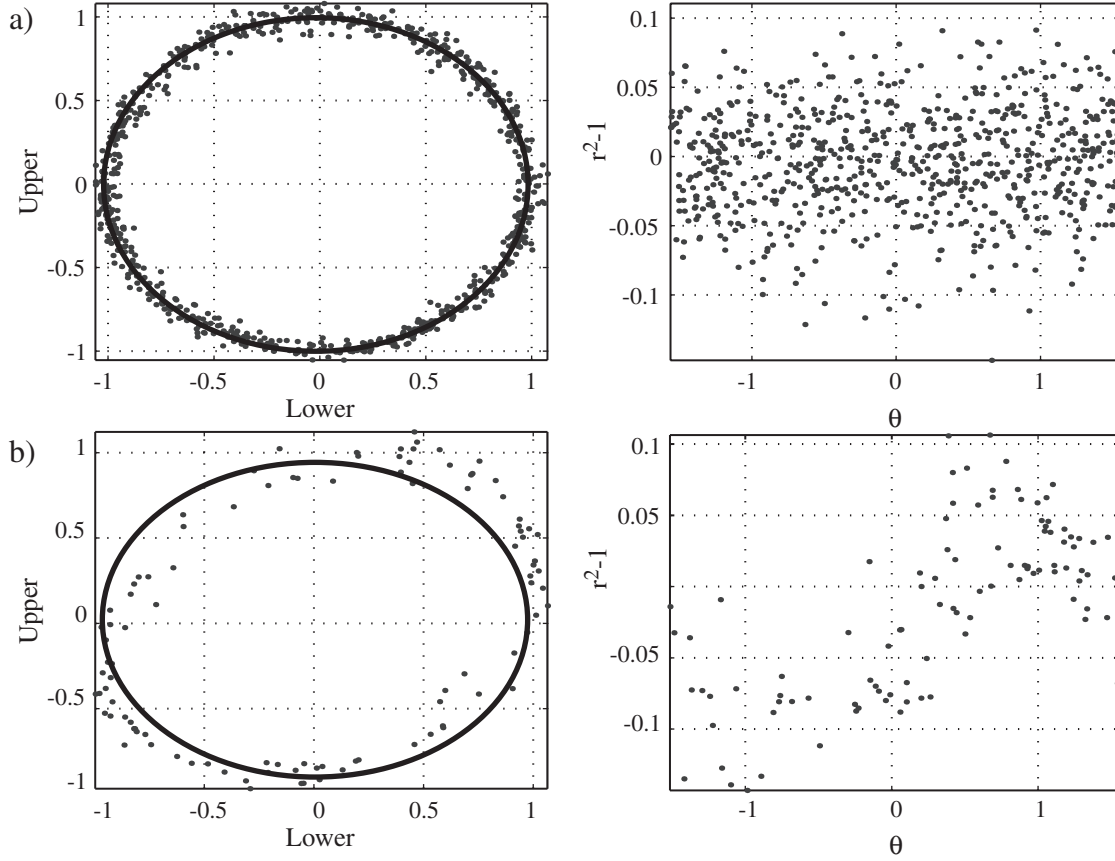


Figure 6.5: Normalized data plotted as upper chamber versus lower lower. The solid line is a least squares fit of a circle, and the  $r^2 - 1$  deviations from the circle are plotted in the adjacent graph. a)  $\Delta\phi \simeq 0$  rad. b)  $\Delta\phi \simeq 0.2$  rad.

accelerometers, and the data are already perfectly matched for this method. Fig. 6.5 shows typical data analyzed using the circle method. The phase uncertainty of the data is characterized two ways. First, the residuals of the fit to the deviations from the circle are directly equal to the uncertainty in the fit for small phase shifts  $\Delta\phi$ . The second method is to divide a larger segment of data into smaller bins, extract a phase from each bin, and calculate the variance of the binned phases. These two methods are in good agreement with each other.

There are several difficult aspects to the circle method. One of the major problems is that the small  $\Delta\phi$  approximation breaks down rapidly. This approximation tends

to cause the phase to be underestimated. The underestimation factor was characterized using simulations and was determined to be a constant 23% low in the range 1 mrad - 500 mrad. Above  $\Delta\phi = 500$  mrad, the circle fitting method breaks down entirely. The second major problem is that the fit is extremely sensitive to the data being normalized to exactly the unit circle centered at the origin. Even with the fit normalizing the data to the unit circle, drifts in the amplitude or offset of the interference fringes can lead to systematic shifts in the phase obtained by the circle fitting method. Finally, if the relative phase between the accelerometers is not nearly  $\pi/2$ , then a magnetic bias pulse must be applied as described in section 6.2.3 in order for this phase extraction method to be applicable.

### 6.2.6 Ellipse fitting

Because of the difficulties involved with the circle fitting method of section 6.2.5, a method to fit directly the data and to extract the phase was sought. A related method based of fitting ellipses to the data instead of circles was implemented. After normalization to remove number fluctuations, the data forms an ellipse when plotted as one interference fringe versus the other. This is generally true and is not dependent on the relative phase of the interference fringes being a particular value. By fitting an ellipse to the raw data, the phase can be directly extracted with no need for normalization. The phase is related to the eccentricity and the rotation angle of the ellipse.

A brief derivation of the ellipse fitting method is now given. The two interference fringes can be written:

$$x(\phi) = A\sin(\phi) + C \tag{6.8}$$

$$y(\phi) = B\sin(\phi + \Delta\phi) + D, \tag{6.9}$$

where  $A$ ,  $B$ ,  $C$ , and  $D$  are the amplitudes and offsets of the two interference fringes  $x$  and  $y$ , and  $\phi$  is the phase of the Raman lasers as they are scanned over an interference fringe. Eliminating  $\phi$  and combining these equations leads, after some manipulation,

to:

$$\begin{aligned} & A^2y^2 - 2AB\cos(\Delta\phi)xy + B^2x^2 + \\ & \left(2ABC\sin(\Delta\phi) - 2A^2D\right)y + \left(2ABD\sin(\Delta\phi) - 2B^2C\right)x + \\ & \left(A^2D^2 + B^2C^2 - A^2B^2\cos^2(\Delta\phi) - 2ABCD\sin(\Delta\phi)\right) = 0. \end{aligned} \quad (6.10)$$

This is the general equation for an ellipse so long as the discriminant is less than zero [94]. For the two interference fringes, the discriminant is  $-4A^2B^2\sin^2(\Delta\phi)$ , which is always less than zero and establishes the applicability of the ellipse approach for the gradiometer data. The important information in Eq. 6.10 lies in the first three terms. By fitting an ellipse to the data, the phase  $\Delta\phi$  can be extracted from the fit parameters. The fit is to the equation:

$$A'y^2 + B'xy + C'x^2 + D'y + E'x + F' = 0, \quad (6.11)$$

where  $A', B', C', D', E'$ , and  $F'$  are the fit parameters. The phase is then given by:

$$\Delta\phi = \cos^{-1} \left( \frac{A'B'}{2\sqrt{A'B'}} \right). \quad (6.12)$$

The method of fitting ellipses to the data is a direct least squares fitting method that uses a constrained minimization technique for computational ease in fitting [95]. The original state vector has five parameters while the transformed state vector (primed coordinates) has six parameters. A direct fit with no constraints is over determined and does not produce a unique solution. To reduce the system to give a unique solution, the ellipse is normalized so that all points lie between zero and one<sup>5</sup>, so that the algebraic distance of the points to the ellipse can be minimized using the constraint that the discriminant is -1. By using this constraint, the fit is both direct, *i.e.* not iterative, specific to ellipses, and the fitted state vector is reduced to five independent parameters again. The fitting reduces to solving a linear eigenvalue

---

<sup>5</sup>The normalization is fundamentally different in the way it effects the fit to the one performed in the circle fitting method.

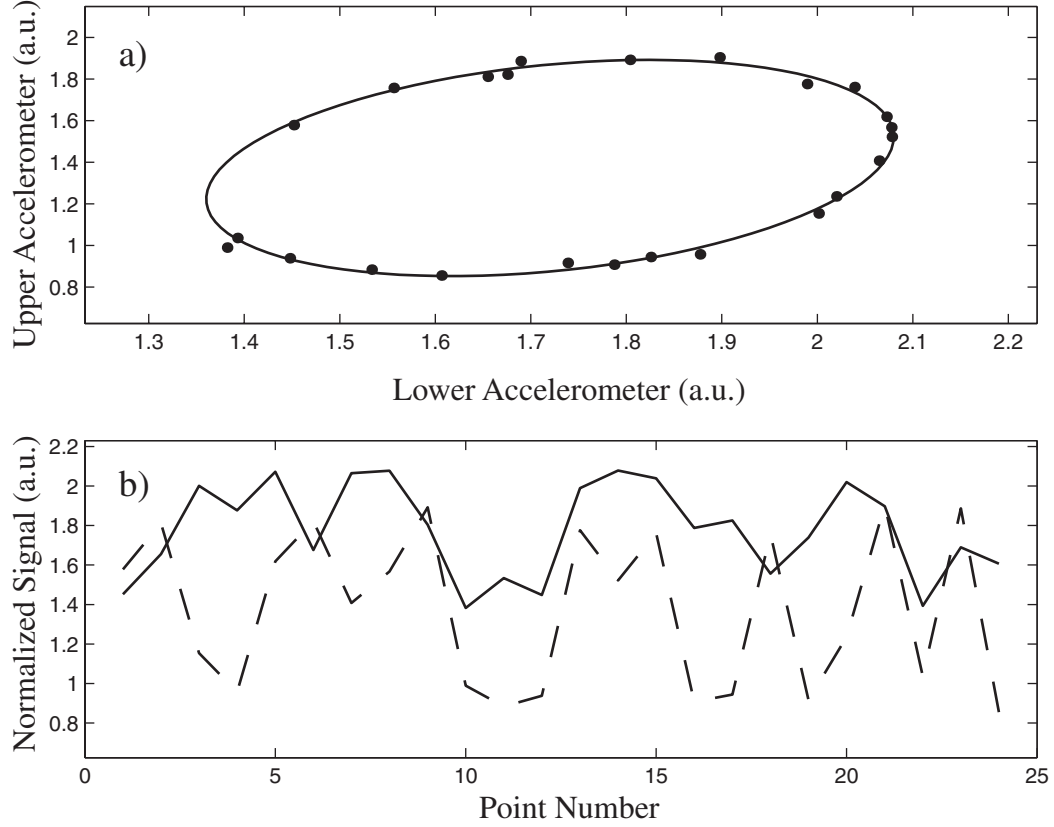


Figure 6.6: Example of data fit with ellipse fitting method. a) Lower accelerometer signal plotted versus upper accelerometer signal. The solid line is the fitted ellipse, and the relative phase information is contained in the eccentricity and rotation angle of the ellipse. b) The raw interference fringes, where the phase is scanned over  $\sim 4\pi$ . The phase noise here is too large for fitting sine waves.

problem, and the single positive eigenvalue uniquely determines the ellipse parameters. This fit method does not rely sensitively on any data normalization or offsets. More importantly, the ellipse fitting method fits accurately at all phases, and does not require a magnetic phase shift to adjust the phase to any specific value. Typical data fit with the ellipse method is displayed in Fig. 6.6.

A test was performed to probe the validity of the phase obtained with the ellipse method. To this end, a controlled phase shift was added to the lower accelerometer using the magnetic pulse described in section 6.2.3. This pulse was stepped through a



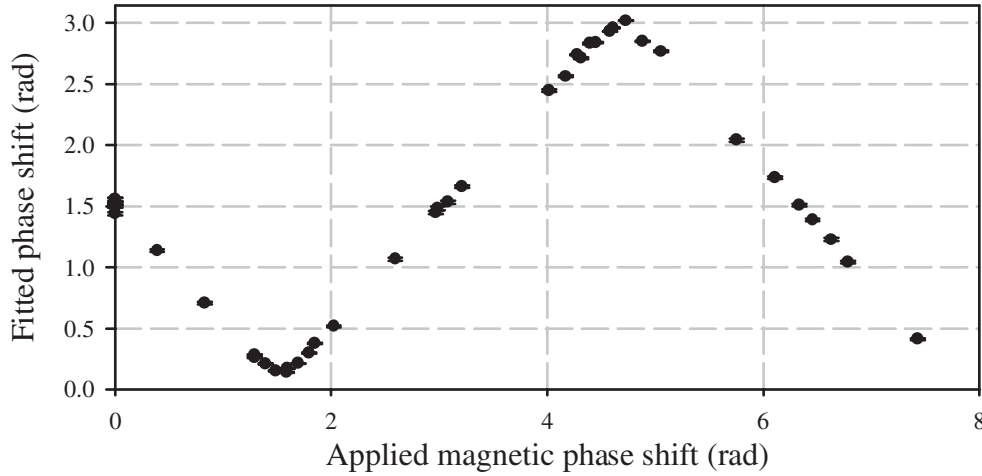


Figure 6.7: Relative phase extracted from  $T = 150$  ms interference fringes using the ellipse fitting routine. The relative phase was varied with a magnetic field pulse.

range of phases and the phase extracted from the ellipse method was compared with the expected phase. The expected phase shift was calibrated by measuring the shift produced by an applied magnetic phase shift (measured using an identical magnetic field pulse in a microwave  $\pi/2 - \pi/2$  clock experiment) and fitting the resultant phase shift using the ellipse method. The results of this calibration are shown in Fig. 6.7. The ellipse fitted phases are a linear function of the expected phases (modulo  $\pi$  and an overall sign due to the  $\cos^{-1}$  in equation 6.12) except for interesting features near the phases 0 and  $\pi$  rad. It appears as if the phase “rolls off” near these values. It is easy to understand why this is. Near 0 and  $\pi$  rad, the two fringes are in phase or completely out of phase, and the ellipse becomes so eccentric it is essentially a line<sup>6</sup>. With a small amount of amplitude noise, the ellipse will never actually become a line, and the ellipse fit will never produce a phase extremely close to these phases for data with noise. In this limited situation, the ellipse fitting method is not appropriate, or a bias magnetic field must be applied to shift away from this area. However over the bulk of the range of phases, the ellipse method performs accurately. One other disadvantage of the ellipse fitting method is that it is sensitive to extreme outliers

---

<sup>6</sup>At exactly these phase values, with no noise, there is a singularity in the fitting routine, but this is a technical detail and not experimentally observable.

outside of the ellipse; these points will strongly pull the fit. However, it is not difficult to reject these wild points.

The phase uncertainty of the phase extracted with this method is calculated using a distance metric. After the eigenvalue problem is solved to obtain the fit constants for equation 6.10, then the data is inserted into the left-hand side of the equation using the fit constants. This value is a distance metric from the fitted ellipse, and the phase uncertainty of the ellipse is related to the square root of the average of the distance metrics over all point in the fit. It is not obvious how the distance metric is specifically related to the phase uncertainty of the fit. To study this, simulations were performed using simulated interference fringes with common phase noise and non-common amplitude noise of up to 10%, which is even larger than the residual noise of the actual data. It was found that the distance metric overestimates the noise by  $\sim 50\%$ , but fits the phase accurately unless the non-common noise is extremely large. Again, to verify this analysis, a large section of data was binned into smaller bins and the variance of the phase extracted from each bin was calculated. These two methods agree well with each other.

### 6.2.7 Summary of data extraction methods

Under the appropriate circumstances, all four data extraction methods are capable of extracting the correct phase shifts. When each extraction technique is employed in its optimal operating environment, all give similar SNRs and long-term drift performance. However, due to the misleading results obtained using the circle fitting method and Gaussian elimination, they are no longer employed. The method of fitting fringes is always unambiguous, but it is not always effective at removing common phase noise, nor is it even able to fit properly in high phase noise situations. The ellipse fitting method is the method of choice in terms of both accuracy and computational speed. It is the only fitting method that can extract phases at nearly all relative phases and is not sensitive to common-mode phase noise at any position. For these reasons it is the predominant fitting method currently employed in the gradiometer. As this method was pioneered towards the end of the work presented herein, much

of the data analysis was performed using the fringe fitting and Gaussian elimination methods.

### 6.3 Sensitivity characterization

Each interference fringe is typically recorded with sixteen consecutive cycles of the experiment. The number of points per scan is kept small to decrease sensitivity to long term drifts in signal amplitude and contrast. The source of such drifts include fluctuations in laser power and drifts in the Cs vapor pressure in the vacuum chambers. The normalized data reduction methods described in section 6.2 are performed on the data. The three high phase noise methods of data extraction all agree well with each other, particularly for short-term sensitivity. The resulting observed SNR is typically 150:1. This corresponds to a differential accelerometer performance of  $4 \times 10^{-8} \text{ m/s}^2/\text{Hz}^{1/2}$ , or  $\sim 4 \times 10^{-9} \text{ g/Hz}^{1/2}$ . Scaling this to a 10 m baseline gives an inferred gradient sensitivity of  $4 \text{ E/Hz}^{1/2}$ . Figs. 6.4, 6.5, and 6.6 all show typical high sensitivity fringes in the upper and lower chamber for a  $T = 150 \text{ ms} - 157.5 \text{ ms}$  interferometer. The fringe contrast is typically  $\sim 33\%$ .

Fig. 6.8 compares interference phase scans with the reference platform rigidly attached to the optical table ( $\sim 10^{-5}g$  acceleration noise) with the reference platform servoed using the vibration isolation system. We can use the data acquired under servoed conditions (*e.g.* Fig. 6.8b) to provide an independent check on the observed SNR, by performing the least-squares fitting analysis detailed in section 6.2.2, and comparing it with the high phase noise analysis methods for data acquired without the servo (*e.g.* Fig. 6.8a). We find that all approaches yield consistent noise estimates when operated optimally. However, as noted above, when the fitting methods are not in their optimal conditions, then inaccuracies can result. The ellipse fitting method is the most suitable method, based on its accuracy, simplicity, and computational speed, for data which does not have egregious outliers, as is the case with the typical gradiometer data.

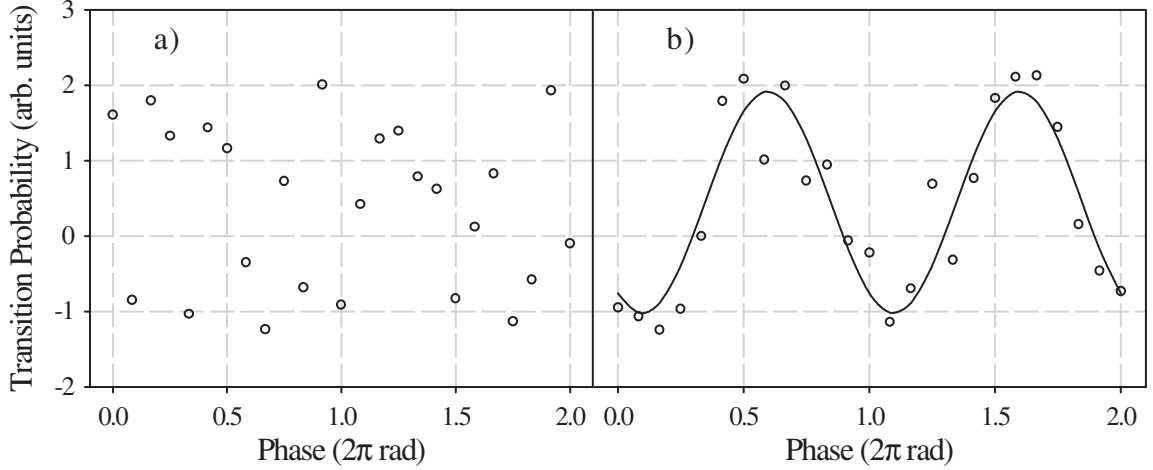


Figure 6.8: Typical interference fringes with  $T = 157.5$  ms. Circles are the raw data points, and the solid line is a sinusoidal least squares fit. (a) Fringe with no vibration isolation, *i.e.* with the corner cube bolted rigidly to the optical table. (b) Fringe with the isolation platform servoed to minimize accelerations.

### 6.3.1 Noise

The dominant noise source is atom shot noise: the Poissonian fluctuations that arise from detecting atoms in coherent superposition states, also called quantum projection noise [96]. Atom shot noise scales as the square root of the number of atoms detected. As long as there is a sufficiently large number of atoms contributing to the interference fringes, this noise source will be the dominant noise source.

For the  $T = 157.5$  ms gradiometer, the demonstrated SNR is predominantly limited by atom number shot noise. The fringe amplitude corresponds to about  $2.5 \times 10^5$  atoms. At 33% fringe contrast, there is a mean offset of  $7 \times 10^5$  atoms. Based on atom shot noise, these atom numbers put a limit of 300:1 on the SNR for each interference fringe  $\left[2.5 \times 10^5 / (7 \times 10^5)^{1/2}\right]$ . Additionally, normalizing each chamber reduces the SNR for each gravimeter to  $(300/2^{1/2}):1$ . Adding the uncorrelated noise sources from the two gravimeter signals during the fitting decreases the SNR by another factor of  $2^{1/2}$ , fundamentally limiting the SNR for the full gravity gradiometer to 150:1.

The noise produced from photon shot noise on the unabsorbed portion of the probe detection light, corresponding to  $\sim 300$  atom minimum detectable signal, is

approximately at the 800:1 level for each individual fringe, giving about a 400:1 limit after the normalization and differential phase extraction of the two fringes. This means that photon shot noise does not impose a substantial SNR limit for the current number of atoms, but it would become significant for reduced atom numbers.

### 6.3.2 Proof-of-principle mass detection

In order to demonstrate further the sensitivity of the gravity gradiometer, measurement of the gradient of a nearby object was performed. With the sensitivity improved beyond the proo-of-principle results of section 6.1, a measurement of the gravity gradient from small test masses has been made [93]. For this measurement, eight lead bricks ( $\sim 12.5$  kg each) were placed symmetrically near the lower accelerometer,  $\sim 0.2$  m from the apex of the atomic fountain. The calculated acceleration from this configuration of mass was  $8.2 \times 10^{-9}g$ . The results of this measurement are shown in Fig. 6.9. Using the Gaussian elimination method of data reduction, the steps in the phase as the lead is place near the chamber and then removed again are clear. The measured acceleration is  $8.1 \pm 2.1 \times 10^{-9}g$  which agrees well with the expected phase shift. Because the mass is a crude mass, the expected phase is only calculated to about 25%.

## 6.4 Accuracy estimation

### 6.4.1 Tidal measurement

To demonstrate accelerometer (hence gradiometer) accuracy, the accelerometer outputs were monitored over extended periods of time. As in [97] the daily fluctuations in the measured acceleration due to gravity induced by the motion of the Sun and Moon are observed. Fig. 6.10 shows data from one accelerometer taken over a period of several days compared to the Tamura 87 tide model [98]. The only free parameter in this fit is an overall phase offset. From this data set, we constrain the accelerometer phase offset to better than  $10^{-9}g$  over the two day measurement cycle. Subsequent measurements, taken several weeks later, resulted in a similar determination of the

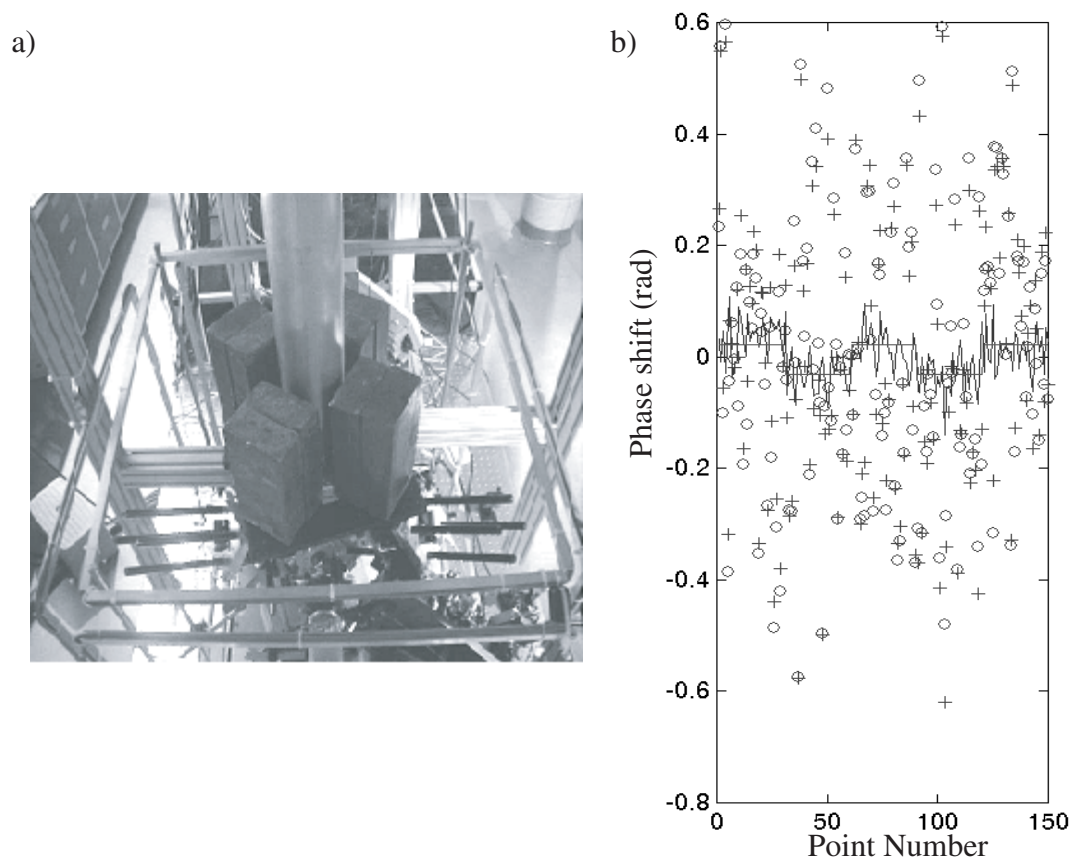


Figure 6.9: a) Picture of the lead bricks positioned above the lower accelerometer. b) Gravitational phase shift measurements made with the bricks near the accelerometer interleaved with data with the bricks removed. The  $\circ$ 's and  $+$ 's are the raw data from the two accelerometers, and the spread in them is due to common-mode vibrational phase noise. The noisy line is the data reduced using Gaussian elimination, and the quiet line is to guide the eye to the time of each change in the position of the bricks.

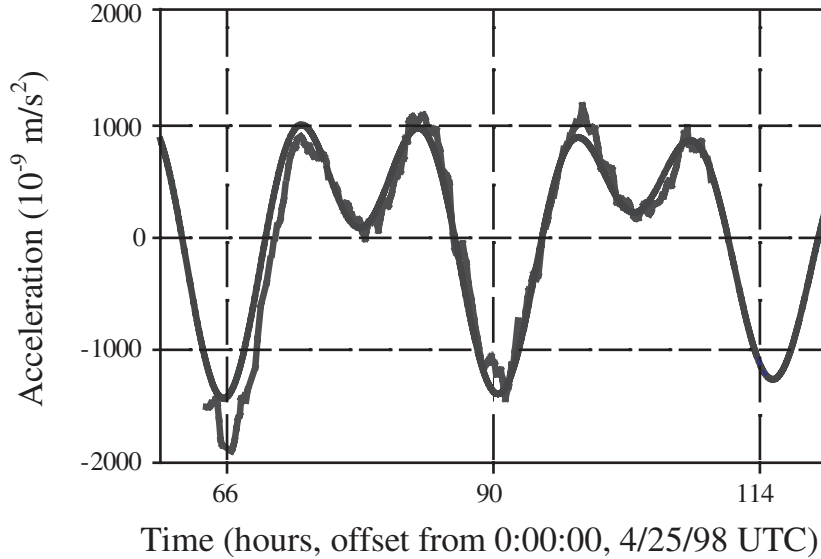


Figure 6.10: Gravitational tidal signals as monitored by one accelerometer over several days. The noisier line is a 20 point running average of the accelerometer data, and the smooth line is the tidal model, with no free scaling parameters.

fitted offset. These measurements denote an accelerometer accuracy of  $< 10^{-9}g$  over time periods of days. The second accelerometer, not shown here, performed equally well over the same period of time. For a 10 m baseline gradient instrument, this corresponds to an inferred accuracy of better than 1 E. Further accuracy studies are underway.

### 6.4.2 Allan variance

Furthermore by performing this long-term integration, the sensitivity of the measurement to small perturbations in the apparatus, including small drifts in laser frequency and intensity, Cs vapor pressure, and ambient magnetic field is characterized. The long-term stability is analyzed by computing the Allan variance of a long, continuous data set [99]. The results are displayed in Fig. 6.11. The Allan variance has a  $\tau^{1/2}$  scaling out to times longer than  $\sim 1000$  s. It appears to begin to flatten out. It is not clear what the source of this drift is, but no effort has been made yet to try to actively stabilize the laser intensities and the Cs vapor pressure. Also, magnetic

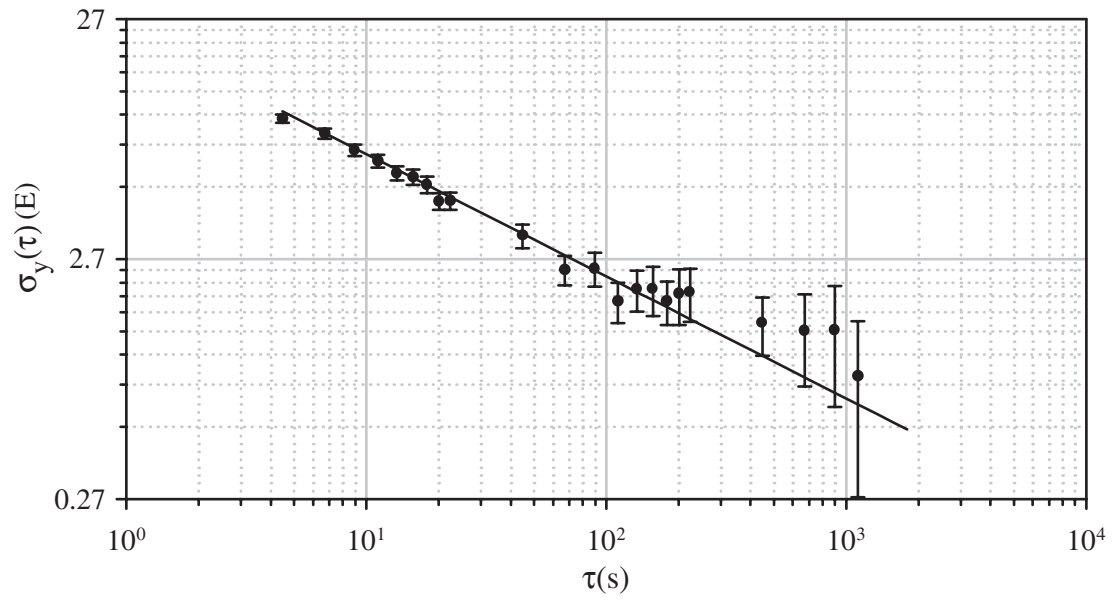


Figure 6.11: Allan variance of  $T = 157.5$  ms gradiometer data monitored continuously for an extended period of time. The sensitivity was not optimal for this data. The data was reduced using the circle routine. Solid line is a  $\tau^{1/2}$  fit, showing white noise scaling.





Figure 6.12: The precision lead test masses for the  $G$  measurement before being placed near the accelerometers and suspended above the lower accelerometer.

shielding might reduce this long-term drift.

### 6.4.3 Gravitational constant measurement

In order to investigate further the instrument stability as well as to perform one of the scientifically interesting measurements discussed in section 2.3, a proof-of-principle measurement of the gravitational constant has been initiated. The concept of this experiment is to measure the gravitational field of a well-characterized test mass as it is brought close to one of the accelerometers in the gradiometer. To this goal, there are two key aspects to the measurement: the precision to which the test mass is characterized and the stability of the experiment over the time needed to measure the test mass to the desired precision.

It is not a trivial matter to obtain a test mass with a uniform density and precise dimensions, particularly one that is suitable for the geometry of the experiment. For our measurements of  $G$ , the test masses are 20 14 in. diameter open bore ultra-pure lead cylinders, each 1 in. high (see Fig. 6.12). The open bore is just large enough to allow the Raman beams to pass through when the lead cylinders are placed above the lower accelerometer. The lead is specified to be 99.99% pure. Each lead disc weighs about 50 lbs and can be measured accurately to greater than a part per  $10^4$  using a calibrated scale. The tolerances on the dimensions are all such that the volume of the

cylinders is only known to a part per 2600 on average. Using these measurements, the density of the lead is known to 0.04%. This uncertainty assumes that the lead is uniform, and there are no air pockets inside of the cast lead. For comparison, an alternate measurement was performed. Small pieces of lead were removed from a spare lead disc. The volume of these pieces was measured using a pycnometer in a water displacement measurement. The volume of water displaced out of a full container of water was measured using a scale and the known density of water. This gave an alternate method of measuring the volume and allowed us to sample small regions of the lead disc to check for inhomogeneities. Due to the small size of the pycnometer, only a small volume of lead was used for the pycnometer measurement, and the density volume was only measured to 0.07%. Both measurements agreed reasonably well at least at the 0.1% level.

The lead is positioned on a cross-braced aluminum platform mounted directly on the floor, so as not to perturb the position of the optical table. The platform has the ability to raise and lower the lead between the two chambers. By doing this, the gravity signal produced by the lead is modulated as the lead is brought near the lower accelerometer and then moved further away. Chopping back and forth allows a method of measuring the gravitational field of the lead while still rejecting low frequency drifts. The platform is able to be lifted up and down over almost two feet in under two minutes using lead screws driven by a stepper motor. The phase shift from the gravitational field of the lead is calculated in the perturbative approximation of section 4.5.2. The field of the discs can be written analytically, and this field is integrated over the unperturbed parabolic paths using Earth's gravity (gradients are neglected here). In order to numerically obtain the precision required, the field due to the Earth is omitted from the action<sup>7</sup>; this is justifiable because the action is linear in these two terms, and there is no coupling between the two fields at the level of interest. By fitting the extracted acceleration measurements for various positions of the lead mass and fitting the theory to this, an accurate measurement of  $G$  can be made. This measurement is currently underway with a target resolution of 0.1%

---

<sup>7</sup>This field is approximately seven orders of magnitude larger than the lead induced phase shift.

## 6.5 Immunity to environmental noise

An important feature of the gradiometer is the ability to reject common mode accelerations in the two measurements. This is critical for a device which might be used on a moving platform. In order to demonstrate this capability, a series of acceleration and tilt tests were performed to characterize the instrument's sensitivity to platform vibration and tilt noise. The effects of accelerations and tilts are characterized by measuring instrument SNR as a function of the amplitude and frequency of an external platform drive.

### 6.5.1 Linear acceleration

We characterized immunity to linear accelerations by shaking the SHP on which the retroreflecting corner cube is mounted. The platform is driven by applying sinusoidal drive currents to the voice coil coupled to the vibration isolation platform. We monitor the resulting platform acceleration with the platform accelerometer (described in section 5.8.1). For this work, the high frequency lead-foam passive isolation between the platform and the corner cube was removed. This study was done with the interferometer operating in its most sensitive configuration (at  $T = 157.5$  ms interrogation time). Fig. 6.13 summarizes the results of these tests. For frequencies in the range 1 to 100 Hz no significant degradation of the SNR was observed for drive amplitudes up to  $2.5 \times 10^{-2}g$ . This corresponds to a common-mode rejection ratio of 140 dB. At amplitudes greater than  $\sim 0.1g$ , the accelerations are large enough that individual Raman pulses are Doppler-shifted out of the Raman resonance condition. At this point, we observe poor interference fringe contrast.

A theoretical study of the effect of vibrations on the interferometer was performed to simulate the transfer function of vibrational noise to the accelerometers. It is expected that because of the pulses at three discrete times, that the transfer function will not be a smooth, monotonic function. More explicitly, for an interferometer of time  $T$  between pulses, if the vibration frequency is a harmonic of  $1/T$ , then the reference platform will be at the exact same position for every single interferometer pulse, and no extra phase noise will be observed. This is shown in Fig. 6.14. This

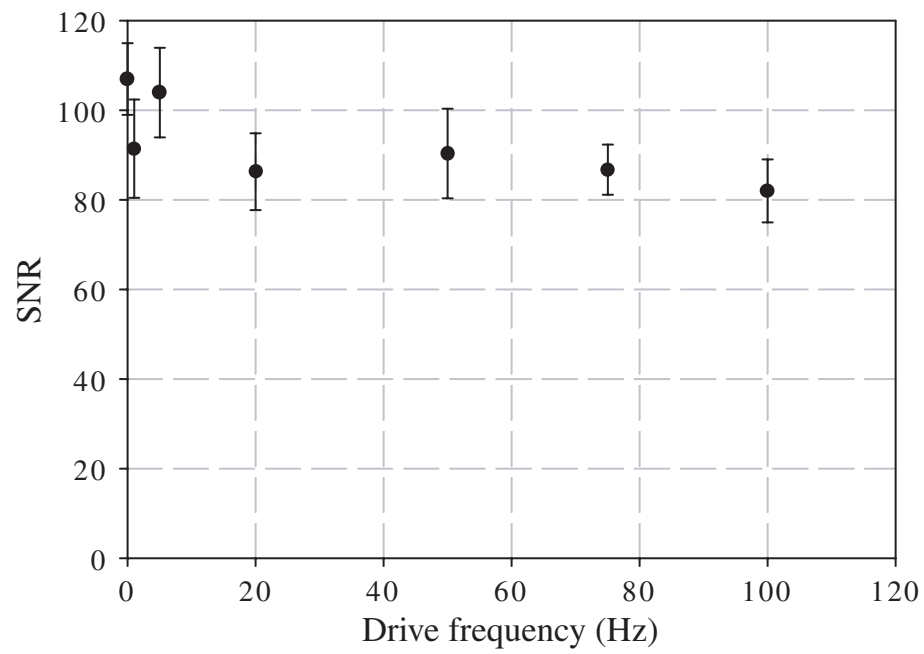


Figure 6.13: Results from the reference platform shake test. No SNR reduction is seen when driving accelerations of the reference cornercube at amplitudes as high as  $10^{-2}g$  over the frequency range indicated. This rejection amounts to 140 dB of common-mode vibration rejection. The observed maximum SNR is slightly decreased from that of Fig. 6.4.

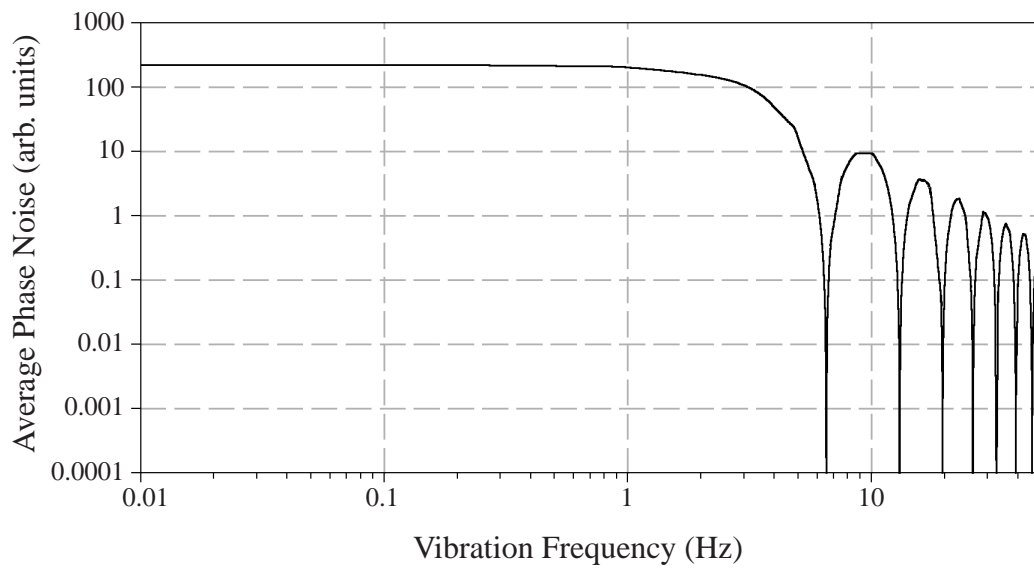


Figure 6.14: Average vibrational phase noise of a given frequency for an interferometer of time  $T = 153$  ms as a function of a platform's vibrations at discrete frequencies and a fixed amplitude.

simulation was performed by using the theory of section 4.4 to calculate the phase shift induced by a platform acceleration  $a = a_o \sin(\omega t)$ . The resulting phase noise was averaged over the relative phase of the driving signal with the interferometer pulse timing. The impact of vibrational noise falls off as  $1/\omega^2$ . It was found that if vibrations of a specific, well-defined frequency are present, then it should be possible to remove their effect entirely by choosing an interferometer time to alias the vibrations.

### 6.5.2 Rotation

Tilts of the Raman interferometer beams are expected to degrade the sensitivity of the measurement. In order to study the effects of small tilt displacements, the optical table on which the gradiometer apparatus was mounted was floated using commercial pneumatic legs (Newport I-2000). Tilt motions were driven with an appropriately placed voice coil and characterized using a tilt meter (Applied Geomechanics 755-1129; specified resolution of  $1 \mu\text{rad}$ , 20 Hz bandwidth). The rotation vector associated with the tilt motion was in a plane perpendicular to the Raman propagation axis, and the center of rotation was approximately 2 m for the accelerometers. Fig. 6.15 shows observed SNR versus maximum tilt amplitude for different driving frequencies. Gaussian elimination was used to reduce this data. At higher frequencies, the massive optical table could not be driven with large tilt amplitudes, and the data could not be extended past  $10 \mu\text{rad}$ .

Both centrifugal and Coriolis forces lead to a degradation in instrument sensitivity. A rotation  $\Omega$  generates a centrifugal acceleration  $R \Omega^2$ , where  $R$  is the distance of one accelerometer from the center of rotation. For two accelerometers separated by distance  $\delta R$ , the differential acceleration is  $\delta R \Omega^2$ , while the acceleration gradient is  $\Omega^2$ . For our operating parameters, we expect this mechanism to begin to degrade the SNR at  $\Omega \sim 10^{-4}$  rad/s. However, full loss in SNR is not expected until  $\Omega \sim 10^{-3}$  rad/s for this mechanism, much higher than the rotation rates employed in this study. However, the Coriolis force leads to a loss in fringe contrast. In this case, the source transverse velocity spread of  $\delta v \sim 3$  cm/s leads to an interference phase spread of  $\delta\phi \sim 2k_{\text{eff}}\delta v\Omega T^2$ . At  $\Omega \sim 10^{-4}$ ,  $\delta\phi \sim 1$  rad, a full loss in contrast is expected. This

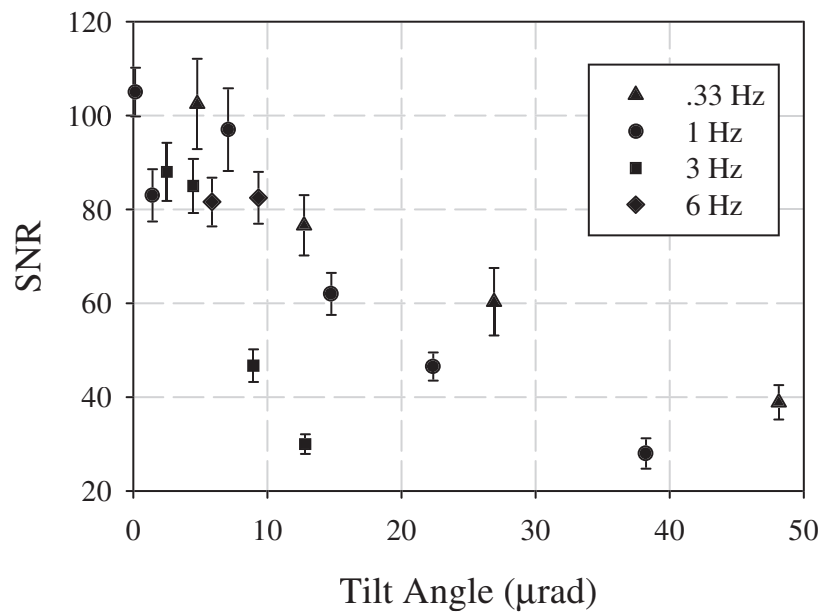


Figure 6.15: Results of the platform tilt test. The floated optical table was tilted at a range of frequencies and amplitudes. The SNR versus peak-to-peak tilt angles is plotted. The SNR is insensitive to tilts for a small range before differential Coriolis forces begin to limit the common-mode vibration rejection and decrease contrast.

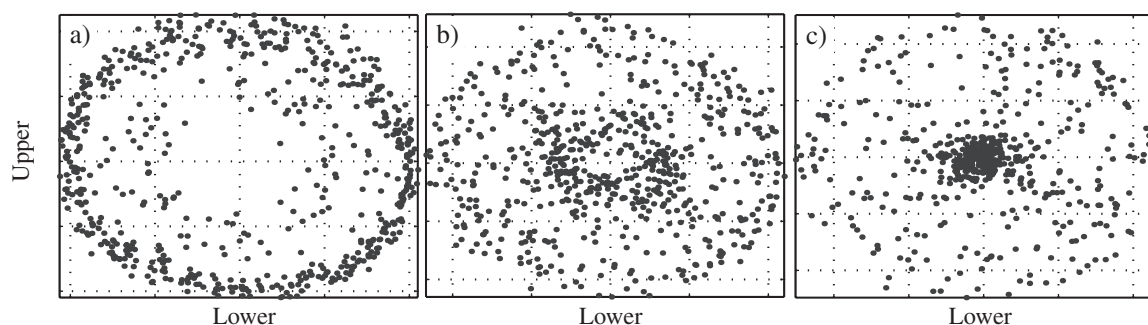


Figure 6.16: Further studies of voice coil-driven rotations on the gradiometer, using the circle method of phase extraction. The loss of contrast is apparent by the points appearing inside the circle diameter with increasing rotation rate. A sinusoidal drive was applied at 1 Hz, inducing a peak rotation rate of a)  $\sim 0.05$  mrad/s, b)  $\sim 0.5$  mrad/s, and c)  $\sim 2$  mrad/s.

is in reasonable agreement with the observations (see Fig. 6.16). Based on the ellipse fitting, it is straightforward to eliminate those points with reduced contrast, however, it may be possible to actively correct for these effects by dynamically adjusting the frequency and phase of the Raman beams.



# Chapter 7

## Discussion

Improvements to the gradiometer have allowed a new level of sensitivity and accuracy to be reached. The new results demonstrate this performance and also probe important technical aspects of the device which allow strong suppression of vibrational noise. In this section, limitations of the current device are discussed. A method of enhancing the sensitivity with the use of multiple Raman pulses is described and demonstrated. Additionally, a comparison is made with several different types of atom interferometers capable of sensing gradients. Finally, several different configurations for measuring the full gradient tensor are described.

### 7.1 Performance Limits

#### 7.1.1 SNR limits

For the  $T = 157.5$  ms gradiometer, the demonstrated SNR is predominantly limited by atom number shot noise. With the current signal levels, the photon shot noise limit from unabsorbed light is close as well. The fringe amplitude corresponds to about  $2.5 \times 10^5$  atoms, and at the typical 33% fringe contrast, there is a mean offset of  $7 \times 10^5$  atoms. Based on atom shot noise, these atom numbers put a limit of 300:1 on the SNR for each interference fringe  $\left[2.5 \times 10^5 / (7 \times 10^5)^{1/2}\right]$ . Additionally, adding in the uncorrelated noise from a second trace by normalizing each chamber

reduces the SNR for each gravimeter to  $(300/2^{1/2}):1$ . Simultaneously using the two gravimeter signals to produce a gradient signal decreases the SNR by another factor of  $2^{1/2}$ , fundamentally limiting the SNR for the full gravity gradiometer to 150:1. This places an upper limit on the sensitivity for a 10 m device of  $4 \text{ E/Hz}^{1/2}$ , when the data collection time (typically 1.4 s per shot) and wild data point reduction are included. The noise produced from photon shot noise on the unabsorbed portion of the probe detection light,  $\sim 325$  atom minimum detectable signal, is approximately at the 800:1 level for each individual fringe, giving about a 400:1 limit after the normalization and subtraction of the two fringes. This means that photon shot noise does not impose a substantial SNR limit for the current number of atoms, but it would become significant for reduced atom numbers.

Improvements to the system could further increase the sensitivity. A larger number of atoms in the interferometer may be possible with improved optical pumping techniques in the state selection or possibly starting with colder atoms to lessen the loss of signal due to ballistic expansion. An increase of four times in the atom number would correspond to an increase in sensitivity to  $2 \text{ E/Hz}^{1/2}$ . Additionally, use of the molasses beams to stop and hold the atoms during detection may make longer integration possible, which should further reduce the background noise on the signal. With a ten times longer detection integration, photon shot noise would be reduced by a factor of three, which would make the photon shot noise negligible even with fewer atoms. Another promising approach is the use of multiple pulse interferometers which have been demonstrated [100]. Multiple pulses result in larger momentum transfer to the atoms which leverages the sensitivity up. This technique is described in section 7.2.1. Extending an interferometer with  $6\hbar k$  wavepacket splitting to the current setup with a  $T = 157.5 \text{ ms}$  interferometer would push the sensitivity below  $1 \text{ E/Hz}^{1/2}$ , when used in conjunction with greater atom numbers.

### 7.1.2 Rotations

Another, less fundamental, potential problem with the gradiometer concerns rotations. Rotations are detrimental to the gradiometer's performance for several reasons.

Firstly, rotations can lead to a loss in fringe contrast due to differential Coriolis forces due to the velocity spread of the atoms as described in section 6.5.2. Additionally a rotation of the reference platform causes a differential Raman path length change between the two chambers. This leads to non-common-mode phase shifts. As previously described, phase shifts between the chambers reduce the ability to remove common-mode vibrations, which limits the sensitivity in the presence of tilts. This effect could be accounted for by accurately measuring the tilts, and calculating the tilt-induced phase shifts. In this manner, the common mode vibrational rejection could be regained using a commercial gyroscope in an open-loop fashion. Another harmful effect of tilts is the misalignment of the measurement axis. It is important that the gradient measurement axis, defined by  $\mathbf{k}_{\text{eff}}$ , stay constant. However, because the gravitational phase shift is proportional to  $\mathbf{k}_{\text{eff}} \cdot \mathbf{g} = k_{\text{eff}}g \cos\theta$  for angle  $\theta$  between the two vectors, this effect is second order in  $\theta$  in the small angle limit. Finally, rotations can lead to systematic offsets. Atom interferometers are highly sensitive to all inertial forces. If the atom interferometers enclose any physical area, they become Sagnac type gyroscopes in addition to accelerometers, and they measure the Coriolis force experienced by the atoms. This rotation sensitivity can arise if the atoms have transverse velocity relative to the measurement axis. With precise alignment of the atomic fountain so that the average transverse velocity is zero, this effect can be removed. All of these rotation effects can be somewhat overcome either with careful alignment or with the use of a commercial gyroscope to compensate, open or closed loop, for rotations. One further problem with rotations comes in the complex way they enter the phase shift calculations in the presence of gravity and gravity gradients (see section 4.6.3). Even if the rotations are completely characterized, there is not a sufficient analytic theory for calculating their phase shift down to the precision levels required for applications such as test of general relativity.

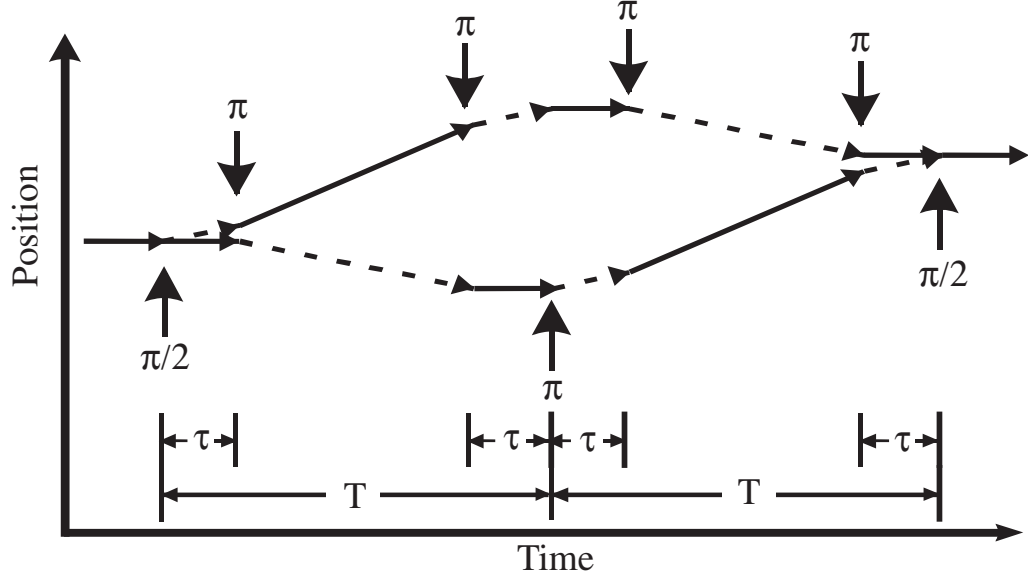


Figure 7.1: A recoil diagram of a  $6\hbar k$  interferometer. Solid and dotted lines represent the two internal atomic states. The arrows represent the Raman pulses with the arrow pointing in the direction of the Raman propagation vectors. Typically  $T \gg \tau$ .

## 7.2 Related methods

### 7.2.1 Large area interferometers

An advanced interferometer scheme to obtain higher sensitivity to gravity gradients was developed [100]. This scheme uses extra Raman pulses to transfer larger relative momentum to the two wavepackets in the interferometer, thereby creating a larger enclosed area in recoil space. The sensitivity scales approximately with the recoil diagram enclosed area. The most simple sequence of this nature is one that transfers  $6\hbar k$  relative momentum to the wavepackets.

The  $6\hbar k$  interferometer is similar to the  $2\hbar k$  interferometer sequence described in section 4, and it consists of three parts: an initial beamsplitting pulse sequence, a mirror sequence, and a recombining sequence. This sequence, depicted in Fig. 7.1, is similar to the basic sequence described in Chapter 4, except each individual pulse is now replaced with a sequence of light pulses. The initial beamsplitter consists of two pulses of light that are spaced closely by time  $\tau$ . All pulses are two-photon

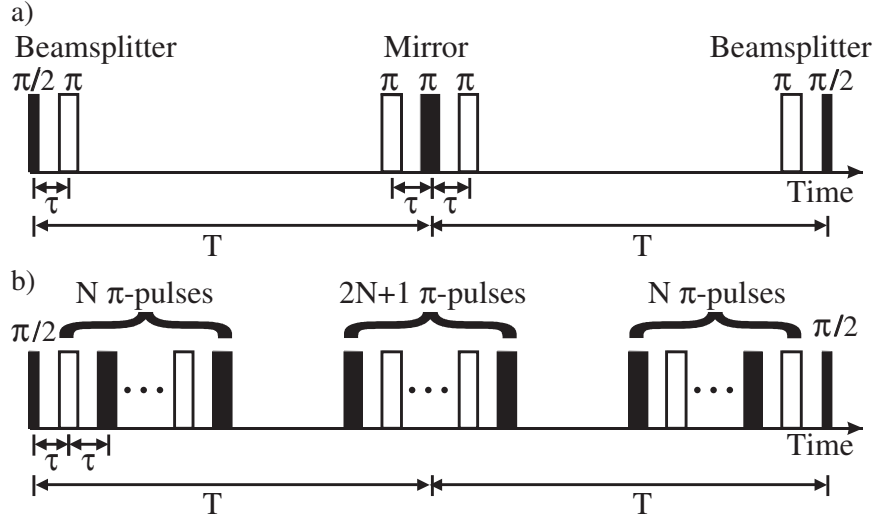


Figure 7.2: Time domain representation of the interferometer. Raman pulses of opposite propagation direction are depicted by the light and dark pulses. (a) is a  $6\hbar k$  interferometer pulse sequence, and (b) shows a generalized sequence for a  $(4N+2)\hbar k$  interferometer.

stimulated Raman transitions. The first is a  $\pi/2$  pulse, followed by a  $\pi$  pulse in rapid succession, but with the optical propagation vectors reversed. This  $\pi$  pulse further splits the atomic wavepackets in momentum by increasing the momentum difference between wavepackets to  $6\hbar k$  ( $3\hbar k_{\text{eff}}$ ). The atoms are allowed to drift freely for a time  $T - 2\tau$  that is usually long in comparison to both the pulse length and the time  $\tau$  between the beamsplitter pulses [see Fig. 7.2(a)]. A series of three  $\pi$  pulses in rapid succession, each of alternating propagation direction, acts as a mirror by re-directing the wavepackets back towards each other with relative momentum  $-6\hbar k$ . After another free evolution period of time  $T - 2\tau$  a final beamsplitting sequence recombines the atomic wavepackets when they overlap again. This sequence consists of a  $\pi$  pulse and then a final  $\pi/2$  pulse with reversed propagation vectors, similar to the initial beamsplitter sequence. This method is related to earlier proposals which employ sequences of optical pulses to manipulate atomic wavepackets [101, 102]. The difference between these proposals and the experiments presented here is that, in our experiments, pulse parameters are chosen to address both interferometer arms simultaneously, whereas in the previously proposed schemes, additional pulses only

address one arm of the interferometer at a time.

To derive the acceleration induced phase shift for the  $6\hbar k$  interferometer, the rules outlined in section 3.7 for two-photon stimulated Raman transitions are applied similarly to section 4.4. Performing this calculation for the seven pulse sequence gives:

$$\Delta\phi = [\phi(t_1) + 2\phi(t_2)] - 2[\phi(t_3) + \phi(t_4) + \phi(t_5)] + [2\phi(t_6) + \phi(t_7)]. \quad (7.1)$$

The three quantities in brackets correspond to the phase imparted to the atoms by the initial beamsplitting pulses, the mirror pulses and the recombining pulses respectively. Here  $t_i$  is the time of the  $i^{th}$  pulse, and  $\phi(t_i) = \mathbf{k}_{\text{eff}} \cdot \mathbf{x}(t_i) + \phi_i^\circ$  are the effective phases of the laser fields at the positions  $\mathbf{x}(t_i)$ . The positions  $\mathbf{x}(t_i)$  are evaluated with respect to the classical trajectories associated with the atomic wavepackets, and  $\phi_i^\circ$  is the phase reference for the  $i^{th}$  pulse and is taken to be zero for these calculations (see section 4.4.2). Finally, the smaller terms in the total phase from the free propagation of the atoms and the final wavepacket overlap are neglected here<sup>1</sup>. This expression simplifies to:

$$\Delta\phi = 3\mathbf{k}_{\text{eff}} \cdot \mathbf{g}T^2 - 4\mathbf{k}_{\text{eff}} \cdot \mathbf{g}T\tau. \quad (7.2)$$

In our geometry, this becomes:

$$\Delta\phi \simeq 6kgT^2 - 8kgT\tau, \quad (7.3)$$

where  $k_{\text{eff}} \simeq 2k$ . This shift is approximately three times the phase shift expected from a  $\pi/2 - \pi - \pi/2$  pulse sequence for long interrogation times  $T$ . The area enclosed by interfering wavepacket trajectories has increased by the same factor<sup>2</sup>. It is stated without proof that the sensitivity of a Raman pulse-type interferometer scales linearly with recoil diagram area, to first order.

The Raman propagation vector reversal is achieved by means of the Pockels cell. Adjusting the voltage applied to the Pockels cell simultaneously rotates the polarization of the orthogonally polarized Raman beams. This is done exactly as in the

---

<sup>1</sup>These two terms are treated exactly as in the  $2\hbar k$  case.

<sup>2</sup>There is no physical area enclosed, only area in the recoil diagram.

method of rejection of systematics using propagation reversal, except here, the propagation is changed every for pulse, instead of changed each experimental cycle. The Pockels cell nominally can switch polarizations in  $\sim 1 \mu\text{s}$  but takes about  $150 \mu\text{s}$  to settle completely. For this reason,  $\tau = 150 \mu\text{s}$  is the minimum time used between pulses in the pulse sequence.

We obtain interference fringes by scanning the phase of the middle interferometer pulse in the mirror sequence similar to the way interference fringes are generated for the  $2\hbar k$  experiment. For this experiment, the phase of each fringe is found by performing a least squares fit on each fifty point interference scan<sup>3</sup>. By varying the free evolution time in the interferometer, we obtain a curve of phase shift versus expansion time  $T$  (see Fig. 7.3). Each point is an average of twenty interference scans. We compare the gravitational phase shift from  $2\hbar k$  and  $6\hbar k$  interferometers. The solid lines represent theoretical fits to the data of  $\Delta\phi = 2kgT^2$  for the  $2\hbar k$  interferometer and  $\Delta\phi = 6kgT^2 - 8kgT\tau$  for the  $6\hbar k$  interferometer. The only free parameter is a constant phase offset which results from the initial arbitrary laser phase  $\Delta\phi^\circ$ .

Using the  $6\hbar k$  interferometer interferometer time  $T$  was extended from 30 ms (Fig. 7.4). For  $T > 30$  ms, the fringes are obscured by excessive phase noise from vibrations of the Raman retro-reflecting mirrors below the chamber. This work was done looking at fringes from a single accelerometer. By using both accelerometers and one of the data extraction methods for high phase noise regimes, these common mode vibrations can be removed.

In principle, this process is extendable up to  $(4N + 2)\hbar k$  momentum transfer by adding extra  $\pi$  pulses, as illustrated in Fig. 7.2(b). The essential idea is that application of subsequent pulses with reversed propagation vectors leads to a linear accumulation of the optical phase in the atomic coherences just as it causes a linear increase in relative momenta between wavepackets. This leverages interferometer sensitivity by providing a finer grained “ruler” for determining force-induced changes in wavepacket positions.

In practice, several factors limit the length of the pulse sequence which may be

---

<sup>3</sup>This work was done before the ellipse fitting method was pioneered.

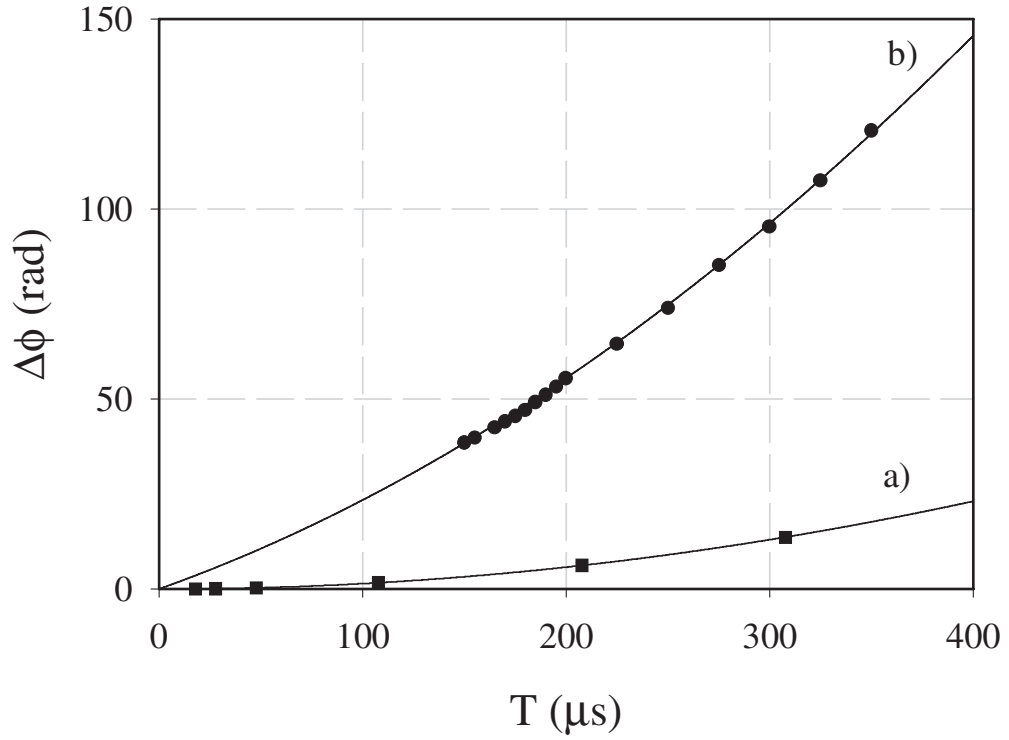


Figure 7.3: Comparison of the phase shift  $\Delta\phi_{\text{tot}}$  due to the Earth's gravity as a function of free expansion time  $T$  for (a)  $2\hbar k$  and (b)  $6\hbar k$  interferometers. Solid lines represent theoretical curves. Each interferometer had an arbitrary constant phase offset due to the particular pulse parameters ( $\phi_{\text{laser}}$ ) that has been suppressed. The phase uncertainty for each point is about  $\pm 15$  mrad, giving excellent agreement with theory.



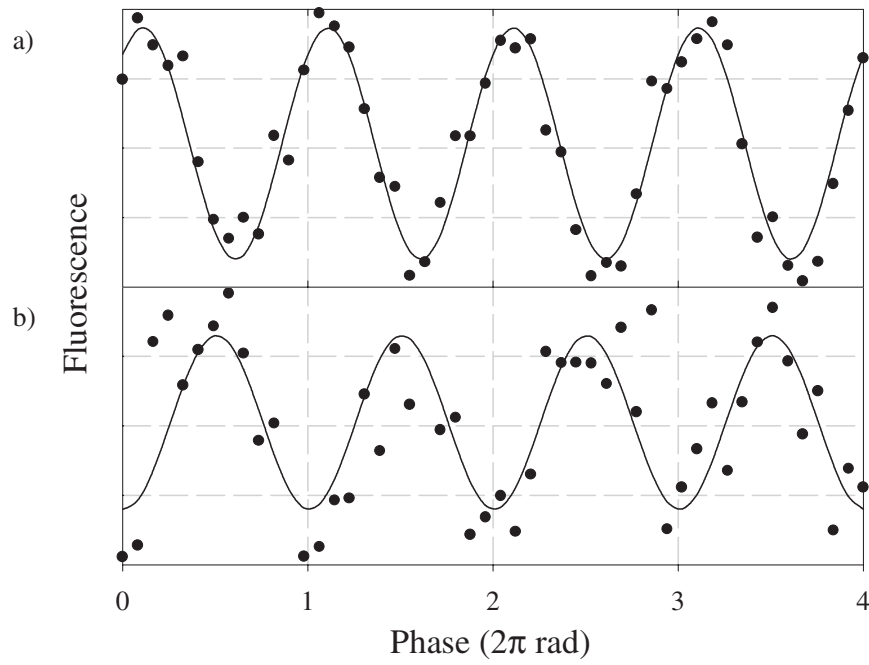


Figure 7.4: Typical interference fringes from (a) a  $2\hbar k$  interferometer and (b) a  $6\hbar k$  interferometer each with  $T = 30$  ms. Fringe contrasts are typically 40% and 30% respectively. The solid lines are least squares fits to the data. The extra noise in (b) is due to increased sensitivity to vibrations due to increased acceleration insensitivity.

used. First, spontaneous emission during the Raman transitions due to weak coupling to the allowed single-photon transitions to the intermediate state homogeneously dephases the atomic coherence and places a lower limit on the optical detuning for the Raman pulses. This places an upper limit on the two-photon Rabi frequency, thereby limiting the velocity class of atoms selected by the pulses. For our parameters, we experience 1% spontaneous emission for each  $\pi$  pulse. Second, the Gaussian spatial profile of the Raman beams leads to an inhomogeneous distribution of effective Rabi frequencies. This introduces a spread in pulse area across the atomic spatial distribution and ultimately limits the ensemble transfer efficiency of each  $\pi$  pulse. Additionally, the frequency selectivity of the interrogating pulses limits the number of pulses in the sequence, as the linewidth of each pulse needs to accommodate the differential Doppler shifts in the transition frequencies due to the recoil momentum imparted to the atomic wavepackets by previous pulses. Finally, due to the inefficiencies mentioned, less than perfectly efficient pulses can lead to a superposition of interferometers, *e.g.* wavepackets following both a  $2\hbar k$  and a  $6\hbar k$  loop at the same time, resulting in an averaging of the phase shifts for the two interferometer loops.

We are exploring methods to overcome the above limitations to realize high momentum transfer atom optics. There do not appear to be any serious barriers to realization of momentum transfers greater than  $10\hbar k$ . Such high momentum beam splitters would offer new levels of sensitivity for atom interferometer based precision measurements.

### 7.2.2 Interferometer comparisons

There have been several investigations of gravimeters with different types of atom interferometers. These include atom interferometers based on multiple pulse techniques using stimulated Raman transitions (see section 7.2.1), Bragg scattering, diffraction in the Raman-Nath regime, adiabatic transfer, and the AC Josephson effect with Bose-Einstein condensates (BEC). The advantages and disadvantages of each technique will be discussed here.

The  $6\hbar k$  interferometer should prove to be a sensitive gradient sensing tool. This

method might be extended even further using special sequences of composite pulses (see section 5.5.2). The benefits of using composite pulses in this context would be an large range of selected velocities for a fixed Rabi frequency and robust suppression of spatial inhomogeneities in Rabi frequency (which arise due to the spatial intensity profile of the gaussian Raman laser beams). For example, consider the following sequence. A high efficiency composite microwave pulse could be used for the initial  $\pi/2$  pulse. Next a composite optical  $\pi$  pulse gives the wavepackets  $4\hbar k$  momentum splitting, and after a long drift time two composite  $\pi$  pulses redirect the wavepackets back towards each other. Finally, a last composite optical pulse and another composite microwave pulse recombine the wavepackets to complete the interferometer. Because it uses coupled composite pulses, simulations have shown that this interferometer could result in extremely high contrast interference fringes due to its increased insensitivity to inhomogeneous broadening.

Bragg scattering-based interferometers diffract atoms from standing waves of laser light. As in the light-pulse interferometers, these interactions can be configured as atom optic beamsplitters and mirrors [103]. The primary virtue of Bragg scattering interferometers is that the atoms always remain in the same internal state. The effects of many systematic phase shifts such as Zeeman shifts and AC Stark shifts are reduced, since the wavepackets in each arm of the interferometer experience symmetric phase shifts due to these effects. In comparison, the Raman method requires the use of propagation vector reversal techniques to gain immunity to these possible systematics. Furthermore, high-order Bragg diffraction can be used to create large-area, high-sensitivity instruments. However, high-order Bragg processes only operate efficiently over a relatively narrow range of initial atomic velocities (significantly less than a photon recoil velocity). This severely constrains the fraction of atoms which can contribute to the interference signal, and thus the sensitivity drops due to small atom counting rates. On the other hand, BEC or atom laser sources may eventually produce extremely bright atomic beams (having excellent velocity collimation) [55, 104]. In this case, Bragg processes may become a competitive choice for interferometer sensors, however it is unlikely that robust condensates will be developed in the near future.

A gravimeter based on diffraction in the Raman-Nath regime has also been demonstrated [105]. In this interferometer, short, intense pulses of highly focused light are applied to the atom. Because of the short pulse and tight focus, atoms are diffracted into a large spread of momentum states, with many multiples of  $2\hbar k$  present. Two Raman-Nath pulses are used to construct the interferometer, and because of the wide spread of momentum, many different interfering paths exist. Some of these paths overlap and interfere after an echo time, which determines the sensitivity to gravitational phase shifts. The many paths increase the finesse of the interference fringes and provide greater ability to resolve phase shifts than for single path interferometers for identical SNRs. This sensitivity scales with increasing echo time. However, Raman-Nath diffraction populates many higher lying momentum states that do not contribute to the closed interferometer paths, which decreases the interferometer contrast and limits the SNR by limiting the counting statistics. A comparison is given between the gravitational phase shift in a Raman interferometer and a Raman-Nath interferometer, based on the theoretical treatment in [105]. For equal total interferometer time  $(N + 1)T$ , the ratio of the Raman-Nath phase shift,  $\mathbf{k}_{\text{eff}} \cdot \mathbf{g}T^2N(N + 1)/2$  for the  $N^{\text{th}}$  echo, to the Raman phase shift,  $\mathbf{k}_{\text{eff}} \cdot \mathbf{g}T^2(N + 1)^2/4$ , is given by  $2N/(N + 1)$ . The maximum theoretical interferometer contrast is used as a weighting factor here: 100% for Raman interferometers and for Raman-Nath devices the maximum of  $J_N$  and  $J_{N+1}$  for the  $N^{\text{th}}$  echo where  $J_N$  is a first order Bessel function. Because of the severe drop in contrast for Raman-Nath beamsplitters, the maximum effective momentum transfer is only approximately  $0.5\hbar k$  when after the decreased counting statistics are included, which is twelve times less sensitive than a  $6\hbar k$  Raman-type interferometer. Additionally, if the shot noise from the atoms in momentum states not contributing to the signal is considered, the Raman-Nath interferometer is 42 times less sensitive than a  $6\hbar k$  Raman interferometer. This relative sensitivity becomes even worse for higher order Raman beamsplitters, *e.g.*  $10\hbar k$  and higher. Even with an ultra-cold source, sensitive Raman-Nath gravimeters and gradiometers seem infeasible.

Adiabatic transfer recently has been used in a proof-of-principle demonstration of a possible large-area interferometer [106]. In this approach, atoms are put into coherent superpositions of two states using a microwave pulse. Momentum is transferred to one

state in this superposition by adiabatically transferring it from the  $m_F = 0$  sublevel to the highest (or lowest) lying  $m_F$  level [51]. Adiabatic transfer is used subsequently to manipulate and ultimately to overlap the wavepackets. A final microwave pulse is then used to interfere these wavepackets. This method can transfer up to  $2m_F\hbar k$  momentum to one arm of the interferometer. The primary limitation to the utility of this method is that the adiabatic transfer populates magnetic field sensitive sublevels. This makes the interferometer sensitive to Zeeman shifts, *e.g.* a 1 mG difference in field between two 150 ms interferometers in a gradiometer produces a phase change of  $\sim 30$  rad, which is similar in size to a change of  $2.5 \times 10^{-6}g$ . While such an interferometer may demonstrate a high sensitivity, it remains to be seen whether it can achieve high accuracy.

Finally, the AC Josephson effect in arrays of Bose-Einstein condensed atoms [107] has been used to make a proof-of-principle gravity measurement. In this approach, condensate atoms tunnel from an array of vertically spaced lattice sites. Atoms tunnelling from different sites subsequently interfere. The resulting interference pattern is a periodic train of atom pulses whose frequency depends on the strength of the gravitational potential. This frequency can be measured with high accuracy using conventional atom detection techniques. A major technological drawback to this technique is the need for Bose-Einstein condensed atomic sources, which still are difficult to produce and not suitable for a portable apparatus. Also, the time required to condense atoms is typically in excess of 30 s, which results in a low instrument bandwidth. However, if techniques to produce robust, BEC atom sources improve, this method may become viable for future instruments.

### 7.2.3 Multi-loop interferometers

There are several Raman-pulse based schemes which can be used for direct gravity gradient measurements. The simplest of these is the double-loop, or figure-eight, interferometer which was first proposed in [12]. This geometry can be easily achieved in the light-pulse method by inserting an extra  $\pi$  pulse into the light-pulse sequence. Instead of applying a  $\pi/2$  pulse for the third pulse, the two atomic wavepackets are

allowed to pass through each other and form a second loop [see Fig. 7.5b]. Next a second  $\pi$  pulse redirects the wavepackets to close the second loop, and a final  $\pi/2$  pulse interferes the wavepackets. This pulse sequence directly produces a phase shift proportional to the gravity gradient by essentially performing a coherent subtraction of two spatially, and temporally, separated gravity measurements (one for each loop). Following the pulse rules presented in section 4.4, the double-loop phase shift is given by:

$$\Delta\phi \simeq \phi(t_1) - 2\phi(t_2) + 2\phi(t_3) - \phi(t_4), \quad (7.4)$$

where  $\phi(t_i)$  is the phase of the  $i^{th}$  Raman pulse at the position of the atomic wavepacket at time  $t_i$ . Evaluating this phase, assuming a linear gravitational gradient  $g(z) = g_o + \alpha z$  along the sensitive axis, gives:

$$\Delta\phi \simeq 8kg_o\alpha T^4, \quad (7.5)$$

where  $g_o$  is the gravitational component along the Raman wavevector at the atoms' initial position and  $\alpha$  is the linear gradient. This formula is valid for an interferometer in the first half of a fountain of length  $8T$  and for  $\alpha z' \ll g_o$  where  $z'$  is the total height of the fountain.

One problem with this approach is that, for a given fountain height, the double-loop interferometer is maximally sensitive when the interferometer occurs in only one half of the fountain. If the interferometer spans the whole fountain time, *i.e.* is symmetric about the fountain's peak, then the gravity signal from each loop will be identical, resulting in no phase shift. Thus, to obtain gradient sensitivity, the double-loop must be used only in the first half or the second half of the fountain, which severely constrains the possible instrument sensitivity. (This means the maximum interaction time for our fountain is  $T = 39$  ms, resulting in 3000 times less sensitivity to gradients as compared with two single loop interferometer which are separated by 10 m.) In addition to this sensitivity limit, it is difficult to make the gradiometer baseline arbitrarily large and there is no common-mode vibration rejection, since each of the two acceleration measurements which comprise the gravity gradient signal are

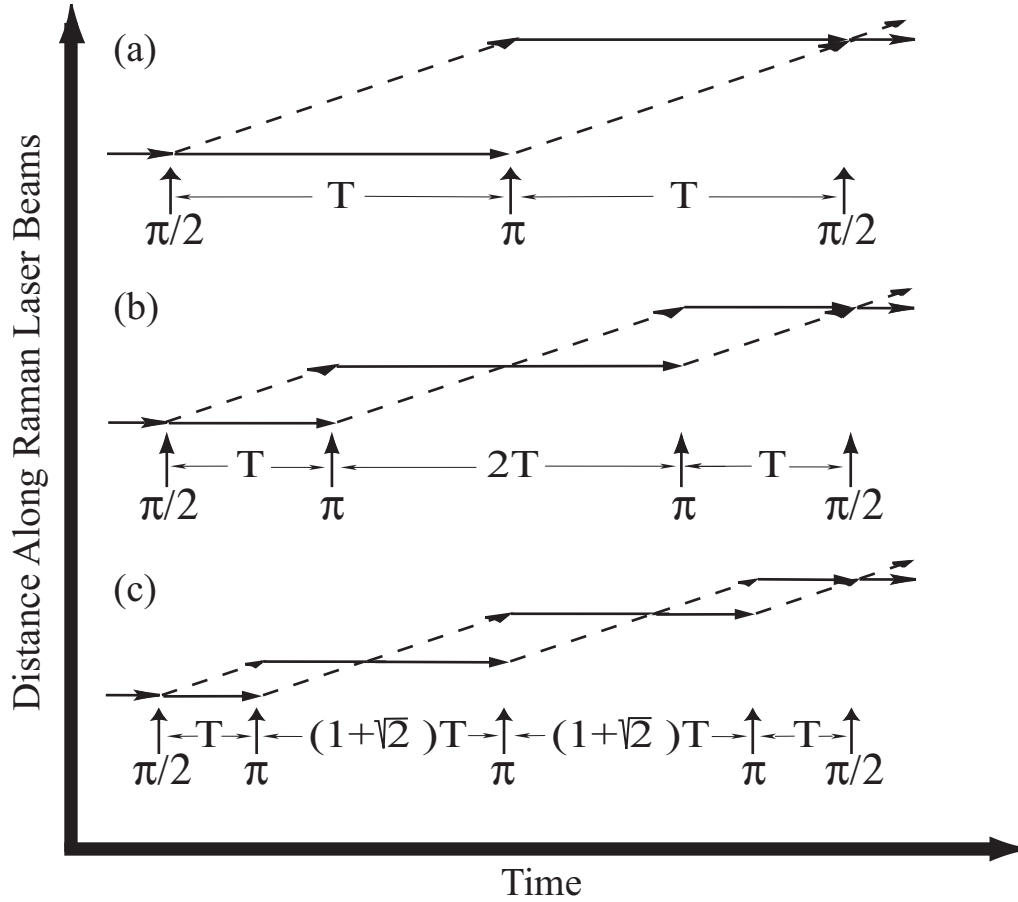


Figure 7.5: Recoil diagrams for various interferometer sequences. Solid and dotted lines represent the  $F = 3$  and  $F = 4$  states respectively. The time of the Raman pulses is denoted by the vertical arrows. a) Single-loop accelerometer. b) Double-loop (figure eight) gradiometer. c) Triple-loop gradiometer.

made at differing times.

A slight modification of the double-loop method allows full use of the fountain interaction time, resulting in a three-fold increase in sensitivity from a double-loop interferometer in an apparatus of equivalent size. This modified sequence uses an extra  $\pi$  pulse in a  $\pi/2 - \pi - \pi - \pi - \pi/2$  sequence, which creates a triple-loop interferometer as seen in Fig. 7.5(c). The phase shift is:

$$\Delta\phi \simeq \phi(t_1) - 2\phi(t_2) + 2\phi(t_3) - 2\phi(t_4) + \phi(t_5), \quad (7.6)$$

which reduces to:

$$\Delta\phi \simeq \left(\frac{17}{3} + 4\sqrt{2}\right) kg_o \alpha T^4, \quad (7.7)$$

again assuming a linear gradient and an interferometer that now spans the entire fountain time,  $(8 + 4\sqrt{2})T$ . This interferometer may be symmetrically spaced about the fountain's apex, so that the maximal interrogation time is  $T = 46$  ms for our fountain. Typical interference fringes from a triple loop interferometer are shown in Fig. 7.6. The 10 m single-loop, two chamber gradiometer still is 1000 times more sensitive due to its larger baseline and longer effective interrogation time. In addition, the triple-loop gradiometer, like the double-loop, does not provide vibration rejection, has a limited baseline, and is only slightly less sensitive to magnetic fields.

### 7.2.4 Curvature measurements

Two multiple-loop gradiometers may be used in conjunction to measure the second moment of the gravity field, in a configuration similar to that used to measure the gradient with two single loop interferometers, except with a triple-loop interferometer performed on each atom ensemble. In this case, the triple-loop gradient phase shifts obtained from two spatially separated atomic ensembles are subtracted to obtain the second order curvature of the gravitational field. This device does have immunity to spurious vibrational noise because measurements are made simultaneously with respect to a common platform. Proof-of-principle data is shown in Fig. 7.6. Measurement of the second moment of the gravitational field allows differentiation between



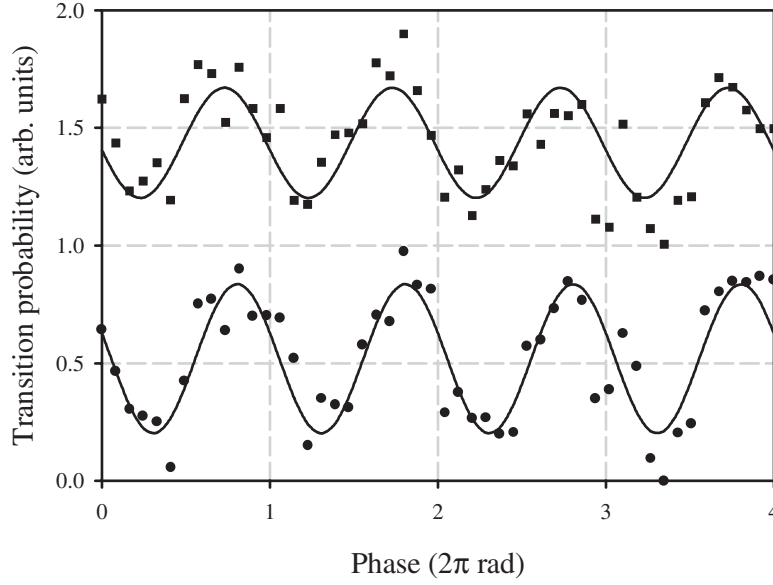


Figure 7.6: Typical interference fringes from  $T = 44$  ms triple-loop interferometers in the lower and upper chamber. The solid lines are least squares fits, and the phase difference between the two fringes represents a measurement of the second moment of the gravitational field.

massive, distant objects and less massive, nearby objects that a gradiometer could not distinguish.

A more direct and sensitive way to characterize the second order moment is to operate simultaneously three single-loop accelerometers spaced equidistantly along a single axis. The difference between gradients obtained by differencing the first and second accelerometer outputs from the second to third accelerometer outputs gives a second moment measurement. This device should have the same benefits as the previous device and would be significantly more sensitive. The disadvantage of such a system is the added size and complexity of a third accelerometer.

### 7.2.5 Multi-axis gradiometers

Lastly, it is desirable to measure the entire gravity gradient tensor rather than just a single component as the gradiometer presented here does. By doing so, the gravity field may be more thoroughly characterized, and a better picture of the surrounding

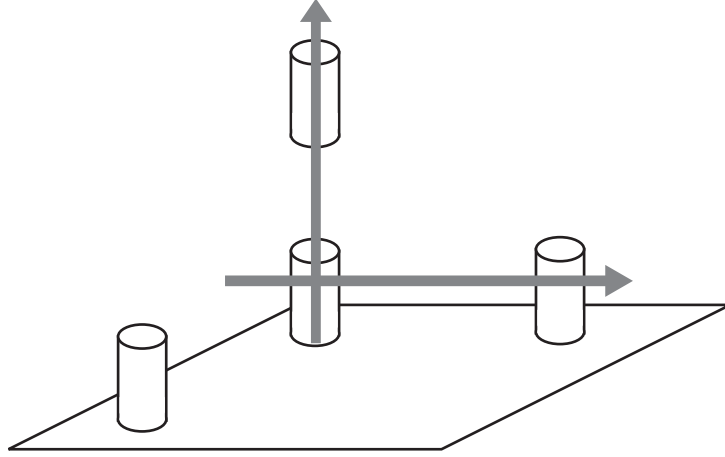


Figure 7.7: Configuration of four accelerometers for a full gradient tensor measurement. Two of the Raman beam paths, each defining a single tensor component measurement, are shown with the arrows.

mass distribution can be obtained. There are several such accelerometer configurations that would be capable of measuring the full tensor. Recall, from section 2.1, that there are only five independent components to the gravity gradient tensor, and thus only five orthogonal gradient measurements need to be performed for full knowledge of the tensor.

The most straightforward configuration for measuring the full gravity gradient tensor requires four accelerometers in a tetrahedral pattern as shown in Fig. 7.7. The wavevector of the Raman beams defines the sensitive axis as well as the axis to which the spatial derivative is taken. By making five measurements with the Raman beams oriented along different axes of the tetrahedron, five different gradient tensor components can be measured, and thus the entire tensor known. Some of the individual gradient measurements measure a combination of two components, but each component can be separated by combining the five measurements. The Raman beam measurement axis can be alternated between the different atom ensembles by coupling the light into different fibers. The beams could be switched between the fibers using a combination of AOMs or electro-optic prisms to route the beams. As with the single axis device, the multi-axis gradiometer can have arbitrarily large baselines. In the case where a stable inertial platform is available, this configuration

can be simplified. In this instance, it is possible to make a full gradient tensor measurement using only three accelerometers. This is only the case if all Raman beam launching optics mounted to different parts of the stable platform vibrate together. This configuration can save on the size and cost of a full tensor system.

Finally, there are more speculative methods that may be able to measure multiple components of the gravity gradient tensor. One such method method relies on the complete theory from Chapter 4. Included in this theory would have to be all possible acceleration terms, including transverse gravitational accelerations and gradients, as well as rotations. If a sufficient analytic approximation for the inertial force induced phase shift can be found, then it may be possible to access individual terms in the analytic expansion of the phase by varying physical parameters of the experiment. For instance, a specific component of the gravity field might be contained in a term that could be amplified by adjusting the interferometer time and launch velocity, as well as perhaps inducing known rotations. It is nontrivial to derive an analytic approximation that agrees well with the exact solution, so this approach might not be possible. Additionally, such effects might be too small to make precise measurements in reasonable integration times.

# Chapter 8

## Conclusion

We have demonstrated a precise and accurate gravity gradiometer based on light-pulse atom interference techniques. In addition, it is the first realization of an absolute gradiometer. The gradiometer has a differential sensitivity of  $4 \times 10^{-9}$  g in 1 s, or in gradient units  $4 \text{ E}/\sqrt{\text{Hz}}$ . The accuracy of the device has been shown to be  $< 1 \text{ E}$ . As verification of the sensitivity, the gravity gradient due to a small test mass was measured. A series of tests to characterize the gradiometer in the presence of reference platform rotations and linear accelerations was performed. A high SNR detection system based on balanced, modulation transfer detection was constructed to achieve the high SNRs required for precision gradiometry. A number of data reduction methods were investigated, and an innovative method based on fitting ellipses to the data was pioneered. This section briefly describes possible apparatus upgrades for the gradiometer, including sensitivity and accuracy enhancements. Finally, the high sensitivity and stability of the gravity gradiometer make possible a number of precision measurements, several of which are discussed here.

### 8.1 Future enhancements

The current sensitivity is primarily limited by shot noise on the number of atoms contributing to the signal. In order to improve this limit, the number of atoms participating in the interferometer and being detected must be increased. At the

present time only a small number of atoms are contributing to the signal. Although a relatively large number of atoms is trapped ( $\sim 10^8$ ) only a few times  $10^5$  contribute the interference fringes. The inefficiencies are threefold. The optical pumping sequence is not efficient, a considerable number of atoms are lost in the atomic fountain itself, and the interference fringe contrast coupled with the velocity selection step limit the signal size even more. Improving the signal levels is expected to improve the overall sensitivity in a direct way.

These inefficiencies all have straightforward solutions conceptually, but the solutions are not easy to implement. Improvements in the optical pumping could result in more atoms in the desired internal state. Such improvements might include an increase in the efficiency of each state preparation pulse, a reduction of rescattering from the thermal background atoms by reducing the vapor pressure, or an altogether different optical pumping scheme. The use of colder atom sources would solve a number of problems. Notably, it would produce more atoms in the detection volume following the atomic fountain by limiting the thermal expansion of the atomic clouds during the fountain. Additionally, because the transverse spatial extent of the clouds would be smaller, the atoms would see a more uniform intensity profile from the Raman beams across the cloud, which would lead to higher fringe contrast. Finally, the fringe contrast would rise due to the narrower longitudinal velocity spread causing less inhomogeneous broadening. This longitudinal narrowing might alleviate the need for the velocity preselection step, again resulting in greater numbers of atoms contributing to the signal. Such an ultra-cold fountain source has been demonstrated based on Raman sideband cooling in a two-dimensional lattice [108, 109, 110]. Additionally, increasing the Raman laser power would allow for larger Rabi frequencies or larger Raman beams, both of which would lead to contrast gains similar to cooling the atoms further.

Multiple pulse interferometers ( $> 2\hbar k$ ) are a promising route to higher sensitivity. Extending the proof-of-principle results for the  $6\hbar k$  interferometer of section 7.2.1 to higher momentum and demonstrating high SNRs for these interferometers would linearly increase the sensitivity to gradients, provided that care is taken to avoid the admixture of  $2\hbar k$  interferometer components as well. Additionally special sequences

involving the advanced pulse techniques described in section 5.5.2 could enable high contrast, large-area interferometers. The simulated sequence described in section 7.2.2 appears to be a promising route to high sensitivity gradient sensing. With a combination of all of these improvements, a sensitivity of  $< 1 \text{ E}/\sqrt{\text{Hz}}$  seems feasible ( $< 7 \times 10^{-10} \text{ g}/\sqrt{\text{Hz}}$  per accelerometer).

Such a high sensitivity gravity gradiometer mandates a thorough study of its accuracy. The current measurement of the gravitational constant provides one such test of accuracy. However, because of the uncertainty in  $G$ , this characterization may not be sufficient for ultra-precise measurements. The same holds true for additional comparison with tidal models. Further characterization of accuracy might be best accomplished by comparison with other absolute gravity gradiometers. A second gravity gradiometer unit is being constructed, and this device could be used to verify the accuracy of the original gradiometer. Furthermore, the accuracy of the gradiometer is limited by the precise knowledge of the distance between the two atom ensembles. There are several steps that could be taken that might increase the stability of the device, based on the philosophy that stabilizing as much as possible in the apparatus would lessen any long-term drift which may be present. Actively stabilizing the intensity of all the beams, including the trapping beams, detection beams, and Raman beams would limit any potential fluctuations due to effect such as drifts of the launch velocity, initial trap position, and Raman beam parameters. Finally, incorporation of magnetic shielding would limit phase fluctuations from the second-order Zeeman shift in the interferometer.

## 8.2 Future measurements

Currently underway is the measurement of the gravitational constant discussed in section 6.4.3. The precision of the experiment is sufficient to make a part-per-thousand measurement of the  $G$  in several days. The current limit to the measurement is the accuracy of the test mass as well as the untested accuracy of the gradiometer at the necessary levels. Several systematic effects are limiting the accuracy. The key effect is magnetic field-induced phase shifts from the magnetic field of the platform used

to hold the lead test mass. After the major systematics have been eliminated, it is expected that the knowledge of the gravity field of the test mass will be constrained at around the 0.1% level. This is still a scientifically interesting measurement, as the current CODATA error bars on  $G$  are approximately 1 part in 700. Furthermore, the light-pulse interference method is an entirely new method of measuring  $G$ , relying on absolute accuracy from the wavelength of the light and using well-characterized single atoms as proof masses. For a more precise measurement of  $G$ , a higher precision test mass is required, and further studies of instrument accuracy are merited.

A sensitive and absolute gradiometer also could make important contributions to precision tests of general relativity. Composition dependence of gravity,  $1/r^2$  dependence, and temporal variations of  $G$  could all be studied in a search for equivalence principle violations. Using a dual-species MOT, consisting of rubidium and cesium for example, a co-located dual-species gravimeter could be constructed. A difference in the gravity experienced by each species would be a manifestation of a breakdown in the equivalence principle. Each species would follow the exact same atomic fountain path. Raman beams of two disparate frequencies would be needed for such a measurement, one pair for each species, but they could use the same optical path. Recent developments in frequency metrology could be used to measure accurately the Raman wavelengths for each species [111]. Similar optical and atomic paths would reduce many experimental systematics. In this situation, the relative frequencies of the beams for each species must be well known.

Also, fifth forces could be sought, particularly those involving atomic spin-gravity couplings. One of the two accelerometers in the gradiometer could be set to drive transitions between the  $F = 3$   $m_F = -1$  and the  $F = 4$   $m_F = 1$  hyperfine sublevels (or the  $F = 3$   $m_F = 1$  and the  $F = 4$   $m_F = -1$  states alternately). This transition is nearly degenerate with the  $F = 3$   $m_F = 0$  and the  $F = 4$   $m_F = 0$  transition, as the first-order Zeeman shift cancels from the two hyperfine levels. By comparing the acceleration from the  $0 \rightarrow 0$  transition with the  $-1 \rightarrow 1$  transition, a search for spin-gravity dependent forces could be performed.

Pursuant to these goals, a second gradiometer is being constructed. The goal of this device is to be both robust and portable. This new gradiometer will take

advantage of compact optics and a simplified system to achieve similar sensitivities in a significantly smaller package. The portable gradiometer could then be used in field tests to characterize gravity gradients from environmental mass anomalies such as oil and minerals and subsurface structures. Additionally, it should be noted that the performance of a gravity gradiometer in a microgravity environment would be greatly enhanced due to the larger available interrogation time ( $\phi_{\text{tot}} \propto T^2$ ) without need for an atomic fountain, and measurements as small as  $10^{-15} g$  would be accessible. Such a high sensitivity device would be ideal for tests of fundamental theories or for high altitude measurements of gradients from terrain features at the Earth's surface. Finally, in order to perform such long interrogation time measurements, the theory of gravitationally and rotationally-induced phase shifts in light-pulse interferometers needs to be refined. Based on its demonstrated sensitivity and accuracy, however, the gravity gradiometer appears poised to make important scientific contributions.



# Appendix A

## Physical parameters of Cs

Property	<sup>133</sup> Cs
cooling transition	$6S_{1/2}, F = 4 \rightarrow 6P_{3/2}, F' = 5$
$\lambda$	852.35 nm
$m$	$2.21 \times 10^{-25}$ kg
$\Gamma/2\pi$	5.18 MHz
$\tau_n$	30.70 ns
$I_{sat}$	1.09 mW/cm <sup>2</sup> (swing transition)
$T_D$	124.39 $\mu$ K
$T_{rec}$ at 852 nm	198 nK
$v_{rec}$ at 852 nm	3.52 mm/s (single-photon)
$\omega_{hf}$	9.192 631 770 GHz (defined)

Table A.1: Properties of Cs

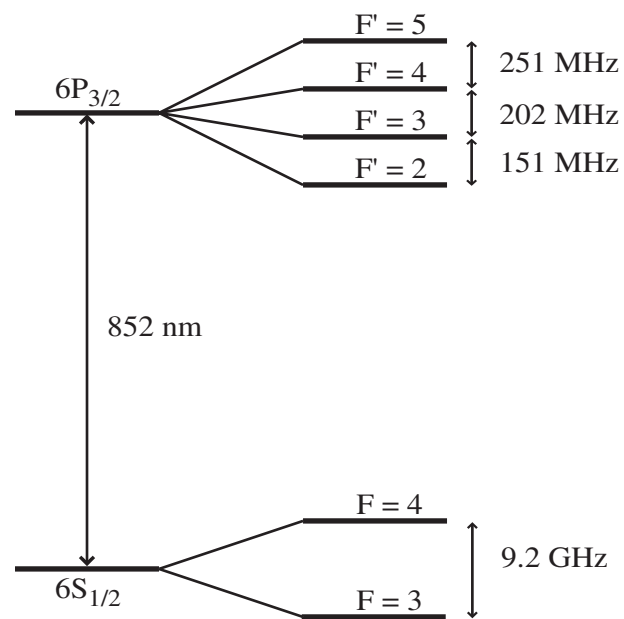


Figure A.1: Energy level diagram for the  $^{133}\text{Cs}$  D<sub>2</sub> line

# Appendix B

## Digital control loops

This section details the digital feedback loop that is used to servo the acceleration of the SHP. First the transfer function of the voice coil-SHP system, including the accelerometer used in the feedback loop, was characterized (see Fig. B.1). Because the accelerometer input has a large offset, the feedback loop has an offset that is ramped up to match the accelerometer offset. This ramp must be done slowly so as not to drive the SHP into oscillations with a sudden impulse. All gains in the feedback loop are ramped up over several minutes to give the low frequency filters time to initialize properly. A high pass filter of 12.5 mHz is applied to the input to filter out low frequency signals outside of the bandwidth of the accelerometer as well.

The main section of the feedback loop originally employed a simple proportional, integral, and differential (PID) gain algorithm. This routine, however, could not produce enough gain in the pass band of the accelerometer-SHP system without causing oscillations outside of this range. Instead a series of lead and lag filters is used to provide high gain while rolling off the gain quickly outside the chosen filter bandwidth. The digital implementation of a lead filter is:

$$\text{Out}(k) = G [\text{In}(k) - z_c \text{In}(k-1)] + p_c \text{Out}(k-1), \quad (\text{B.1})$$

where  $k$  and  $k-1$  represent the discrete steps of the filter. Similarly a lag filter is

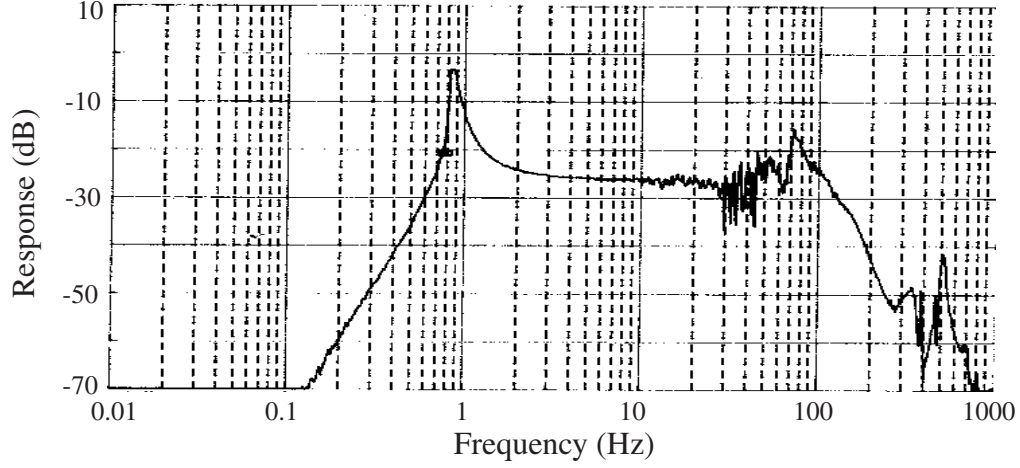


Figure B.1: Transfer function of the SHP-voice coil system as characterized by driving the voice coil with a fixed current and monitoring the on-board accelerometer. The relative response of the system is plotted.

given by:

$$\text{Out}(k) = \frac{2 - f_1}{2 + f_1} \text{Out}(k - 1) + G \frac{f_1(2 + f_2)}{f_2(2 + f_1)} \text{In}(k) - G \frac{f_1(2 - f_2)}{f_2(2 + f_1)} \text{In}(k - 1). \quad (\text{B.2})$$

$G$  is the filter gain, and all other constants produce the frequency cut-offs for each filter.

The first lead filter is applied to roll-off the gain at low frequency. Without a low frequency roll-off, the phase of accelerometer/SHP system crosses through  $\pi$  rad below 300 mHz. Here, the feedback would become positive instead of negative, resulting in low frequency oscillations. A first-order gain roll-off is not sufficient for this, and therefore, a second lead filter is added in series. A lead filter keeps the phase from inverting better than a proportional-integral filter combination. However, in order to get enough gain at higher frequencies (10's of Hz), the gain of the lead filter has to be turned up enough to cause the system to start oscillating at the high frequency phase cross-over of 120 Hz, just outside the accelerometer's 100 Hz low-pass frequency. For this reason, a lag filter is added to roll-off the high frequency gain without perturbing the phase like a simple low-pass filter would. Finally, a second lag filter is added in series to make the high frequency gain roll-off second as well. A summary of the

bandwidths and gains is found in Table B.1.

Filter	Bandwidth	Gain
Lead 1	38 mHz - 200 Hz	1
Lead 2	380 mHz - 200 Hz	1
Lag 1	1 Hz - 80 Hz	200
Lag 2	1 Hz - 80 Hz	80

Table B.1: Vibration isolation system filter bandwidths and gains.

A comparison of the lead/lag filter combination with a digital PID filter is given in Fig B.2. The lead/lag filter combination keeps the phase constant over a larger range, allowing the gain to be increased without driving oscillations at the phase crossover points. Additionally, it rolls the gain off faster at low frequency.

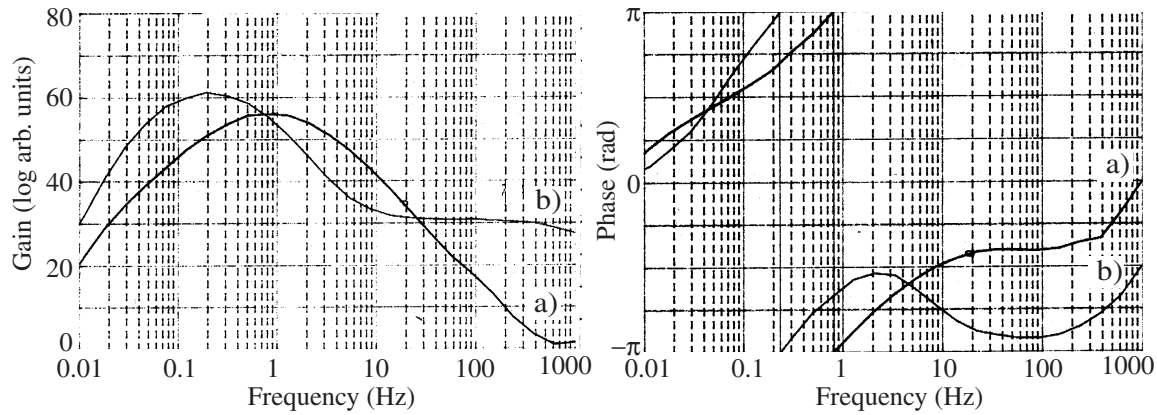


Figure B.2: Gain and phase for a) PID filter and b) lead/lag filter combination.

# Bibliography

- [1] A. Einstein, “Über den Einfluss der Schwerkraft auf die Ausbreitung des Lichtes,” *Annalen der Physik (Leipzig)* **35**, 898–908 (1911).
- [2] T. W. Hänsch and A. L. Schawlow, “Cooling of gases by laser radiation,” *Opt. Commun.* **13**, 68 (1975).
- [3] D. Wineland and W. Itano, *Phys. Rev. A* **20**, 1521 (1979).
- [4] W. Phillips and H. Metcalf, “Laser deceleration of an atomic beam,” *Phys. Rev. Lett.* **48**, 596–599 (1982).
- [5] S. Chu, L. Hollberg, J. E. Bjorkholm, A. Cable and A. Ashkin, “3-Dimensional viscous confinement and cooling of atoms by resonance radiation pressure,” *Phys. Rev. Lett.* **55**, 48–51 (1985).
- [6] E. L. Raab, M. Prentiss, A. Cable, S. Chu and D. E. Pritchard, “Trapping of neutral sodium atoms with radiation pressure,” *Phys. Rev. Lett.* **59**, 2631–4 (1987).
- [7] The Royal Swedish Academy of Sciences, Press Release: The 1997 Nobel Prize in Physics (1997).
- [8] N. F. Ramsey, *Phys. Rev.* **78**, 695–9 (1950).
- [9] R. Colella, A. W. Overhauser and S. A. Werner, “Observation of gravitationally induced quantum interference,” *Phys. Rev. Lett.* **34**, 1472–4 (1975).

- [10] S. A. Werner, J.-L. Staudenmann and R. Colella, “Effect of Earth’s rotation on the quantum mechanical phase of the neutron,” *Phys. Rev. Lett.* **42**, 1103–6 (1979).
- [11] S. Altshuler and L. M. Frantz, “Matter wave interferometric apparatus,” U.S. Patent 3761721 (1973).
- [12] J. F. Clauser, “Ultra-high sensitivity accelerometers and gyroscopes using neutral atom matter-wave interferometry,” *Physica B* **151**, 262–72 (1988).
- [13] D. W. Keith, C. R. Ekstrom, Q. A. Turchette and D. E. Pritchard, “An interferometer for atoms,” *Phys. Rev. Lett.* **66**, 2693–6 (1991).
- [14] M. Kasevich and S. Chu, “Atomic interferometry using stimulated Raman transitions,” *Phys. Rev. Lett.* **67**, 181–4 (1991).
- [15] F. Riehle, T. Kisters, A. Witte, J. Helmcke and C. J. Bordé, “Optical Ramsey spectroscopy in a rotating frame: Sagnac effect in a matter-wave interferometer,” *Phys. Rev. Lett.* **67**, 177–80 (1991).
- [16] M. Kasevich and S. Chu, “Measurement of the gravitational acceleration of an atom with a light-pulse atom interferometer,” *Appl. Phys. B* **54**, 321–32 (1992).
- [17] T. L. Gustavson, P. Bouyer and M. A. Kasevich, “Precision rotation measurements with an atom interferometer gyroscope,” *Phys. Rev. Lett.* **78**, 2046–9 (1997).
- [18] A. Peters, K. Y. Chung, B. Young, J. Hensley and S. Chu, “Precision atom interferometry,” *Philos. Trans. Roy. Soc. A* **355**, 2223–33 (1997).
- [19] M. J. Snadden, J. M. McGuirk, P. Bouyer, K. G. Haritos and M. A. Kasevich, “Measurement of the Earth’s gravity gradient with an atom interferometer-based gravity gradiometer,” *Phys. Rev. Lett.* **81**, 971–4 (1998).
- [20] Loránd Eötvös Virtual Museum, <http://www.elgi.hu/museum>.

- [21] P. R. Bevington and D. K. Robinson, *Data Reduction and Error Analysis for the Physical Sciences* (WCB/McGraw-Hill, 1992), second edition.
- [22] A. Peters, *High Precision Gravity Measurements using Atom Interferometry*, Ph.D. thesis, Stanford University (1998).
- [23] A. Lawrence, *Modern Inertial Technology: Navigation, Guidance, and Control* (Springer-Verlag, New York, 1998).
- [24] B. E. Clotfelter, “The Cavendish experiment as Cavendish knew it,” *Am. J. Phys.* **55**, 210–213 (1987).
- [25] P. J. Mohr and B. N. Taylor, “CODATA recommended values of the fundamental physical constants: 1998,” *Rev. Mod. Phys.* **72**, 351–495 (2000).
- [26] H. W. S. McQueen, “Independence of the gravitational constant from gross Earth data,” *Phys. Earth and Planet. Inter.* **26**, P6–P9 (1981).
- [27] N. I. Kolosnitsyn, “Calibration of gravitational gradiometers using gradient gauges,” *Meas. Tech.* **35**, 1443–7 (1992).
- [28] E. Hantzsche, *Annalen der Physik (Leipzig)* **47**, 401–412 (1990).
- [29] H. Terazawa, *Phys. Rev. D* **22**, 1037–1038 (1980).
- [30] T. Damour and A. Polyakov, “The string dilaton and a least coupling principle,” *Nucl. Phys. B* **423**, 532–58 (1994).
- [31] A. D. Sakharov, “Vacuum quantum fluctuations in curved space and theory of gravitation,” *Sov. Phys.-Dokl.* **177**, 70 (1967).
- [32] G. T. Gillies, “The Newtonian gravitational constant: recent measurements and related studies,” *Rep. Prog. Phys.* **60**, 151–225 (1997).
- [33] E. R. Cohen and B. N. Taylor, “The 1986 adjustment of the fundamental physical constants,” *Rev. Mod. Phys.* **59**, 1121–48 (1987).



- [34] J. H. Gundlach and S. M. Merkowitz, “Measurement of Newton’s constant using a torsion balance with angular acceleration feedback,” *Phys. Rev. Lett.* **85**, 2869–72 (2000).
- [35] C. W. Misner, K. S. Thorne and J. A. Wheeler, *Gravitation* (W. H. Freeman, New York, 1973).
- [36] G. L. Smith, C. D. Hoyle, J. H. Gundlach, E. G. Adelberger, B. R. Heckel and H. E. Swanson, “Short-range tests of the equivalence principle,” *Phys. Rev. D* **6102**, 2001 (2000).
- [37] B. Mashhoon, “Gravitational couplings of intrinsic spin,” *Classical Quant. Grav.* **17**, 2399–2409 (2000).
- [38] D. J. Wineland, J. J. Bollinger, D. J. Heinzen, W. M. Itano and M. G. Raizen, “Search for anomalous spin-dependent forces using stored-ion spectroscopy,” *Phys. Rev. Lett.* **67**, 1735–8 (1967).
- [39] B. Venema, P. Majumder, S. Lamoreaux, B. Heckel and E. Fortson, “Search for a coupling of the Earth’s gravitational-field to nuclear spins in atomic mercury,” *Phys. Rev. Lett.* **68**, 135–8 (1992).
- [40] C. Jekeli, “A review of gravity gradiometer survey system data analyses,” *Geophys.* **58**, 508–14 (1993).
- [41] Personal communication to Lockheed Martin (2000).
- [42] E. van Leeuwen, “BHP develops airborne gravity gradiometer for mineral exploration,” *Leading Edge* **19**, 1296–7 (2000).
- [43] A. J. Romaides, J. C. Battis, R. W. Sands, A. Zorn, D. O. Benson, Jr. and D. J. DiFrancesco, “A comparison of gravimetric techniques for measuring subsurface void signals,” *J. Phys. D: Appl. Phys.* **34**, 433–443 (2001).
- [44] M. Ryan, “Memphis uses gravity to reach new navigational heights,” *Undersea Warfare* **1**, 22–3 (1998).

- [45] M. V. Moody and H. J. Paik, “Gauss law test of gravity at short-range,” *Phys. Rev. Lett.* **70**, 1195–8 (1993).
- [46] F. van Kann, M. Buckingham, C. Edwards and R. Matthews, “Performance of a superconducting gravity gradiometer,” *Physica B* **194**, 61–2 (1994).
- [47] J. Goodkind, “The superconducting gravimeter,” *Rev. Sci. Instrum.* **70**, 4131–52 (1999).
- [48] J. Brown, T. Niebauer, F. Klopping and A. Herring, “A new fiber optic gradiometer for 4-D absolute differential gravity,” *Geophys. Res. Lett.* **27**, 33–6 (2000).
- [49] H. J. Metcalf and P. van der Straten, *Laser Cooling and Trapping* (Springer-Verlag, New York, 1999).
- [50] P. R. Berman (ed.), *Atom Interferometry* (Academic Press, San Diego, CA, 1997).
- [51] L. Allen and J. H. Eberly, *Optical Resonance and Two-Level Atoms* (Dover, New York, 1987).
- [52] M. A. Kasevich, *Atom Interferometry in an Atomic Fountain*, Ph.D. thesis, Stanford University (1992).
- [53] A. Ashkin, “Acceleration and trapping of particles by radiation pressure,” *Phys. Rev. Lett.* **24**, 156–9 (1970).
- [54] T. Bergeman, G. Erez and H. Metcalf, “Magnetostatic trapping fields for neutral atoms,” *Phys. Rev. A* **35**, 1535–46 (1987).
- [55] M. H. Anderson, J. R. Ensher, M. R. Matthews, C. E. Wieman and E. A. Cornell, “Observation of Bose-Einstein condensation in a dilute atomic vapor,” *Science* **269**, 198–201 (1995).

- [56] P. D. Lett, R. N. Watts, C. I. Westbrook, W. D. Phillips, P. L. Gould and H. J. Metcalf, "Observation of atoms laser cooled below the Doppler limit," *Phys. Rev. Lett.* **61**, 169–72 (1988).
- [57] J. Dalibard and C. Cohen-Tannoudji, "Laser cooling below the Doppler limit by polarization gradients: Simple theoretical models," *J. Opt. Soc. Am. B* **6**, 2023–45 (1989).
- [58] P. J. Ungar, D. S. Weiss, E. Riis and S. Chu, "Optical molasses and multilevel atoms: Theory," *J. Opt. Soc. Am. B* **6**, 2058–71 (1989).
- [59] W. Wing, "On neutral particle trapping in quasistatic electromagnetic fields," *Prog. Quant. Elect.* **8**, 181–99 (1984).
- [60] K. E. Gibble, S. Kasapi and S. Chu, "Improved magnetooptic trapping in a vapor cell," *Opt. Lett.* **17**, 526–8 (1992).
- [61] M. A. Kasevich, E. Riis, S. Chu and R. G. DeVoe, "RF spectroscopy in an atomic fountain," *Phys. Rev. Lett.* **63**, 612–6 (1989).
- [62] M. Kasevich, D. S. Weiss, E. Riis, K. Moler, S. Kasapi and S. Chu, "Atomic velocity selection using stimulated Raman transitions," *Phys. Rev. Lett.* **66**, 2297–300 (1991).
- [63] K. Moler, D. S. Weiss, M. Kasevich and S. Chu, "Theoretical analysis of velocity-selective Raman transitions," *Phys. Rev. A* **45**, 342–8 (1992).
- [64] M. Sagnac, *C. R. Acad. Sci.* **157**, 708 (1913).
- [65] H. Stolzenberg, S. Becker, G. Bollen *et al.*, "Accurate mass determination of short-lived isotopes by a tandem Penning-trap mass spectrometer," *Phys. Rev. Lett.* **65**, 3104–7 (1990).
- [66] A. L. Fetter and J. D. Walecka, *Theoretical Mechanics of Particles and Continua* (Addison Wesley, 1980).
- [67] H. Goldstein, *Classical Mechanics* (Addison Wesley, 1980), second edition.

- [68] R. P. Feynman and A. R. Hibbs, *Quantum mechanics and path integrals* (McGraw-Hill, New York, 1965).
- [69] J. J. Sakurai, *Modern Quantum Mechanics* (Addison Wesley, 1985).
- [70] T. Gustavson, *Precision Rotation Sensing using Atom Interferometry*, Ph.D. thesis, Stanford University (2000).
- [71] P. Wolf and P. Töurenc, “Gravimetry using atom interferometers: Some systematic effects,” *Phys. Lett. A* **251**, 241–6 (1999).
- [72] Personal communication with N. Sehgal, R. Launay, Kai Bongs, and Mark Kasevich.
- [73] J. H. Moore, D. C. Christopher, M. A. Coplan and C. C. Davis, *Building Scientific Apparatus : A Practical Guide to Design and Construction* (Addison-Wesley, 1989), second edition.
- [74] J. F. O’Hanlon, *A User’s Guide to Vacuum Technology* (John Wiley and Sons, 1989), second edition.
- [75] O. W. in Crystals : Propagation and C. of Radiation, *A User’s Guide to Vacuum Technology* (John Wiley and Sons, 1983).
- [76] A. Yariv, *Quantum Electronics* (John Wiley and Sons, 1989), third edition.
- [77] O. Schmidt, K.-M. Knaak, R. Wynands and D. Meschede, “Cesium saturation spectroscopy revisited: How to reverse peaks and observe narrow resonances,” *Appl. Phys. B* **59**, 167–78 (1994).
- [78] L. Golberg, H. F. Taylor, J. F. Weller and D. M. Bloom, *Electron. Lett.* **19**, 491 (1983).
- [79] S. Kobayashi and T. Kimura, “Injection locking in AlGaAs semiconductor laser,” *IEEE J. Quantum Elect.* **17**, 681–8 (1981).

- [80] J. N. Walpole, "Semiconductor amplifiers and lasers with tapered gain regions," **28**, 623–45 (1996).
- [81] A. Abragam, *The Principles of Nuclear Magnetism* (Oxford Univ. Press, 1961).
- [82] M. H. Levitt, "Composite pulses," *Prog. NMR Spect.* **18**, 61–122 (1986).
- [83] P. Bouyer, T. L. Gustavson, K. G. Haritos and M. A. Kasevich, "Microwave signal generation with optical injection locking," *Opt. Lett.* **21**, 1502–4 (1996).
- [84] G. Santarelli, P. Laurent, P. Lemonde *et al.*, "Quantum projection noise in an atomic fountain: a high stability cesium frequency standard," *Phys. Rev. Lett.* **82**, 4619–22 (1999).
- [85] R. W. P. Drever, J. L. Hall, F. V. Kowalski *et al.*, "Laser phase and frequency stabilization using an optical-resonator," *Appl. Phys. B* **31**, 97–105 (1983).
- [86] J. S. Shirley, "Modulation transfer processes in optical heterodyne saturation spectroscopy," *Opt. Lett.* **7**, 537–9 (1982).
- [87] J. J. Synder, R. K. Raj, D. Bloch and M. Ducloy, "High-sensitivity non-linear spectroscopy using a frequency-offset pump," *Opt. Lett.* **5**, 163–5 (1980).
- [88] D. Bloch and M. Ducloy, "Theory of saturated line shapes in phase-conjugate emission by resonant degenerate four-wave mixing in Doppler broadened three-level systems," *J. Opt. Soc. Am.* **73**, 635–46 (1983).
- [89] M. A. Kramer, R. W. Boyd, L. W. Hillman and C. R. Stroud, Jr., "Propagation of modulated optical fields through saturable-absorbing media: a general theory of modulation spectroscopy," *Opt. Lett.* **5**, 163–5 (1980).
- [90] B. Do, J. Cha, D. S. Elliot and S. Smith, "Degenerate phase-conjugate four-wave mixing in a nearly Doppler-free two-level atomic medium," *Phys. Rev. A* **58**, 3089–98 (1998).
- [91] J. M. McGuirk, G. T. Foster, J. B. Fixler and M. A. Kasevich, "Low-noise detection of ultracold atoms," *Opt. Lett.* **26**, 364–6 (2001).

- [92] A. P. J. M. Hensley and S. Chu, “Active low frequency vibration isolation,” *Rev. Sci. Instrum.* **70**, 2735–41 (1999).
- [93] J. M. McGuirk, G. T. Foster, J. B. Fixler, M. J. Snadden and M. A. Kasevich, “Sensitive absolute gravity gradiometry using atom interferometry,” (2001). In preparation.
- [94] W. H. Bay (ed.), *CRC Standard Mathematical Tables and Formulae* (CRC Press, Boca Raton, 1991), 29th edition.
- [95] A. W. Fitzgibbon, M. Pilu and R. B. Fisher, “Direct least squares fitting of ellipses,” *IEEE Trans. on Patt. Anal. and Mach. Intell.* **21**, 476–80 (1999).
- [96] W. M. Itano, J. C. Bollinger, J. M. Gilligan *et al.*, “Quantum projection noise - population fluctuations in two-level systems,” *Phys. Rev. A* **47**, 3554–70 (1993).
- [97] A. Peters, K. Y. Chung and S. Chu, “Measurement of gravitational acceleration by dropping atoms,” *Nature* **400**, 849–52 (1999).
- [98] Y. Tamura, *Bulletin d’Informations Marees Terrestres* **99**, 6813 (1987).
- [99] D. W. Allan, N. Ashby and C. C. Hodge, “The science of timekeeping,” Application Note 1289, Hewlett-Packard (1997).
- [100] J. M. McGuirk, M. J. Snadden and M. A. Kasevich, “Large area light-pulse atom interferometry,” *Phys. Rev. Lett.* **85**, 4498–501 (2000).
- [101] B. Young, M. Kasevich and S. Chu, “Precision atom interferometry with light pulses,” in Berman [50], pp. 363–406.
- [102] C. J. Bordé, “Matter-wave interferometers: A synthetic approach,” in Berman [50], pp. 257–92.
- [103] D. M. Giltner, R. W. McGowan and S. A. Lee, “Atom interferometer based on Bragg scattering from standing light waves,” *Phys. Rev. Lett.* **75**, 2638–41 (1995).

- [104] I. Bloch, T. W. Hänsch and T. Esslinger, “Atom laser with a cw output coupler,” *Phys. Rev. Lett.* **82**, 3008–11 (1999).
- [105] S. B. Cahn, A. Kumarakrishnan, U. Shim, T. Sleator, P. R. Berman and B. Dubetsky, “Time-domain de Broglie wave interferometry,” *Phys. Rev. Lett.* **79**, 784–7 (1997).
- [106] P. D. Featonby, G. S. Summy, C. L. Webb *et al.*, “Separated-path Ramsey atom interferometer,” *Phys. Rev. Lett.* **81**, 495–9 (1998).
- [107] B. P. Anderson and M. A. Kasevich, “Macroscopic quantum interference from atomic tunnel arrays,” *Science* **282**, 1686–9 (1998).
- [108] D. L. Haycock, S. E. Hamann, G. Klose and P. S. Jessen, “Atom trapping in deeply bound states of a far-off-resonance optical lattice,” *Phys. Rev. A* **55**, R3991–4 (1998).
- [109] A. J. Kerman, V. Vuletic, C. Chen and S. Chu, “Beyond optical molasses: 3D Raman sideband cooling of atomic cesium to high phase-space density,” *Phys. Rev. Lett.* **83**, 439–42 (2000).
- [110] P. Treutlein, K. Y. Chung and S. Chu, “High-brightness atom source for atomic fountains,” *Phys. Rev. A* **63** (2001).
- [111] R. Holzwarth, T. Udem, T. W. Hänsch, J. C. Knight, W. J. Wadsworth and P. S. J. Russel, “Optical frequency synthesizer for precision spectroscopy,” *Opt. Lett.* **5**, 163–5 (1980).